

# Heavy impurity transport in the presence of 3D MHD ideal perturbations

Présentée le 31 mars 2022

Faculté des sciences de base  
SPC - Théorie  
Programme doctoral en physique

pour l'obtention du grade de Docteur ès Sciences

par

**Eduardo José LASCAS NETO**

Acceptée sur proposition du jury

Prof. F. Mila, président du jury  
Dr J. Graves, directeur de thèse  
Prof. I. Calvo, rapporteur  
Prof. T. Fülöp, rapporteuse  
Dr B. Duval, rapporteur



To my parents...



# Acknowledgements

This thesis would not be possible without the continuous support of my family and friends. My mother and father which always helped me when needed. From a very young age, they always encouraged me to expand my view of the world and helped the curious individual inside me to thrive. For that, I will always be very grateful. The beginning of the journey that led to this thesis would not be possible without the encouragement and incentive of André and Rogério, which helped me not only decide to embrace this new journey, but also in adapting to the new life in Switzerland. In Lausanne, I was able to meet fantastic people, from students to professors, which helped me to improve both as an individual and as a physicist. I am grateful to all my office mates during these years, Madhu, Sam and Guillermo. Each of you in your way, always improved my day with both work and non-work related discussions. I am grateful to Roberto, Kevin and Ajay with which I had great weekend cinema sessions and lunches full of peculiar humour. I am grateful to Dahye, Matteo, Jeremy, Alberto, Claudio, Anna, Trang, Justin and Federico, for your always cheerful and supportive attitude. I am grateful to Hamish and Carrie for your two distinctive British personalities, which always made lunch discussions quite interesting. I would like to thank to the musical crew of SPC, Pedro and Hamish for the musical discussions, and Lorenzo, Mirko, Guillermo for the musical sessions. I would like to thank Samuel, for knowing I could always count with you even if I we did not meet often here in Switzerland. Talking about the Portuguese crew in SPC, I would like to thank António for the nice conversations. For the helpful attitude of Olivier during TCV DDJ sessions I am also grateful. Regarding the people I worked directly with, a special thanks to Madhu for helping me understand different aspects of the topic of the work in this thesis, and to Peter Donnel, Stephan Brunner and Cristian for the discussions regarding collision operator physics without which, part of the work in this thesis would not be possible. I am also grateful to the MHD group crew, Timothée, Sam, Cristian, Mike, Andreas, Antoine, Joaquim and Margot, as well as to Daniele and Baptiste for the fruitful theoretical discussions. I would like to express my gratitude to my supervisor Prof. Jonathan P. Graves. I will not forget all the support you have given me over these four years. Your help, motivation and patience allowed me to regain confidence in my ability and in the work I was developing, and for this I will always be grateful. This list would not be complete without Maurizio, Alexandra, André, Rogério and Sandra, with which I passed great times both in Switzerland and Portugal. A special thanks is required to Sovelas and Pedro, two friends from Portugal which, many times helped me have a good laugh through video calls, which were specially important in the last year of this thesis.



# Abstract

Heavy impurity accumulation poses a problem for the operation of tokamaks featuring tungsten plasma facing components. Early termination of the plasma due to tungsten accumulation is often observed following long living 3D MHD perturbations. Such scenarios are often observed in present tokamaks like JET and ASDEX-U, and may be of concern for future machines like ITER and the European DEMO. Finding a way of designing high performance scenarios while preventing tungsten accumulation is therefore crucial. This thesis aims at understanding and modelling heavy impurity transport in tokamak plasmas in the presence of long living 3D MHD ideal perturbations. In the first part of the thesis, we develop the theoretical framework to treat the problem, building on stellarator theory for the main ions, while including the effect of strong toroidal rotation that is only present in tokamaks. The orderings of the background ion species and the heavy impurity species are developed in detail. The background ions are subsonic which allows for the calculation of their flows using the stellarator  $1/\nu$  collisional regime, while the heavy impurities flow supersonically which requires the inclusion of centrifugal effects for the impurity description. An expression for the neoclassical heavy impurity flux is obtained which helps identify the contrasting physics involved. In the second part of the thesis, we present the development of the numerical tools used to model the problem according to the theoretical framework presented. The usage of the VMEC code to obtain suitable 3D MHD equilibria is explained. Also, the development of new codes for calculating the background ion flow and heat flux of the ions, and the impurity flow from such magnetic equilibria is described. The heavy impurities are followed in this background plasma using the VENUS-LEVIS code. This code describes the guiding-center movement of the heavy impurities, accounting for the centrifugal and Coriolis drifts, as well as for the correct effect of friction and thermal forces exerted by the background ions on the impurities through a newly implemented collision operator. Finally, the numerical tools developed in this thesis are used to model the impact of long living  $1/1$  internal kink modes on heavy impurity transport. Heavy impurity accumulation is observed to occur rapidly in the presence of a  $1/1$  internal kink mode, contrary to what is observed in axisymmetry, in which off-axis accumulation occurs due to the strong rotation. These cases agree well with a JET pulse where tungsten accumulates following rapid growth of a continuous  $1/1$  mode. In the weakly 3D phase of the pulse, off-axis accumulation of tungsten is observed, whilst in the strong 3D phase of the pulse, strong tungsten on-axis accumulation is observed. The theoretical developments allow us to break down all the relevant physics effects. It is seen that such on-axis accumulation is due to the synergetic effect of the  $1/1$  mode, the strong toroidal

## **Abstract**

---

rotation and the NTV ambipolar electric field.

Keywords: Plasma Physics, Nuclear Fusion, Magnetic Confinement, Heavy Impurity Transport, Neoclassical Transport, 3D MHD, Strong Flows



# Résumé

L'accumulation d'impuretés lourdes pose un problème pour le fonctionnement des tokamaks contenant composants du tungstène en contact avec le plasma. L'arrêt précoce du plasma, en raison de l'accumulation de tungstène, est souvent observé à la suite de perturbations MHD 3D de longue durée. De tels scénarios sont souvent observés dans les tokamaks actuels, comme JET et ASDEX-U, et peuvent devenir motif de préoccupation pour les machines futures, comme l'ITER et le DEMO européen. Trouver un moyen de concevoir des scénarios de haute performance tout en empêchant l'accumulation de tungstène, est donc crucial. Cette thèse vise à comprendre et modéliser le transport d'impuretés lourdes dans un plasma d'un tokamak en présence de perturbations MHD 3D idéales à long terme. Dans la première partie de cette thèse, nous développons le cadre théorique pour traiter le problème, basé sur la théorie des stellarateurs pour les ions principaux, tandis que l'effet de la rotation toroïdale forte, présent uniquement dans les tokamaks, est inclus. Les échelles pertinentes pour les ions de fond et les impuretés lourdes sont développées en détail. Les ions de fond sont subsoniques, ce qui permet le calcul de ces vitesses de fluide grâce à l'utilisation de la théorie des stellarateurs dans le régime collisionnel  $1/\nu$ , tandis que les impuretés lourdes s'écoulent de manière supersonique, ce qui demande l'inclusion d'effets centrifuges dans leur description. Une expression du flux néoclassique d'impuretés lourdes est obtenue, ce qui permet d'identifier les différents effets physiques impliqués. Dans la deuxième partie de la thèse, nous présentons le développement des outils numériques utilisés pour modéliser le problème selon le cadre théorique présenté. L'utilisation du code VMEC pour obtenir des équilibres 3D MHD appropriés est expliqué. En outre, le développement de nouveaux codes pour calculer la vitesse du fluide et le flux de chaleur des ions de fond, ainsi que la vitesse du fluide des impuretés, à partir de tels équilibres magnétiques est décrit. Les impuretés lourdes sont suivies dans ce plasma d'équilibre à l'aide du code VENUS-LEVIS. Ce code décrit le mouvement des centres de guidage des impuretés lourdes, en prenant compte des effets de la dérive centrifuge et de Coriolis, ainsi que l'effet correct de la force de frottement et de la force thermique exercés par les ions de fond sur les impuretés, grâce à une nouvelle mise en œuvre d'un opérateur de collision. Enfin, les outils numériques développés dans cette thèse sont utilisés pour modéliser l'impact des modes de torsion interne de longue durée  $1/1$  dans le transport d'impuretés lourdes. Une accumulation rapide d'impuretés lourdes est observé en présence du mode  $1/1$  de torsion interne, contrairement à ce qui est observé en axisymétrie, dans laquelle une accumulation hors axe se produit en raison d'une forte rotation. Ces cas montrent un bon accord avec un tir du JET où le tungstène s'accumule après une

## Résumé

---

croissance rapide d'un mode  $1/1$ . Dans la phase du tir faiblement 3D, une accumulation de tungstène hors axe est observée, tandis que dans la phase d'impulsion fortement 3D, une forte accumulation de tungstène sur l'axe est observée. Les développements théoriques permettent de séparer tous les effets physiques pertinents. On constate que la telle accumulation sur l'axe est due à l'effet synergique du mode  $1/1$ , de la forte rotation toroïdale et du champ électrique ambipolaire dû à la NTV.

Mots clés : Physique des Plasmas, Fusion Nucléaire, Confinement Magnétique, Transport d'Impuretés Lourdes, Transport Néoclassique, MHD 3D, Fortes Vitesses des Fluides

# Resumo

A acumulação de impurezas pesadas representa um problema para a operação de tokamaks que possuem componentes expostos ao plasma compostos por tungsténio. O fim precoce do plasma devido a acumulação de tungsténio, é frequentemente observado após perturbações MHD 3D de longa duração. Tais cenários são observados com frequência em tokamaks actuais, como o JET e o ASDEX-U, e podem constituir uma preocupação para máquinas futuras, como o ITER e o DEMO europeu. Encontrar uma maneira de projectar cenários de alto desempenho ao mesmo tempo que se previne a acumulação de tungsténio é portanto, crucial. Esta tese tem como objectivo compreender e modelar o transporte de impurezas pesadas em plasmas de tokamaks, na presença de perturbações MHD 3D ideais de longa duração. Na primeira parte desta tese, desenvolvemos o quadro teórico para tratar o problema, com base na teoria de stellarators para os iões principais do plasma, enquanto que o efeito da rotação toroidal forte, apenas presente em tokamaks, é incluída. As escalas relevantes para os iões de fundo e para as impurezas pesadas são desenvolvidas em detalhe. Os iões de fundo são subsónicos, o que permite o cálculo das duas velocidades de fluído através do uso de teoria de stellarator no regime colisional  $1/\nu$ , ao passo que as impurezas pesadas fluem supersonicamente, o que requer a inclusão efeitos centrífugos na sua descrição. Uma expressão para o fluxo neoclássico de impurezas pesadas é obtida, o que ajuda a identificar os diferentes efeitos físicos envolvidos. Na segunda parte da tese, apresentamos o desenvolvimento das ferramentas numéricas usadas para modelar o problema de acordo com o quadro teórico apresentado. O uso do código VMEC para obter equilíbrios MHD 3D adequados é explicado. Além disso, o desenvolvimento de novos códigos para calcular a velocidade de fluído e o fluxo de calor dos iões de fundo, bem como a velocidade de fluído das impurezas a partir de tais equilíbrios magnéticos é descrito. As impurezas pesadas são seguidas neste plasma de equilíbrio usando o código VENUS-LEVIS. Este código descreve o movimento dos centros-guia das impurezas pesadas, tendo em conta os efeitos das derivas centrífuga e de Coriolis, bem como o efeito correcto da força de fricção e da força térmica exercidas pelos iões de fundo sobre as impurezas mediante uma nova implementação de um operador de colisão. Finalmente, as ferramentas numéricas desenvolvidas nesta tese são usadas para modelar o impacto de modos  $1/1$  de torção interna e de longa duração no transporte de impurezas pesadas. Acumulação rápida de impurezas pesadas é observada na presença do modo  $1/1$  de torção interna, contrariamente ao que é observado em axi-simetria, em que acumulação fora do eixo ocorre devido à rotação forte. Estes casos mostram uma boa concordância com um pulso do JET em que o tungsténio acumula após o crescimento rápido de um modo  $1/1$  contínuo. Na fase fracamente 3D do

## Resumo

---

pulso, acumulação de tungsténio fora do eixo é observada, enquanto que na fase fortemente 3D do pulso, uma acumulação forte de tungsténio no eixo é observada. Os desenvolvimentos teóricos permitem separar todos os efeitos físicos relevantes. É verificado que tal acumulação no eixo é devida ao efeito sinérgico do modo 1/1, da forte rotação toroidal e do campo eléctrico ambipolar devido à NTV.

Palavras-Chave: Física de Plasmas, Fusão Nuclear, Confinamento Magnético, Transporte de Impurezas Pesadas, Transporte Neoclássico, 3D MHD, Velocidades de Fluido Fortes

# Contents

<b>Acknowledgements</b>	<b>i</b>
<b>Abstract (English/Français/Deutsch)</b>	<b>iii</b>
<b>1 Introduction</b>	<b>1</b>
<b>Introduction</b>	<b>1</b>
1.1 Fusion energy . . . . .	1
1.2 Magnetic confinement reactors . . . . .	3
1.3 The importance of heavy impurity transport . . . . .	5
1.4 Orbits of particles in magnetic confinement devices . . . . .	8
1.5 Neoclassical particle transport . . . . .	11
1.6 State of the art on heavy impurity transport modelling . . . . .	14
1.7 Motivation for this thesis . . . . .	15
1.8 Outline of this thesis . . . . .	16
<b>2 Analytical model for the study of heavy impurity transport in the presence of 3D MHD ideal perturbations</b>	<b>21</b>
<b>Chapter2</b>	<b>21</b>
2.1 Particle description . . . . .	21
2.2 Fluid description . . . . .	22
2.3 MHD description . . . . .	26
2.4 Flux coordinates . . . . .	28
2.5 Ordering of the background ions and heavy impurities . . . . .	32
2.6 Ion background flows . . . . .	35
2.7 The drift kinetic equation . . . . .	38
2.8 Understanding flows associated with geometry . . . . .	40
2.9 Quasi-neutrality and ambipolarity . . . . .	42
2.10 Heavy impurity flow . . . . .	43
2.11 Heavy impurity neoclassical flux . . . . .	46
2.12 The guiding-center equations of motion in the presence of strong flows . . . . .	50
2.13 Conclusion . . . . .	51
<b>3 Numerical tools for the study of heavy impurity transport in the presence of 3D</b>	

<b>MHD ideal perturbations</b>	<b>53</b>
<b>Chapter3</b>	<b>53</b>
3.1 The VMEC code . . . . .	54
3.1.1 VMEC coordinates . . . . .	54
3.1.2 VMEC's variational formulation of ideal MHD . . . . .	57
3.1.3 VMEC equilibrium for modelling a JET pulse with 1/1 internal kink . . . . .	58
3.1.4 Converting from VMEC to Boozer and Hamada coordinates . . . . .	65
3.1.5 Numerical calculation of geometrical factors and background flows . . . . .	68
3.2 VENUS-LEVIS for tracing heavy impurity guiding centers in the presence of strong flows and 3D geometry . . . . .	70
3.2.1 The guiding center description with strong flows . . . . .	71
3.2.2 Collisions between impurities and the background plasma . . . . .	73
3.2.3 Conclusion . . . . .	78
<b>4 The effect of 3D MHD ideal perturbations on Heavy impurity transport</b>	<b>81</b>
<b>Chapter4</b>	<b>81</b>
4.1 The background ion flow . . . . .	82
4.2 Axisymmetry with strong flows . . . . .	83
4.3 Synergetic effect of the 1/1 internal kink mode with rotation on heavy impurity transport . . . . .	86
4.4 Synergetic effect of the 1/1 internal kink mode, rotation and NTV electric field on heavy impurity transport . . . . .	88
4.5 Heavy impurity density hole in the presence of a 1/1 internal kink mode and ECRH . . . . .	90
4.6 Heavy impurity diffusion coefficients . . . . .	93
4.7 Impact of the 1/1 internal kink amplitude on heavy impurity transport . . . . .	97
4.8 Conclusion . . . . .	99
<b>5 Conclusions and Outlook</b>	<b>101</b>
<b>Chapter5</b>	<b>101</b>
<b>A Considerations on flux coordinates</b>	<b>105</b>
A.1 Flux coordinates . . . . .	105
A.2 Boozer coordinates . . . . .	109
A.3 Hamada coordinates . . . . .	110
A.4 Transformation between straight field line coordinates . . . . .	112
A.5 Axisymmetry . . . . .	112
<b>B Derivation of the drift kinetic equation</b>	<b>115</b>
<b>Bibliography</b>	<b>121</b>

<b>Bibliography</b>	<b>125</b>
<b>Curriculum Vitae</b>	<b>127</b>





# 1 Introduction

## 1.1 Fusion energy

In today's society energy is essential to maintain the standards of quality of life. The production of energy has relied mainly on the usage of fossil fuels. It is well known that these resources will not last forever. Their use in energy production is detrimental to the environment due to large emissions of carbon dioxide, contributing to climate change. Reducing such quantities of emissions requires the urgent development of alternative processes of energy production. These energy production methods include renewable energies, nuclear fission, and nuclear fusion.

Renewable energy methods use virtually infinite sources such as sunlight, wind, hydroelectric, and geothermal heat. These sources of energy are relatively free of emissions and radioactive waste products, but large-scale distribution is difficult. Some of them, e.g. solar and wind energy, are also only capable of producing electricity intermittently, though this can be mitigated by the use of batteries. However, batteries are produced with natural resources that will ultimately also be exhausted. One continuous centralised energy production process is nuclear fission in which heavy uranium nuclei are broken up by the collision with a neutron (see figure 1.1). This process generates lighter nuclei and energetic neutrons that can then collide with other uranium nuclei to produce a fast growing chain of nuclear fission reactions. This chain reaction and the production of energetic neutrons, together with neutron control, is the key to electricity production in controlled nuclear fission power plants. Nevertheless, if uncontrolled, this process can lead to a runaway process that causes nuclear accidents (1). Furthermore, the lighter nuclei produced are very radioactive, and thus are considered high level radioactive waste which can be detrimental to the environment over a long timescale ( $\sim 10000$  years). Both renewable energy methods and nuclear fission are used for energy production today, but predictions point out that by 2050, the usage of fossil fuels will still occupy almost 50% of the total energy consumption even with the active use of these two alternatives (2). This partly motivates the present effort to develop an efficient way of producing energy using the third alternative method, nuclear fusion, which would complement the use of both

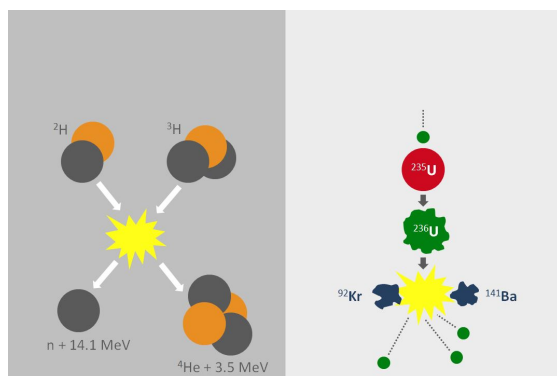


Figure 1.1 – The main reaction used to achieve fusion (left) and fission (right). Courtesy of Eurofusion site (1).

nuclear fission and renewable energies.

Fusion energy, whilst still not achievable in an efficient way, should be made easily available on a large scale once its technical challenges are overcome. Nuclear fusion is the process in which light nuclei fuse together to produce heavier nuclei and an energetic neutron (see figure 1.1). This process is difficult to achieve spontaneously because the light nuclei do not possess enough kinetic energy to overcome the strong Coulomb repulsion force between themselves. Yet, it is a natural occurring process in the stars, such as the sun in our solar system. The sun's environment provides high temperatures and a large gravitational field that help the light hydrogen nuclei to fuse into a heavier helium nucleus. The sun's high temperature helps separate the light atoms of hydrogen into ions and electrons. This mixture, usually called a plasma, is then confined due to the strong gravitational force it undergoes. The ions can then fuse together. Our inability of generating such gravitational forces on Earth requires the use of different strategies to produce fusion reactions. All such strategies heat the hydrogen (or its isotopes) to create the plasma - they mostly differ in the way the plasma is confined. This is a difficult process since there needs to be an equilibrium between the outward expansion (due to the thermal diffusion) and the forces that are confining the plasma. However, it is exactly this difficulty that grants nuclear fusion its safety compared with nuclear fission, since if some problem occurs in the operation, the fine balance that allows fusion to occur is lost and operation stops instantaneously. The concept of a fusion power plant is thus safer than a fission power plant. Moreover, nuclear fusion produces more energy than nuclear fission per reaction. These advantages motivate the development of good strategies to confine the plasma in order to efficiently produce energy by fusion <sup>1</sup>.

---

<sup>1</sup>There are some disadvantages of fusion, notably high cost, large infrastructure and large quantities of medium scale radioactive waste

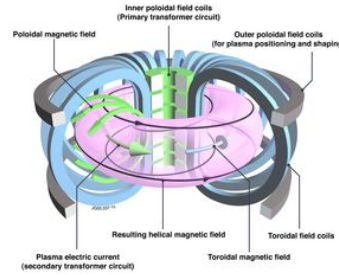


Figure 1.2 – Schematic of a magnetic confinement reactor. This design is called tokamak. Courtesy of Eurofusion site (1).

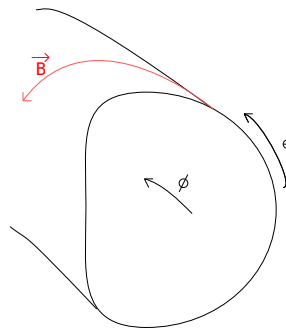


Figure 1.3 – Geometry of a toroidal plasma.  $\theta$  is the poloidal angle and  $\phi$  is the toroidal angle. The magnetic field  $\mathbf{B}$  is the sum of a toroidal and poloidal components.

## 1.2 Magnetic confinement reactors

Up until now, the most successful way of confining the charged particles that constitute the plasma are magnetic confinement reactors. The work of this thesis is focused in this area of nuclear fusion. In these machines, the plasma is confined using strong magnetic fields produced by coils placed (mostly) outside the vacuum vessel containing the plasma. The magnetic field helps confine the plasma through the magnetic force. The ions and electrons comprising the plasma, being charged particles, undergo a helical trajectory around the magnetic field lines. Thus, the main idea for the design of a magnetic confinement reactor is that of a torus (see figure 1.2). The main particle confining field is thus a toroidal magnetic field (see figure 1.3). However, this toroidal field is not enough to confine the plasma as the electric fields present inside the plasma will make the particles drift away from the central region of the tokamak until they are lost to the walls. Ions and electrons drift in opposite directions which reinforces the electric field, and the drift itself. It is therefore, necessary to generate an extra poloidal field to reduce the drifts and keep the plasma better confined. The two main designs for magnetic confinement reactors are called tokamaks and stellarators. These devices mainly differ in the way the poloidal magnetic field is generated.

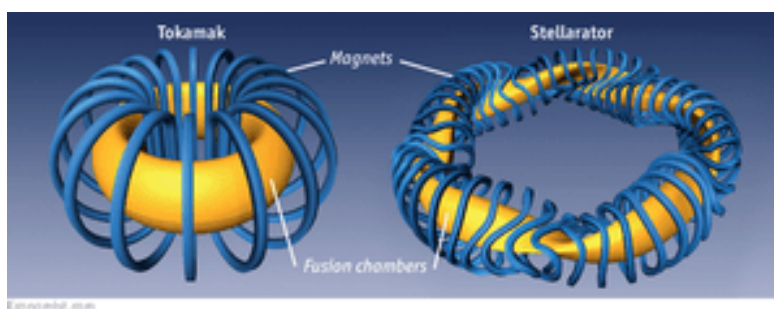


Figure 1.4 – Schematic of the two main designs of a magnetic confinement reactor. Tokamak on the left and stellarator on the right (1).

Since a plasma is composed of both electrons and ions it can be looked at as a charged fluid. Magnetohydrodynamics (MHD) (3) is the theoretical framework that describes the behaviour of the fluid and electromagnetic properties of the plasma. The designs of magnetic fusion reactors are found by finding a solution to the fine equilibrium between the kinetic pressure of the plasma and the pressure exerted by the magnetic field energy. In the case of tokamaks the toroidal design is made such that it is symmetric around the toroidal direction (see figure 1.2). In order to achieve such design, a toroidal field is generated by identical magnetic coils (called toroidal coils) placed and spaced symmetrically around the vacuum vessel and along the entire torus (see figure 1.2). The poloidal field is then obtained by generating a current inside the plasma inductively. Such current is generated via the plasma behaving as a secondary circuit in a transformer, in which the primary circuit are poloidal coils placed at the centre of the machine (see figure 1.2).

The two remaining ways of generating a poloidal magnetic field consist in designing the toroidal coils and vessel system in such a way that the magnetic axis is non-planar, or the plasma poloidal cross section rotates along the toroidal direction (4). This implies that a design employing at least one of these two methods does not necessarily possess any symmetry (see rightside of figure 1.4). Such non-axially symmetric (or non-axisymmetric) 3D design is called a stellarator and does not need any current for generating a poloidal magnetic field.

The poloidal field generation by these three methods in a toroidal plasma device can be easily compared to that of water flowing in a toroidal pipe. Since the charged particles follow the magnetic field lines, and a plasma can be modelled by a charged fluid, we can imagine that a very small tube of plasma fluid is always following a magnetic field line. This means that the velocity of the small fluid tube is in the same direction as the magnetic field. Thus, the magnetic field in such a plasma has a role comparable to the velocity of water in a pipe. In a toroidal pipe, water can rotate poloidally in three ways. One of them is to generate a vortex that makes the water rotate poloidally. This method is similar to the generation of plasma current. In fact, a current is a measure of the vorticity of the magnetic field. Another way to rotate the water is to make the toroidal pipe twisted or rotate its cross section (4). This is equivalent to the stellarator design.

The axisymmetric design of tokamaks provides simpler construction of the large coils, and potentially lower cost. Furthermore, tokamaks provide better particle confinement than stellarators since the loss of particles due to additional drifts caused by the curvature of the magnetic field is smaller. However, tokamaks are not inherently steady state devices because they generally need an induced current to operate. The necessity of the current is also a source of potential issues for the tokamak design concept. The current can lead to small perturbations of the magnetic field, which can be described within the MHD formalism. These perturbations can grow and modify the initially axisymmetric field. In the best case, these perturbations grow and saturate, generating a new ideal (non-resistive) equilibrium magnetic field and plasma, that are no longer axisymmetric. In some cases this perturbation turns out to be too unstable and leads to disruption of the plasma operation. It is easy to understand that these instabilities should exist for the case of finite vorticity of the magnetic field when comparing again to the analogy of water flowing in a toroidal pipe. While vorticity in the water makes the water rotate poloidally, it may also generate instabilities such as the well-known Kelvin-Helmoltz instability. In tokamaks, the current of the different small tubes of plasma induce a repelling force between them. When the plasma tube is perturbed, this repelling force can lead to instabilities. Stellarators are less prone to have MHD instabilities since the plasma current is very small. They are also designed to be inherently steady state devices. Yet, the complexity of their design makes them very costly and difficult to construct. They also provide less confinement due to the very complex magnetic curvature they usually possess. In this thesis we focus on understanding heavy impurity transport in the tokamak configuration in the presence of ideal 3D MHD perturbations. Indeed, we investigate plasma scenarios where MHD instabilities in the tokamak have not caused disruptions, but have saturated. Such scenarios are important because they occur in several tokamak devices in operation like JET, ASDEX-U, WEST, TCV and EAST. Moreover, the next-step devices, ITER which is being constructed, and the European DEMO which is in its design phase, are also tokamaks, in which such operation scenarios may also be important. The description of heavy impurity transport in 3D tokamak plasmas is one important subject, more complex and challenging than in intrinsically 3D stellarator plasmas (for which significant research has already been undertaken). As will be seen, plasmas in tokamaks tend to rotate toroidally, and the consequent forces (e.g. centrifugal) felt by heavy impurities need to be taken into account in the physics problem.

### 1.3 The importance of heavy impurity transport

Both tokamaks and stellarator plasma facing walls are subject to hot temperatures. Sometimes the jets of plasma coming from the inner region of the plasma (called the plasma core, see figure 1.5) can hit the wall. Since these jets are at quite high temperatures, it is therefore important to make the wall able to sustain such hot temperatures. Moreover, it is also important to exhaust impurities that enter the plasma originating from either fusion products (such as helium ash), from the vessel wall, or from other plasma facing components. For many

years the simplest solution used was the inclusion of a so-called limiter. This is usually made of carbon (graphite) and it is located on the wall of the device along the toroidal direction and around the mid plane of the device. This wall structure provided direct contact with the plasma which helped mitigate the degradation of the remaining sections of the wall as well as recycling of impurities. However, a carbon limiter had the disadvantage of retaining a large portion of hydrogen, which is the fuel of the fusion reactions, hindering the efficiency of energy production.

A different approach was implemented during the operation of the ASDEX tokamak. The ASDEX tokamak used a structure called the divertor. The divertor is composed of two plates (called 'legs') located on the lower region of the wall in a tokamak. Contrary to the limiter, the divertor does not touch the high density plasma. Instead, the heat load is placed on the diverter plates via a special magnetic field configuration called a separatrix (see figure 1.5). In this separatrix the magnetic field lines do not close on themselves. These magnetic field lines are 'open' and are directed to the divertor legs. This helps redirect the hot jets of plasma to the divertor plates. This geometry provides less stress on the wall since the heat loads are localised in the divertor plates (which is a much smaller area than the limiter). It was also verified with the ASDEX operation that this geometry provides better confinement of the plasma by achieving a mode of operation called the H-mode (5). Carbon was used in the first divertor designs and many subsequent machines (including the Swiss TCV machine today). Unfortunately, carbon cannot be used as a divertor material in a reactor because it will retain tritium. Tungsten has been chosen instead due to its high heat tolerance (highest melting point of all metals), low erosion rate and low hydrogen retention (6).

Tungsten ions are usually heavy when compared with the hydrogen and helium ions that ideally compose the plasma, and are therefore classified as heavy ions. Despite its low erosion rate tungsten, can still be eroded from the divertor and be transported into the plasma (see figure 1.6). If tungsten ions reach the core of the plasma, they will radiate due to collisions with the background plasma, which can excite their large number of electrons. The de-excitation of such electrons will send out the energy difference as radiation. This radiated energy comes at the expense of decreasing the thermal energy of the plasma (see figure 1.6) (total energy conserved). This loss of energy decreases the core temperature of the plasma, and sometimes it is drastic enough to stop plasma operation. Such situations are currently seen in JET and ASDEX-U (7). Understanding how to mitigate the transport of tungsten to the core of the plasma (core accumulation) is therefore crucial for efficient reactor operation of present tokamaks like JET with ITER-like wall, ASDEX-U and WEST. In fact, this makes it a high priority for defining operation scenarios for ITER, because its divertor will inevitably be composed of tungsten to avoid tritium retention while handling heat fluxes (8).

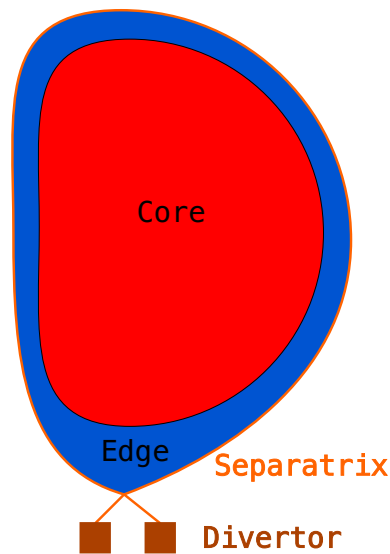


Figure 1.5 – The two regions of the plasma where the magnetic field lines are closed. The hotter and most inward region called core (red). The outer region called edge (blue). In orange we have an open magnetic field line in the separatrix. The limits of the magnetic field line touch the divertor (brown).

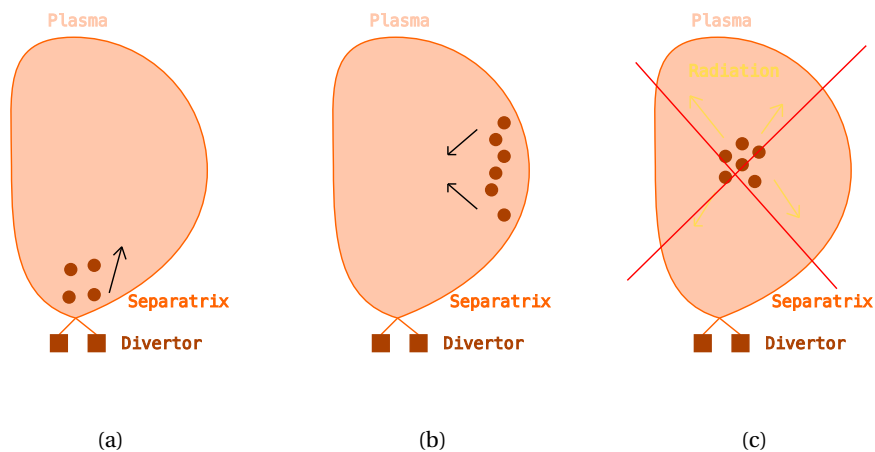


Figure 1.6 – Simplified diagram of tungsten (brown circles) accumulation and the resultant degradation of the plasma. (a) The reactor is designed with a tungsten divertor (brown squares). (b) The hot plasma may strike the wall and scrape off some tungsten ions. (c) Tungsten ions are transported through collisions with the plasma. (d) If the tungsten reaches the plasma, the plasma loses energy by radiation sometimes causing the plasma to terminate.

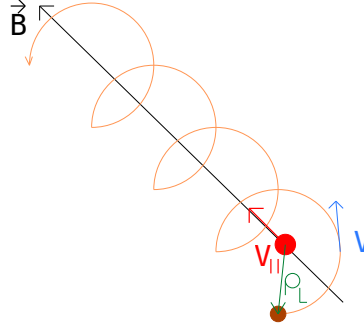


Figure 1.7 – A charged particle (brown) in a magnetic field will follow a helical trajectory (orange) around the magnetic field line (black) with a velocity  $v$  (blue). We can divide this movement into a circular movement around the magnetic field line with a radius  $\rho_L$  called the Larmor radius, and a movement of the center of this circular movement along the magnetic field lines with a velocity  $v_{||}$  parallel to the magnetic field line. The center of the Larmor gyration is called guiding center (red). The typical gyration frequency associated with the circular movement is called cyclotronic frequency  $\Omega_C$ . Electrons will have a circular movement in the opposite direction than ions (shown in this figure).

### 1.4 Orbits of particles in magnetic confinement devices

In order to understand the transport of charged particles in a magnetic confinement device, it is important to understand the basic movement of these particles under the influence of magnetic fields. Such particles will follow helical trajectories around a magnetic field line (see figure 1.7). This movement can be separated in the Larmor radius gyration and the guiding center movement (see figure 1.7).

The plasma in magnetic confinement devices is under the action of different forces  $\mathbf{F}$ . These forces, if perpendicular to the magnetic field (see figure 1.8), can cause the charged particles to drift away from their original trajectory around a magnetic field line. If there is no perpendicular force then the particle rotates with a constant Larmor radius around the field line (see 1.8). However, if a force perpendicular to the magnetic field line is applied in the plasma the perpendicular velocity of the charged particle is changed. This change in the perpendicular velocity causes the Larmor radius to increase (see figure 1.8). Such a modification creates a



deviation of the perfect circular movement around the magnetic field line which effectively creates a movement of the guiding center of the particle trajectory in the direction perpendicular to the magnetic field and the force  $\mathbf{F}$ , which is denoted by  $\mathbf{F} \times \mathbf{B}$  (see figure 1.8). Such movement is called a drift of the guiding center related to the force  $\mathbf{F}$ . This drift is a movement of the guiding center, but it is a consequence of the Larmor radius movement of the particles.

A plasma can be subject to different forces in magnetic confinement devices. All these forces can create a drift of the guiding centres of the particles. The most obvious force is an electric force since the particles in a plasma are charged. The drift due to the electric force is in fact the drift that makes it necessary to have a poloidal magnetic field in magnetic confinement devices. All the particles of a ion species in the plasma have different velocities. However, under the correct circumstances, on statistically averaging over all the particle velocities, we may find that the ensemble of particles of one species will move with a mean velocity. We call this a flow, since the ensemble of particles flow macroscopically at that velocity. In magnetic confinement devices, the particles of each species can have large flows. For example, heating the plasma with different mechanisms can make the plasma rotate in the symmetry direction of the device. In the case of tokamaks the ensemble of particles can often rotate in the toroidal direction. This rotation can generate a centrifugal force analogous to that felt by a person driving a car in a curved road. The interaction between this flow velocity and the parallel velocity (around the magnetic field line) of each particle guiding center can also generate a Coriolis force. This is the same force that will make the cyclones rotate in different directions in the North and South hemispheres.

Finally, the magnetic field itself can generate two different forces. The first is caused by the movement of a particle's guiding center with a parallel velocity along a magnetic field line. In such situation, the particle's guiding center can also feel a centrifugal force. This happens in magnetic confinement devices, because the magnetic field has a curvature and thus the particle is moving in a "curved road", the magnetic field. We call this the magnetic curvature force. The second, less intuitive, force can be exerted by the magnetic field itself. To understand this force, it is first necessary to look at the Larmor movement of the particle. We know that currents are generated by the movement of charged particles. A current will generate a circular magnetic field around itself, as it is the case of generation of a poloidal magnetic field component in tokamaks due to a toroidal plasma current. The inverse is also true. A circular current will create a magnetic field that passes through the circular surface defined by the current. Thus, a particle moving with a Larmor radius will generate a small magnetic field associated with the particle. We say that the particle has a magnetic moment  $\mu$ . This means that the particle undergoing this movement is itself a magnetic dipole. Magnetised materials gain their properties due to being composed of magnetic dipoles, since unlike electric charges, magnetic monopoles cannot exist. A magnetic moment  $\mu$  can be seen as the particle charge equivalent for magnetic fields. We know that charged particles will move from zones of high to low electrical charge. Or equivalently, from zones of highest to lowest electric potential. In magnetic fields, particles with a magnetic moment  $\mu$  will be forced to go to zones of weaker magnetic field. This force is usually called magnetic mirror force and is the equivalent of the

electric force in which the charge is the magnetic moment, and the potential is the magnitude of the magnetic field. All the perpendicular components of the described forces can generate drifts of the guiding centers.

A further discussion can be made specifically about the mirror force parallel to the magnetic field. In tokamaks, for an axisymmetric plasma configuration <sup>2</sup>, relevant parameters are independent of the toroidal direction. Thus, the magnetic field magnitude  $B$  varies only in the radial and poloidal directions and the parallel mirror force points in the poloidal direction pushing particles from the zone of stronger magnetic field to weaker magnetic field ( $\theta = 0$ ). Since the magnetic field magnitude is the potential for such a magnetic force exerted on the particles (with a constant magnetic moment), they can be trapped in wells of the magnetic field magnitude. This happens because the magnitude of the magnetic field has the form of a wave with a harmonic component depending of the poloidal angle (see figure 1.9). Thus, particles that have enough energy to overcome the magnetic well, or in other words the parallel mirror force, can move in the entire poloidal direction (passing or circulating particles, see figure 1.10), but particles that do not have enough energy are not able to overcome the magnetic well, and thus are trapped on the poloidal angles around the minimum of the magnetic field magnitude (banana particles, see figure 1.10). As both the orbits of these particles are poloidally symmetric around the  $\theta = 0$  plane, the radial drift of both of these particles averages to zero due to it pointing in different directions above and under the plane  $\theta = 0$ ). As a consequence, in tokamaks, both passing and trapped particles are well confined (in the absence of collisions). However, both the magnetic mirror and curvature radial drifts are larger in the zones of weaker magnetic field. The radial excursion of the trapped ('banana') orbits is therefore larger than for the passing orbits, as the trapped orbit is mostly located poloidally near the zones of weaker magnetic field.

In stellarators, the magnetic field is no longer axisymmetric, having at least one harmonic which depends on both poloidal and toroidal angles. This can cause several local minima in the magnetic field magnitude (see figure 1.9). Particles can be trapped in these local minima which means they are trapped in a helical direction defined by a helical angle  $\alpha = m\theta - n\phi$  (with  $n$  and  $m$  integers defining the number of the poloidal and toroidal harmonics). These are called helically trapped particles or 'superbananas'. Such particles can be trapped in local minima that are not symmetric around the  $\theta = 0$  plane. Over an orbit, the radial drift felt by these particles does not average to zero and these particles can drift away from the device even in the absence of collisions. In tokamak plasmas with 3D MHD ideal perturbations, the same type of particles can be present in the plasma, though in these cases the 3D magnetic field components are weaker than in stellarators, and thus, there is less helical trapping.

Another important feature of tokamaks is that they allow for strong flows to exist in the toroidal direction. These strong flows, as discussed before, will exert a centrifugal force on the particles. This force comprises both a perpendicular force, that can make the particles drift, as well as a poloidal centrifugal force that may cause particles to be trapped in the outboard of the

---

<sup>2</sup>This thesis will consider tokamak steady state plasmas that are not axisymmetric

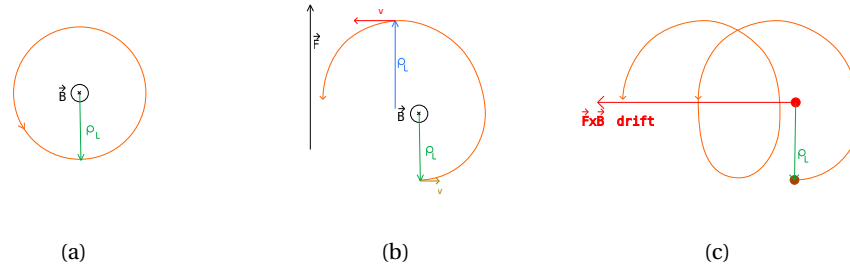


Figure 1.8 – Simplified picture of the drift movement of the guiding center of particles moving in the magnetic field (pointing upward from the paper). (a) Without forces  $\vec{F}$  perpendicular to the magnetic field the Larmor movement is a perfect circle. (b) A perpendicular force acting on the particle changes the perpendicular velocity and the size of the Larmor radius  $\rho_L$ . (c) The change of the Larmor radius size makes the Larmor movement deviate from a perfect circle and the guiding center moves in the direction perpendicular to both the magnetic field and the force  $\vec{F} \times \vec{B}$ .

poloidal cross section - a centrifugal well analogous to the magnetic well. Usually these effects are weak for hydrogen and helium ions but can be quite strong for tungsten due to their larger mass. Usually, the analogous centrifugal potential associated with such a strong rotation behaves in a similar way to the magnetic field magnitude in tokamaks and thus the particles are still well confined. In general stellarator geometry, strong flows are damped. The culprit of such a phenomenon is the neoclassical viscosity, which is the effective viscosity acting in the plasma when the particles flow with a mean flow velocity. It is called 'neoclassical' because the viscosity coefficients associated with it depend on the geometry of the magnetic field. The 3D tokamak plasma configurations considered in this thesis also have some flow damping due to toroidal viscosity but significant residual velocity has to be taken into account.

To sum up, in the absence of collisions, the transport of ions in the presence of toroidal magnetic geometry effects (that is neoclassical transport in the collisionless limit) is mainly in the direction parallel to the magnetic field for tokamaks, because the perpendicular transport (cross-field transport) is averaged to zero. However, in stellarators and 3D tokamak plasmas the cross-field transport can be finite and cause the particles to be lost to the wall.

## 1.5 Neoclassical particle transport

The particles in a plasma are subject to collisions. In the presence of collisions, the neoclassical cross-field transport described above can be non-zero even for tokamak plasmas. The collisions in the plasma happen due to the Coulomb potential interactions between the particles in different helical orbits that are separated by up to a Larmor radius. At each collision, the particles that collide can abruptly change their orbits and, in a configuration with a constant magnetic field, are transported radially by a distance of a Larmor radius. This process which happens even in a constant magnetic field (with no curvature) is called classical

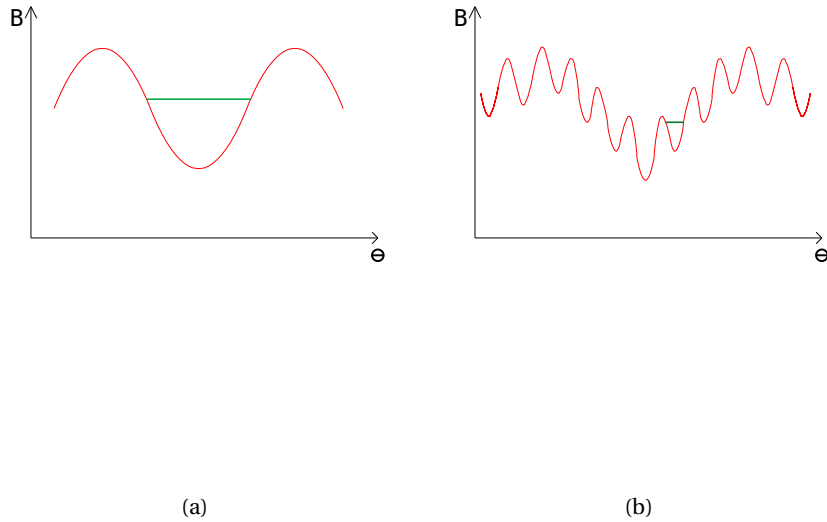


Figure 1.9 – The magnetic field force magnitude  $B$  is a potential for the magnetic mirror force in magnetic confinement devices. (a) In tokamaks, the particles can be trapped (green) in a symmetric well around the absolute minimum of  $B$  at  $\theta = 0$ . (b) In stellarators, the non-axisymmetric magnetic field originates different local minima in which the particles can be trapped (green).

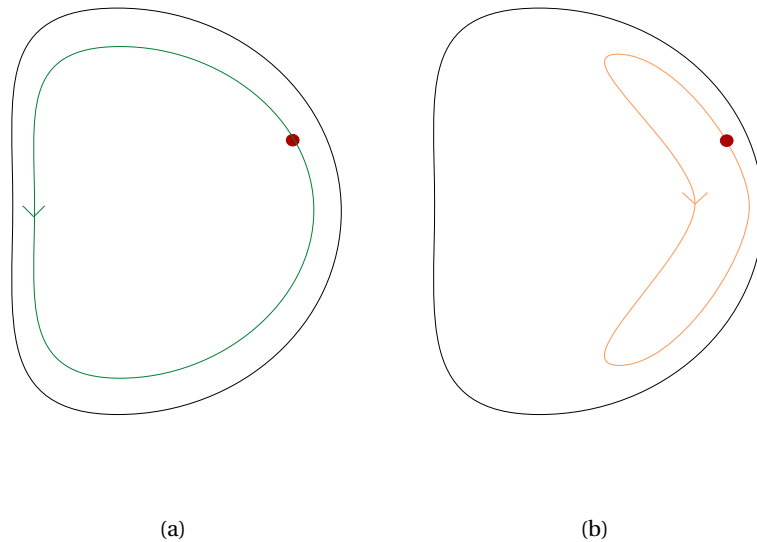


Figure 1.10 – Passing (green) and trapped (orange) particle trajectory in a tokamak when projected in the poloidal cross section of a tokamak (black). The trapped trajectories (orange) are called banana orbits due to their shape.

transport (9). The trapped particle orbits in tokamaks and stellarators have a radial width that is usually larger than a particle Larmor radius. Thus, when trapped particles collide, their guiding centers may change trajectories. This radial movement is of the order of the width of the trapped orbit. Given the same frequency of collisions as in a configuration with a constant magnetic field, this radial transport is thus faster than classical transport and it is called neoclassical (collisional) transport. A third type of transport can occur in fusion devices and is called anomalous transport. This transport occurs usually due to the turbulence occurring in the plasma. This turbulence generates large zones (turbulent vortexes or eddies) in which the macroscopic physical quantities of the plasma have similar structure. These zones often have a width larger than trapped particle orbits. The particles in these zones can collide with the particles in a different zone, changing their position. This transport is often faster than neoclassical transport, because the change of the particle positions can be of the order of the width of such eddies.

Due to the different type of orbits in tokamaks it is important to distinguish what processes are important when discussing collisional neoclassical transport. The collisions between background ions will happen at some collisional frequency which we call  $\nu_{II}$ . At the same time, the passing and trapped particles have a characteristic frequency associated with completing an orbit. For trapped particles, we call this the bounce frequency  $\omega_B$ . For helically trapped particles (or superbanana particles) that are still confined (i.e. that do not drift away from the tokamak, and complete an entire orbit), the time they need to travel the full orbit is larger than for banana particles. Thus, the bounce frequency is smaller for superbananas than bananas. In axisymmetric tokamaks, for high enough collisionality  $\hat{\nu} = \nu_{ii}/\omega_B > 1$ , the collisions happen faster than the timescale in which trapped particles complete one banana orbit. In this regime, the trapped population is not important and the plasma can be treated mostly as a fluid (Pfirsch-Schlüter regime). If collisionality decreases enough for the banana particles to complete a banana orbit before a collision, the trapped particles start to be important for the collisional transport, and we call this low collisionality regime, the banana regime. In 3D plasmas, the Pfirsch-Schlüter regime has the same meaning as in tokamak axisymmetric plasmas. If we decrease collisionality in such plasmas, the collisions are fast enough to prevent helically trapped particles from completing their orbits, but not fast enough to prevent the same for banana orbits. This regime is called  $1/\nu$  regime and the banana orbits dominate the transport processes. If collisionality goes even lower, helically trapped particles start to be able to complete their orbits before a collision and thus can dominate the transport processes. We call this low collisionality regime, the  $\sqrt{\nu}$  regime. The equation that describes all the neoclassical transport physics including collisions is called the drift-kinetic equation.

In this thesis, we are interested in core transport of tungsten. Such transport has been seen to be predominantly neoclassical in axisymmetry (6). Neoclassical transport theory has been developed over many years. The drift kinetic equation that describes the particle movement of the guiding centers has been derived e.g. in (10). A review of the topic of collisional transport has been written in detail (11), and the topic is also carefully explained in (9) for axisymmetric devices. The drift kinetic equation in the presence of strong flows has been derived in (12) and

(13) and the main ion transport in that regime is discussed in (13) and (14). The particular case of neoclassical axisymmetric transport in the Pfirsch-Schlüter (high collisionality regime) can also be found in (9) and (11). Work on neoclassical axisymmetric transport in the banana regime (low collisionality) is found in (15), (16), (17), (11), (18), (9). Aspects of neoclassical transport theory in 3D magnetic geometry for the background ions and electrons in the plasma are discussed in (19), (9). A recent review by Shaing et al. (20) covers most of the important aspects of 3D neoclassical transport, 3D neoclassical flows and neoclassical toroidal viscosity (NTV) processes. Calculations of neoclassical transport in the several regimes for 3D magnetic configurations can be found specifically in (21), (22), (23), (24), (25), (26), (27), (28), (29), (30), (31) and (32). A different and more recent approach to the calculation of the neoclassical flows and bootstrap current in 3D magnetic field configurations can be found in (33). Work on neoclassical transport of the background ions in tokamaks with 3D MHD ideal perturbations can be seen in (34) and for 3D resonant perturbations in (35), (36), (37), (38), (39), (40), (41) and (42).

### 1.6 State of the art on heavy impurity transport modelling

The development of the theory of heavy impurity neoclassical axisymmetric transport started with the understanding that heavy impurity transport at trace density limits was mainly dictated by background ion density and temperature gradients. These effects are due to the friction force and thermal force that the main ions exert on the heavy impurities when they collide. In the Pfirsch-Schlüter (PS) regime, for all species it was seen (43) that both density and temperature gradients generate radially inward transport of impurities, causing them to accumulate on axis. Following that, the calculations were extended to treat the banana regime of the main ions (44). It was seen that, in this regime the thermal force would actually oppose the friction force. Thus, the background ion temperature gradient provides a thermal screening effect. Later, it was observed that strong heavy impurity poloidal density asymmetries can be generated in the plasma. Due to its large mass, heavy impurities like tungsten can feel a strong centrifugal force that cause them to redistribute poloidally in the plasma. Neutral beam injection (NBI), which is used to heat the plasma in tokamaks like ASDEX-U and JET, causes tungsten ions to rotate supersonically along the toroidal direction. In the framework of axisymmetric neoclassical theory for impurities, these effects were calculated in (45), (46), (47) and (48). The strong centrifugal force generates an in-out asymmetry of the impurity density. The heavy ions are then trapped on the outboard side of the device. At this region of the poloidal plane, the friction force points radially inward contrary to what happens on the inboard side. Accumulation of impurities is therefore enhanced because most of impurities are trapped in the region in which the force points radially inward. Strong poloidal asymmetries of impurities can also be generated due to small perturbations of the background quasi-neutrality condition. Perturbing this condition creates a small poloidal electric field. Notably, since the charge of heavy impurities is high, the effect of the small electric field is felt strongly by these ions. Centrifugal effects also cause a correction in quasi-neutrality. Another mechanism that

can generate such corrections are the effects of large friction and thermal forces felt in the edge of tokamaks due to the large background ion density and temperature gradients. Such effects have been studied in (49) and (47). It was seen that such strong collisional effects could trap the particles on the inboard side of the poloidal cross section preventing accumulation. Ion cyclotron radio wave heating (ICRH) is another mechanism that can generate poloidal asymmetries. ICRH is used to heat the plasma in JET. It was seen in (6) that this mechanism can perturb the quasi-neutrality condition generating an electric field that often helps reduce impurity accumulation.

The modelling of neoclassical heavy impurity transport in stellarators has also seen progress in recent years. The development of neoclassical transport theory for thermal ions and electrons enabled calculations for the background ion and electron flows and heat fluxes (26), (33) in stellarators. These flows are important for calculating the friction and thermal forces felt by the heavy impurities. These results enabled the description of heavy impurity transport in stellarators. Experimental observations in the LHD stellarator showed that the ambipolar electric field, which is usually negative, played an important role in pushing impurities radially inwards, overwhelming the effect of temperature screening. This is in contrast to what happens in axisymmetric configurations, in which the radial electric field drive of transport vanishes. Recently it was shown theoretically that for the regime of interest in stellarators such as W7-X, in which the impurities are highly collisional, and the main ions are in the low collisionality  $1/\nu$  regime that, temperature screening may be important when compared to the effect of the ambipolar electric field (which is seen to be negligible (50)). This result is contrary to most observations in stellarators where the electric field drive is usually dominant. Indeed, recent theoretical results show that with the inclusion of parallel impurity density asymmetries in stellarator configurations, the effect of the ambipolar radial electric field reappears and is important (51), (52). Finally, impurity density asymmetries were considered due to corrections to quasi-neutrality when considering helically trapped main ions (51) and fast ions (52) in W7-X-like configurations.

## 1.7 Motivation for this thesis

The results described in the previous section show that a good understanding of neoclassical theory exists for axisymmetric magnetic fields in tokamaks. However, such theory may not be applicable to 3D tokamak plasmas in which 3D MHD perturbations may exist. These perturbations can have non-negligible amplitudes such that, the neoclassical tokamak related theory just described above may fail. Operational scenarios in tokamaks like JET and ASDEX-U often feature 3D ideal MHD perturbations, such as long-lived 3D ideal perturbations, or nonlinear 3D MHD modes with magnetic islands. Experimental studies have reported heavy impurity behaviour in the presence of both long living MHD perturbations (53) and magnetic islands due to neoclassical tearing modes (54). Nevertheless, only limited work has been reported on the effect of 3D long living ( $n = 1, m = 1$ ) MHD modes on heavy impurity transport (55), (56). And crucially, stellarator theory is also not entirely applicable to 3D

tokamak plasmas because plasma flows are strongly damped by the 3D magnetic fields of stellarators (see section 2.6). In tokamaks, strong toroidal rotation due to NBI is still observable when 3D long living modes are present, making the modelling of such scenarios a distinct problem. This combination of physics effects is critical, as will be seen.

Long living MHD modes like the 1/1 internal kink mode can sometimes exist without significantly deteriorating plasma operation. For this MHD mode, the core of the plasma suffers a rigid displacement that makes the magnetic axis have a poloidal excursion as we move around the toroidal direction. It is observed that this type of mode can impact heavy impurity transport in JET. In figure 1.11, we see a Fourier analysis of the toroidal mode number of the magnetic field during a JET pulse. It can be seen that the  $n = 1$  mode becomes strong after  $t = 46.61\text{ s}$  (see figure 1.12), indicating the presence of a strong 1/1 internal kink mode. To investigate the effect of the mode on tungsten transport, we may look at the soft X-ray tomography (SXR) diagnostic. This diagnostic provides a measure of X-ray emissions in the region of the light spectrum that corresponds to the electron transitions in the tungsten ions. Therefore, a strong signal in this diagnostic corresponds to a strong peak in the density of tungsten in the plasma. We can see the SXR signal on the poloidal cross section of JET in figure 1.13. At a time  $t \approx 45.9\text{ s}$  we see that there is off-axis accumulation of tungsten. At this time the plasma is nearly axisymmetric (see figure 1.12). However, at a time  $t \approx 46.63\text{ s}$  in which the 1/1 internal kink mode is strong (see figure 1.12), we observe tungsten accumulating on axis. Experimentally, it is difficult to understand if this accumulation is indeed due to the 3D effects, but a clearer view of the physics can be obtained through modelling of such a problem. Another interesting behaviour of impurity transport can be seen in ASDEX-U experiment with long living 1/1 internal kink modes. The experimental studies done in ASDEX-U (53) show that operational scenarios with the presence of a long living 1/1 ideal internal kink mode during electron cyclotron heating can help prevent impurity accumulation. This scenario could possibly be used in future tokamaks like ITER to prevent impurity accumulation. Understanding the physics behind these contrasting experimental observations is thus very important. Finally, the construction of the European DEMO is already being planned. This machine will be used to demonstrate the viability of fusion energy as a power plant. Operation scenarios with a confinement mode called QH-mode are being considering to avoid edge localised modes that can potentially damage such large device. This QH-mode operation features long living 3D MHD perturbations of the magnetic field in the edge region of the tokamak. It is therefore also important to understand through modelling how these modes affect heavy impurity transport. There are indications in ASDEX-U that EHO's can increase inward transport of impurities, which is a concern that requires further considerations.

## 1.8 Outline of this thesis

The work in this thesis focuses on formulating a theoretical framework for the study of heavy impurity transport in tokamak plasmas with long living 3D ideal MHD perturbations in the presence of strong flows and the ambipolar electric field. This model is implemented in the



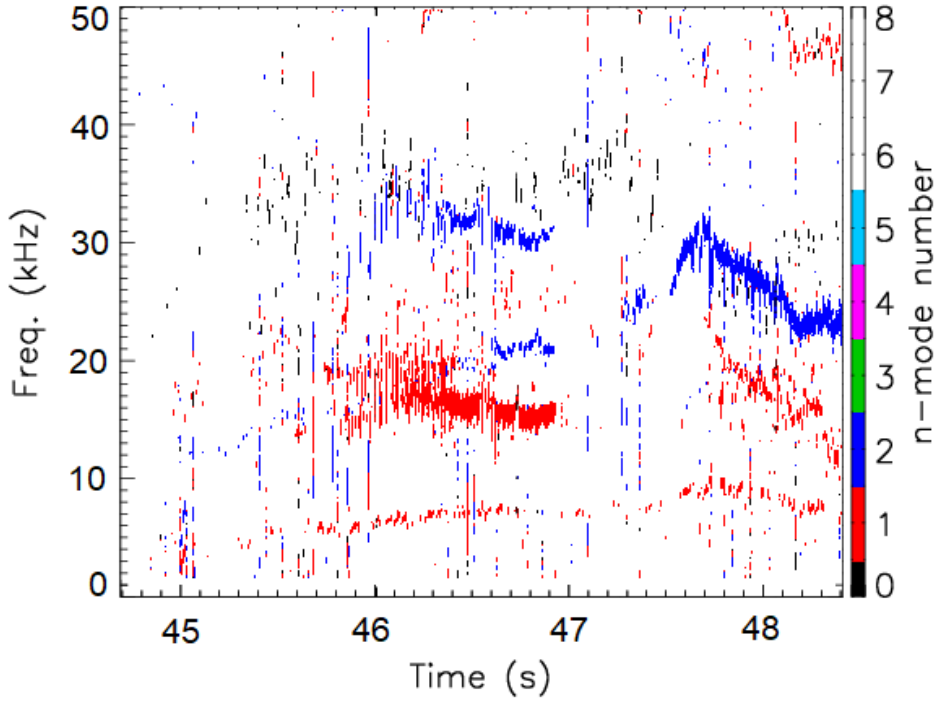


Figure 1.11 – Analysis of the toroidal mode number  $n$  for JET pulse #92181.

code package composed of existing codes VMEC (57), (58), (59) and VENUS-LEVIS (60), (61).

In chapter 2, we focus on presenting the theoretical framework deployed to treat the type of problems investigated in this thesis. Both known and novel theoretical results are presented in this chapter. We start by presenting various important plasma descriptions which are well known. We then formulate a way of tackling the problem of heavy impurity transport in the presence of 3D MHD ideal perturbations and strong flows. We start by discussing the empirically relevant orderings necessary to treat the problems of interest. This ordering allows the impurities to flow supersonically in the toroidal direction, while the background ions are treated as strongly subsonic. Thus, impurities feel the effect of strong flows, but the neoclassical background ion flow calculations for general 3D geometry (e.g. in stellarators) (26), (33) may be used. The additional effect of strong flows in the impurity physics marks the difference between tokamaks with 3D ideal perturbations and general 3D stellarator geometry. We then present the analytical background ion flows and heat flux of interest, as well as the known geometrical factors (26), (33). The impurity flows and impurity flux are obtained with the effect of strong flows by extending the formalism in (51) (52).

In chapter 3, the code package composed of the VMEC and the VENUS-LEVIS codes is presented. The code package is used to numerically implement the framework described in

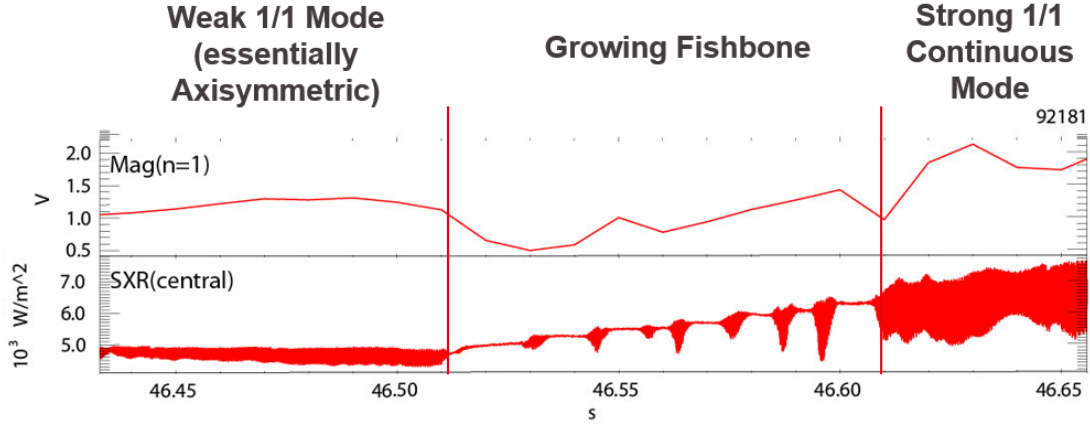


Figure 1.12 – Magnetic signal of the  $n = 1$  mode and central SXR tomography signal in JET pulse #92181.

chapter 2. This chapter again presents both known and new results. We start by explaining the main concepts behind the VMEC code (57), (58), (59). We then describe how we can model 3D MHD ideal saturated modes such as 1/1 internal kink modes with VMEC. We proceed to explain how the background ion flow and heat flux is calculated from the numerical equilibria obtained from the VMEC code. The numerical calculation of the 3D geometrical factors and background ion flows requires the numerical magnetic field configuration obtained from VMEC to be transformed to magnetic coordinates. The auxiliary codes developed in this thesis to convert from VMEC coordinates to Boozer or Hamada coordinates, as well as the codes developed to calculate the 3D geometrical factors and background ion flows, are presented. We then explain the guiding center formulation implemented in VENUS-LEVIS that allows for the following of heavy impurities in the presence of strong flows. A new implementation (based on (62)) of a suitable collision operator to treat both friction and thermal force between heavy impurities and main ions is then discussed.

In chapter 4, the main numerical results of our modelling are presented. The background ion flows in the presence of 1/1 internal kink are presented and discussed. This then facilitates a study into the effects of a 1/1 internal kink mode on heavy impurity accumulation. The saturated tungsten density is calculated as function of the different physical mechanisms involved in such operation scenarios. The transient phase of the simulations is analysed in order to obtain a measure of the diffusion coefficients in the presence of various physical mechanisms. The implications of these results are discussed in detail, and compared qualitatively with empirical observations.

Finally, in chapter 5, we summarise the work presented in this thesis and present future possible applications, such as the modelling of other 3D ideal MHD perturbations (like EHOs), as well as 3D MHD problems with modified topology (e.g. neoclassical tearing modes).

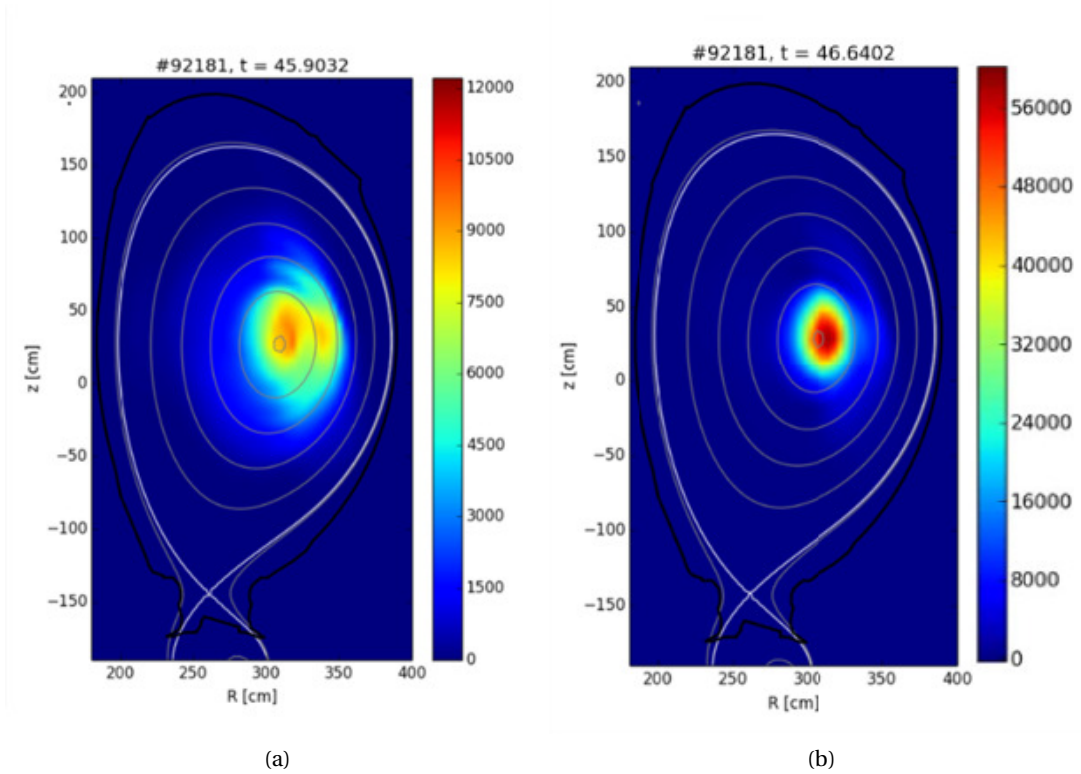


Figure 1.13 – Soft X-ray (SXR) tomography at different times of JET pulse #92181. (a) SXR signal at  $t \approx 45.9$ s of fig. 1.12, where the  $n = 1$  magnetic signal is weak and thus the plasma is essentially axisymmetric. (b) SXR signal at  $t \approx 46.63$ s of fig. 1.12, where the  $n = 1$  magnetic signal is strong and thus a strong 1/1 internal kink mode is present in the plasma. The axis position is given by the highest intensity region since impurities follow the axis of the kink.



## 2 Analytical model for the study of heavy impurity transport in the presence of 3D MHD ideal perturbations

This chapter presents a theoretical framework for studying heavy impurity transport in the presence of 3D MHD ideal saturated modes, strong flows, and ambipolar electric field. The chapter reviews known results and novel theories that are crucial for this thesis. The known results are presented here because they are necessary to understand the new theoretical formulation presented for heavy impurity transport. We start by presenting the basic equations for three different ways of describing the plasma. The particle description, the multi-fluid description and the MHD description. The concept of flux coordinates is then obtained from the MHD description. Following these basic concepts, we discuss the orderings for the background ions and heavy impurities that are relevant to treat heavy impurity transport in tokamak geometry with 3D MHD saturated perturbations. The background ion flow and heat flux are obtained by following these orderings. The drift kinetic formalism is then presented, because part of the ion background flows and heat flux results from its usage. A revision of the meaning of the geometrical factors involved in plasmas with such flows in the context of drift kinetic theory is performed. A derivation of the heavy impurity flux in tokamak configurations with 3D MHD ideal saturated modes, strong flows and heavy impurity transport is then made. The chapter ends with the derivation of the guiding center equations for the heavy impurities in the presence of strong flows.

### 2.1 Particle description

The most elementary way of describing a plasma is to describe the trajectories of all the particles in phase space which comprises both spatial coordinates given by  $\mathbf{x}$  and the velocity space  $\mathbf{v}$ , and the time  $t$ . The description of the movement of the particle trajectories in phase space provides a full description of the plasma. This description is usually called a kinetic description (9). In this microscopic description, the plasma is fully described by the distribution function  $f_s(\mathbf{x}, \mathbf{v}, t)$  of each species  $s$  in the plasma. The distribution function is a measure of the probability density of a particle of species  $s$  being located at the position  $\mathbf{x}$  with a velocity  $\mathbf{v}$  at a time  $t$ . The time evolution of such distribution function is given by the

Boltzmann<sup>1</sup> equation

$$\frac{df_s}{dt} = C(f_s) + S_s \Leftrightarrow \frac{\partial f_s}{\partial t} + \mathbf{v} \cdot \nabla_{\mathbf{x}} f_s + \frac{\mathbf{F}_s}{m_s} \cdot \nabla_{\mathbf{v}} f_s = C(f_s) + S_s, \quad (2.1)$$

in which the position and velocity coordinates are independent of each other. Here,  $m_s$  is the mass of a particle of species  $s$  and  $\mathbf{F}_s = q_s \mathbf{E} + q_s \mathbf{v} \times \mathbf{B}$  is the Lorentz force felt by a particle of species  $s$  with charge  $q_s$  in the presence of an electric field  $\mathbf{E}$  and a magnetic field  $\mathbf{B}$ .  $C(f_s)$  is the collision operator that describes collisions of the particles of species  $s$  with the other particles present in the plasma, and  $S_s$  any possible source terms. This description of the plasma species is often difficult to solve analytically, and its numerical treatment requires the usage of immense numerical resources since, a large number of numerical markers have to be modelled in both time and in 6 phase space coordinates. It is often necessary to find simplified and reduced methods of describing the plasma.

## 2.2 Fluid description

A macroscopic description of the plasma can be obtained by averaging the behaviour of each species over velocity space. The plasma is then described as a being composed of different fluids. Each fluid associated to species  $s$  is described by a macroscopic density  $n_s(\mathbf{x}, t)$ , flow  $\mathbf{U}_s(\mathbf{x}, t)$  and pressure  $P_s(\mathbf{x}, t)$ . The fluid equations are obtained by taking moments of the Boltzmann equation ((9), (20)), i.e. taking integrals on the velocity space of equation 2.1 multiplied by different powers of  $\mathbf{v}$ .

The scalar moment of order 0 gives the continuity equation

$$\frac{\partial n_s}{\partial t} + \nabla \cdot (n_s \mathbf{U}_s) = S_p, \quad (2.2)$$

in which  $n_s$  is defined as

$$n_s = \int d\mathbf{v} f_s, \quad (2.3)$$

$\mathbf{U}_s$  as

$$\mathbf{U}_s = \frac{1}{n_s} \int d\mathbf{v} f_s \mathbf{v} \quad (2.4)$$

and  $S_p$  are possible averaged source of particles. If we take the  $m\mathbf{v}$  vectorial moment of the Boltzmann equation, the momentum equation is obtained

---

<sup>1</sup>In section 3.2.2 we will use a numerical collision operator that effectively will approximate  $C(f_s)$  by the sum of a drift and a diffusion operators. In this case, this equation would be called Fokker-Planck equation

$$n_s m_s \frac{\partial \mathbf{U}_s}{\partial t} + n_s m_s \mathbf{U}_s \cdot \nabla \mathbf{U}_s = q_s n_s (\mathbf{E} + \mathbf{U}_s \times \mathbf{B}) - \nabla P_s - \nabla \cdot \overleftrightarrow{\pi}_s + \mathbf{F}_{r_s} + \mathbf{S}_m, \quad (2.5)$$

where  $P_s$  is the pressure of species  $s$  defined as

$$P_s = \int d\mathbf{v} \frac{m_s w^2}{3} f_s \quad (2.6)$$

in which  $\mathbf{w} = \mathbf{v} - \mathbf{U}_s$ . The viscosity force is  $\nabla \cdot \overleftrightarrow{\pi}_s$  with the viscous-stress (traceless) tensor defined as

$$\overleftrightarrow{\pi}_s = \int d\mathbf{v} \left( \mathbf{w} \mathbf{w} - w^2 \frac{\overleftrightarrow{\mathcal{I}}}{3} \right) f_s \quad (2.7)$$

with  $\overleftrightarrow{\mathcal{I}}$  is the identity matrix. If the plasma fluid has a strong flow velocity such that  $U_s \sim v_{th_s}$ , with  $v_{th_s} = \sqrt{\frac{2P_s}{n_s m_s}}$  the thermal velocity of species  $s$ , then this tensor can be written as (9)

$$\overleftrightarrow{\pi}_s = \mu_d W_{ij} + \mu_v \nabla \cdot \mathbf{U}_s \overleftrightarrow{\mathcal{I}} = \mu_d \left( \frac{\partial U_{s_i}}{\partial x_j} + \frac{\partial U_{s_j}}{\partial x_i} + \delta_{ij} \frac{2}{3} \nabla \cdot \mathbf{U}_s \right) + \mu_v \nabla \cdot \mathbf{U}_s \overleftrightarrow{\mathcal{I}}, \quad (2.8)$$

in which  $\mu_d$  and  $\mu_v$  are respectively the sheer and bulk viscosity coefficients (for plasmas, usually  $\mu_d \sim 1$  and  $\mu_v \sim 0$ ) and  $W_{ij}$  is the rate-of-strain tensor. If  $U_s \ll v_{th_s}$ , the viscosity tensor in the longitudinal direction can often be approximated by

$$\overleftrightarrow{\pi}_s = \mu_d W_{ij} \left( \hat{b}_i \hat{b}_j - \frac{\mathcal{I}}{3} \right) = (P_{\parallel} - P_{\perp}) \left( \hat{b} \hat{b} - \frac{\mathcal{I}}{3} \right) \quad (2.9)$$

in which  $P_{\parallel_s}$  and  $P_{\perp_s}$  are the components of the pressure tensor in the directions parallel and perpendicular to the magnetic field, respectively. Repeated indexes means summation and  $\hat{b} = \frac{\mathbf{B}}{B}$  is the unit vector in the direction of the magnetic field. If the pressure is isotropic ( $P_{\parallel_s} - P_{\perp_s} = 0$ ) we may define a temperature  $T_s = P_s / n_s$ . The friction force is obtained from the distribution function as

$$\mathbf{F}_{r_s} = \int d\mathbf{v} M_s \mathbf{v} C(f_s) \quad (2.10)$$

and  $\mathbf{S}_m$  are possible averaged sources of momentum. The momentum equation in conjunction with the continuity equation allow the calculation of flow for species  $s$  which obeys to both quasi-neutrality and ambipolarity provided that expressions for higher moments (pressure, viscous tensor, and friction force) are given or obtainable through, e.g. from kinetic or fluid description. The component of the momentum equation perpendicular to the magnetic field 2.5 can be used to obtain the perpendicular flow. The parallel flow can then be obtained from the continuity equation 2.2. The parallel component of the momentum equation 2.5 allows, in conjunction with quasi-neutrality, to obtain parallel corrections to the density  $n_s$  and the electric field  $E$ . At a different ordering, the same parallel component will help obtaining

constraints to be imposed to the flow, due to the action of the parallel viscosity. And finally, from taking the toroidal component of the momentum equation, taking an average over the poloidal and toroidal angles, and summing over all species  $s$ , one obtains the ambipolarity constraint. It is basically an equation which defines the radial ambipolar electric field required for the sum of the cross-field flux  $q_s \Gamma_r$  multiplied by the charge of the particles to vanish, i.e. for the radial current density  $J_r$  in the plasma to vanish. Here, the subscript  $r$  indicates the direction of the minor radius of the toroidal section of the toroidal magnetic device. The cross-field flux is defined for toroidal coordinates as

$$q_s \Gamma_r = q_s n_s \mathbf{U}_{s_r}. \quad (2.11)$$

The energy equation is obtained by taking the  $(v^2 m_s)/2$  moment of the Boltzmann equation, and is written as

$$\frac{\partial}{\partial t} \left( \frac{3}{2} P_s + n_s m_s U_s^2 \right) + \nabla \cdot \left[ \mathbf{q}_s + (\vec{\Pi}_s + P_s \vec{\mathcal{J}}) \cdot \mathbf{U}_s + \frac{1}{2} n_s m_s U_s^2 \mathbf{U}_s + \frac{3}{2} P_s \mathbf{U}_s \right] = \mathcal{Q}_J + (q_s n_s \mathbf{E} + \mathbf{F} r_s) \cdot \mathbf{U}_s + S_E, \quad (2.12)$$

in which the heat flux is defined as

$$\mathbf{q}_s = \int d\mathbf{v} \mathbf{w} \frac{m_s w^2}{2} f_s, \quad (2.13)$$

and where the collisional energy exchange is

$$\mathcal{Q}_J = \int d\mathbf{v} \frac{m_s w^2}{2} C(f_s) \quad (2.14)$$

and  $S_E$  are possible averaged sources of energy. Taking the moment  $\frac{m_s v^2}{2} \mathbf{v}$  of the Boltzmann equation, the energy flux equation is obtained and can be written as

$$\begin{aligned} \frac{\partial \mathbf{Q}_s}{\partial t} = & \frac{q_s}{m_s} \mathbf{E} \cdot \left[ \left( \frac{5}{2} P_s + \frac{1}{2} n_s m_s U_s^2 \right) \vec{\mathcal{J}} + \vec{\pi}_s + \frac{1}{2} m_s n_s \mathbf{U}_s \mathbf{U}_s \right] + \frac{1}{c} \frac{q_s}{m_s} \mathbf{Q}_s \times \mathbf{B} \\ & - \nabla R_s - \nabla \cdot \vec{\mathcal{R}}_s + \frac{P_s}{n_s} \left( \frac{5}{2} \mathbf{F} r_s + \mathbf{H}_s \right) + \mathbf{S}_q \end{aligned} \quad (2.15)$$

where the energy flux is defined as

$$\mathbf{Q}_s = \int d\mathbf{v} \mathbf{v} \frac{m_s v^2}{2} f_s = \mathbf{q}_s + (\vec{\pi}_s + P_s \vec{\mathcal{J}}) \cdot \mathbf{U}_s + \frac{1}{2} n_s m_s U_s^2 \mathbf{U}_s + \frac{3}{2} P_s \mathbf{U}_s, \quad (2.16)$$



the energy stress is

$$R_s = \frac{5P_s^2}{2n_s m_s}, \quad (2.17)$$

the energy stress anisotropic tensor is approximated by (neglecting off diagonal terms in coordinates aligned with the magnetic field line):

$$\overleftrightarrow{\mathcal{R}}_s = (R_{\parallel_s} - R_{\perp_s})(\hat{b}\hat{b} - \frac{\overleftrightarrow{\mathcal{I}}}{3}), \quad (2.18)$$

where  $R_{\parallel_s}$  and  $R_{\perp_s}$  are the longitudinal components of the energy stress tensor. The heat friction force (or thermal force) is given by

$$\mathbf{H}_s = \int d\mathbf{v} m_s \mathbf{v} \left( \frac{v^2}{v_{th_s}^2} - \frac{5}{2} \right) C(f_s) \quad (2.19)$$

and  $S_q$  are possible averaged energy flux sources. The energy equation 2.12 and the energy flux 2.15 can be used to obtain the heat flux vector of species  $s$  provided a closure is given for the heat friction, the energy stress anisotropic tensor, the friction force, and the viscosity tensor. Equation 2.15 allows the perpendicular heat flux  $\mathbf{q}_s$  to be obtained, and equation 2.12 gives the parallel heat flux. We can also write the equation that states the evolution of entropy in the plasma which in the fluid limit is written (on averaging with  $\ln f_s - 1$ ) as

$$\frac{\partial S_s}{\partial t} + \nabla \cdot \mathbf{S}_s = \Theta_s, \quad (2.20)$$

where the entropy density is approximated on closure as

$$S_s = n_s \ln \left( \frac{T_s^{\frac{3}{2}}}{N_s} \right), \quad (2.21)$$

the entropy flux vector is

$$\mathbf{S}_s = S_n \mathbf{U}_s + \frac{\mathbf{q}_s}{T_s}, \quad (2.22)$$

and the heat viscosity tensor is

$$\overleftrightarrow{\Theta}_s = \frac{m_s}{T_s} (R_{\parallel_s} - R_{\perp_s}) (\hat{b}\hat{b} - \frac{1}{3} \overleftrightarrow{\mathcal{I}}) - \frac{5}{2} (P_{\parallel_s} - P_{\perp_s}) (\hat{b}\hat{b} - \frac{1}{3} \overleftrightarrow{\mathcal{I}}). \quad (2.23)$$

The entropy equation 2.20 is used to obtain constraints relating both the density and the pressure of the fluid. These plasma fluid equations are thus important to obtain the flow and heat flux of background ions as well as the impurity flow. It is important to remark here that generally there are an infinite number of fluid equations and they are not closed. For example, the equations just presented depend on unknown higher moments of the distribution function, e.g. the viscous tensor as well as the collisional friction force when calculating the  $\nu$  moment of  $f_s$  (see equation 2.5). In order to obtain a closed solution for the flows and the heat flux, further assumptions have to be made about these quantities or they have to be calculated from a model (simplified) kinetic description (see section 2.6).

### 2.3 MHD description

The fluid description of the last section simplifies considerably the description of the plasma compared with the kinetic description (provided a suitable closure is provided). However, a plasma in the presence of a magnetic field is often described in an even more simplified way, we can look at the plasma as a single charged fluid with a total mass density

$$\rho = \sum_s n_s m_s, \quad (2.24)$$

a plasma velocity

$$\mathbf{U} = \frac{1}{\rho} \sum_s n_s m_s \mathbf{U}_s, \quad (2.25)$$

a total current density

$$\mathbf{J} = \sum_s n_s q_s \mathbf{U}_s, \quad (2.26)$$

and a total isotropic pressure

$$P = \sum_s n_s T_s. \quad (2.27)$$

This description of the plasma is called magnetohydrodynamics or MHD (3). The MHD continuity equation is then obtained by summing the continuity equation 2.2, in the absence of source terms, for all species  $s$ , and is given by

$$\frac{\partial \rho}{\partial t} + \nabla \cdot (\rho \mathbf{U}) = 0, \quad (2.28)$$

The MHD force balance equation is obtained from summing the momentum equation 2.5 for all species  $s$  which yields

$$\rho \left( \frac{\partial \mathbf{U}}{\partial t} + \mathbf{U} \cdot \nabla \mathbf{U} \right) = \mathbf{J} \times \mathbf{B} - \nabla P \quad (2.29)$$

in the absence of pressure anisotropies, source terms and viscous-stress terms. The system of fluid equations is closed by the adiabatic equation which is written as

$$\frac{d}{dt} \left( \frac{P}{\rho^\gamma} \right) \equiv \frac{\partial}{\partial t} \left( \frac{P}{\rho^\gamma} \right) + \mathbf{U} \cdot \nabla \left( \frac{P}{\rho^\gamma} \right) = 0. \quad (2.30)$$

The momentum equation approximation also includes the ideal Ohm's in the limit of zero collisional resistivity

$$\mathbf{E}' = \mathbf{E} + \mathbf{U} \times \mathbf{B} = 0, \quad (2.31)$$

in which  $\mathbf{E}'$  is the electric field felt in the single fluid frame moving with the plasma velocity  $\mathbf{U}$ . The Ampère's law, is given as usual in the limit of non-relativistic particles as

$$\mu_0 \mathbf{J} = \nabla \times \mathbf{B}, \quad (2.32)$$

with  $\mu_0$  the magnetic permeability of the vacuum. The Gauss law for the magnetic field states as usual the zero divergence of the magnetic field:

$$\nabla \cdot \mathbf{B} = 0. \quad (2.33)$$

The Gauss law for the electric field on scales larger than a so-called Debye length is

$$\nabla \cdot \mathbf{E} = 0, \quad (2.34)$$

which states that the plasma is quasi-neutral, giving the the quasi-neutrality condition

$$\sum_s n_s q_s = 0. \quad (2.35)$$

In the stationary limit ( $\frac{\partial}{\partial t} \rightarrow 0$ ), and in the absence of strong flows and time varying fluctuations, we obtain the simpler form of the MHD force balance equation

$$\mathbf{J} \times \mathbf{B} = \nabla P, \quad (2.36)$$

which is a balance between the magnetic force felt by the plasma and the pressure force exerted by the plasma. Typically, this is the equation that is solved in order to obtain magnetic configurations of equilibrium for magnetic confinement devices such as tokamaks and stellarators. In such cases, the charged fluid represents the sum of the hydrogen (isotopes) or helium ions, and electrons composing the background plasma in such fusion devices. The importance of equation 2.36 will be seen later when describing the numerical tool VMEC which solves equation 2.36 to obtain numerical solutions of magnetic configurations representing stable equilibria of tokamak configurations with 3D MHD ideal saturated modes. The existence of a system of coordinates called flux coordinates is important for simplifying the calculations of many areas in this thesis.

## 2.4 Flux coordinates

We can now discuss one important implication of the MHD description due to the fact that the magnetic field of an MHD equilibrium is constrained by the equations 2.36, 2.32, and 2.33. Such equations imply that the equilibrium magnetic field configuration established in the plasma has a special relation to the density current and the pressure of the plasma. This allows the plasma to be more easily described in a set of spatial coordinates called flux coordinates (63), (64), (65), (66). These special set of coordinates are important as they often simplify calculations. Equation 2.32 leads to the constraint

$$\nabla \cdot \mathbf{J} = 0. \quad (2.37)$$

Moreover, 2.36 implies the following constraints

$$\mathbf{J} \cdot \nabla P = 0 \quad (2.38)$$

and

$$\mathbf{B} \cdot \nabla P = 0. \quad (2.39)$$

These constraints mean that in a magnetic field configuration which obeys the MHD force balance equation, the current density and magnetic field vectors lie on surfaces of constant pressure. This implies that each of these surfaces have an associated magnetic flux and total current. This is so because the magnetic field and density current vector fields have zero divergence, and thus the same magnetic field lines and current lines will stay on the same surface along the entirety of the torus. We then call these surfaces flux surfaces. Another equivalent meaning of these constraints is that if we describe the magnetic field and current

density in a set of general flux coordinates  $(s, \theta, \phi)$ , where  $s^2$  is a radial coordinate that labels the flux surface, then the magnetic field and the current density across flux surfaces vanish which can be mathematically written as  $B^s = 0$  and  $J^s = 0$ . Here,  $\theta$  and  $\phi$  can be any arbitrary poloidal and toroidal angles. Provided the coordinate system chosen is based on flux coordinates  $(s, \theta, \phi)$  the constraints  $B^s = 0$  and  $J^s = 0$  greatly simplify the description of problems in the MHD description. If we assume that the toroidal magnetic equilibrium described by such equations can be represented by these flux surfaces in a way that they are nested surfaces with a single magnetic axis, then we can describe the pressure as being function of only the radial variable  $s$ :

$$P = P(s). \quad (2.40)$$

Equations 2.33 and 2.39 imply that a potential function  $v^*$  exists such that the contravariant magnetic field is of the form

$$\mathbf{B} = \nabla s \times \nabla v^*. \quad (2.41)$$

Equations 2.37 and 2.38 imply that a potential function  $w^*$  exists such that the contravariant current density is of the form

$$\mathbf{J} = \nabla w^* \times \nabla s. \quad (2.42)$$

This form of the current density vector in conjunction with Faraday's law 2.32 implies that a potential function  $u^*$  exists such that the covariant magnetic field is of the form

$$\mathbf{B} = \nabla u^* + w^* \nabla s. \quad (2.43)$$

The definitions of poloidal and toroidal magnetic flux inside a poloidal and toroidal flux surface labelled by  $s$  are given by

$$2\pi\Psi_P(s) = \int \int B^\theta ds d\phi \quad (2.44)$$

and

$$2\pi\Psi_T(s) = \int \int B^\phi ds d\theta. \quad (2.45)$$

As such the form of potential function  $v^*$  has to be

$$v^*(s, \theta, \phi) = \frac{d\Psi_T}{ds}\theta - \frac{d\Psi_P}{ds}\phi + \tilde{v}(s, \theta, \phi), \quad (2.46)$$

in which  $\tilde{v}(s, \theta, \phi)$  is an arbitrary periodic function in  $\theta$  and  $\phi$ .

---

<sup>2</sup> $s$  is not to be confused with the subscript for species

The definitions of poloidal and toroidal current (multiplied by  $\mu_0$ ) passing through a poloidal and toroidal flux surface labelled by  $s$  are given by

$$2\pi I_P(s) = \int \int \mu_0 J^\theta ds d\phi \quad (2.47)$$

and

$$2\pi I_T(s) = \int \int \mu_0 J^\phi ds d\theta, \quad (2.48)$$

and lead in a similar fashion to the following form for the potential function  $w^*$

$$w^*(s, \theta, \phi) = -\frac{dI_T}{ds}\theta - \frac{dI_P}{ds}\phi + \tilde{w}(s, \theta, \phi), \quad (2.49)$$

in which  $\tilde{w}(s, \theta, \phi)$  is again an arbitrary periodic function in  $\theta$  and  $\phi$ . Faraday's law 2.32 then implies that the potential function  $u^*$  is

$$u^*(s, \theta, \phi) = I_T\theta + I_P\phi + \tilde{u}(s, \theta, \phi), \quad (2.50)$$

with  $\tilde{u}(s, \theta, \phi)$  an arbitrary periodic function in  $\theta$  and  $\phi$ . These potential functions define an arbitrary set of flux coordinates. Choosing specific forms of the functions  $\tilde{v}(s, \theta, \phi)$ ,  $\tilde{w}(s, \theta, \phi)$  and  $\tilde{u}(s, \theta, \phi)$  will lead to different choice of  $\theta$  and  $\phi$  coordinates. Each set of flux coordinates  $(s, \theta, \phi)$  is a valid set of coordinates to describe an equilibrium magnetic field which is a solution of the MHD force balance equation 2.36. However, some flux coordinates offer specific advantages. The choice being made depends on the problem that is presented. Sometimes, we may need to solve magnetic differential equations (see appendix A) which have a magnetic differential operator  $\mathbf{B} \cdot \nabla$ . It is clear that this operator is treated in a simpler way if the contravariant components  $B^\theta(s, \theta, \phi) = \mathbf{B} \cdot \nabla\theta$  and  $B^\phi(s, \theta, \phi) = \mathbf{B} \cdot \nabla\phi$  of the magnetic field are flux functions such that  $\langle B^\theta \rangle = B^\theta$  and  $\langle B^\phi \rangle = B^\phi$ . In which case the flux average for a function  $\varkappa(s, \theta, \phi)$  is defined as

$$\langle \varkappa(s, \theta, \phi) \rangle(s) = \frac{\int_0^{2\pi} \int_0^{2\pi} \varkappa(s, \theta, \phi) \sqrt{g} d\theta d\phi}{\int_0^{2\pi} \int_0^{2\pi} \sqrt{g} d\theta d\phi} = \frac{\int_0^{2\pi} \int_0^{2\pi} \varkappa(s, \theta, \phi) \sqrt{g} d\theta d\phi}{V'}. \quad (2.51)$$

Here,  $\sqrt{g}(s, \theta, \phi) = (\nabla s \cdot \nabla\theta \times \nabla\phi)^{-1}$  is the jacobian in the set of flux coordinates  $(s, \theta, \phi)$  and  $V(s)$  is the volume enclosed by the flux surface labelled by  $s$  such that the differential volume element is  $dV = \sqrt{g} ds d\theta d\phi$ . We also define for an arbitrary flux function  $v(s)$  the following notation  $\varkappa'(s) = \frac{dv}{ds}$ . The sets of flux coordinates in which the contravariant components of  $B^x$  multiplied by the jacobian  $\sqrt{g}$  are flux functions are called straight field line coordinates as the representation of the field lines in the  $(\theta, \phi)$  plane are straight lines. Since, from 2.41, the magnetic field lines are defined by the intersection of a flux surface  $s$  and a surface in which  $v^*$  is constant it is clear to see that straight field line coordinate systems are obtained when imposing  $\tilde{v} = 0$ . The simplest set of coordinates that can be obtained without considering the

trivial case (with  $v^* = u^* = w^* = 0$ ) are obtained by imposing  $v^* = u^* = 0$  or  $v^* = w^* = 0$ . The former are called Boozer coordinates (64), (65) and the latter Hamada coordinates (66).

Boozer coordinates  $(s, \theta_B, \phi_B)$  are straight field line coordinates with a simple representation of the covariant component of the magnetic field such that

$$\mathbf{B} = \frac{d\Phi_T}{ds} \nabla s \times \nabla \theta_B - \frac{d\Phi_P}{ds} \nabla s \times \nabla \phi_B = \nabla \Phi_T \times \nabla \theta_B - \iota \nabla \Phi_T \times \nabla \phi_B, \quad (2.52)$$

$$\mathbf{J} = \frac{dI_T}{ds} \nabla s \times \nabla \theta_B + \frac{dI_P}{ds} \nabla s \times \nabla \phi_B + \nabla \tilde{w}_B \times \nabla \phi_B, \quad (2.53)$$

$$\mathbf{B} = \tilde{w}_B \nabla s + I_T \nabla \theta_B + I_P \nabla \phi_B, \quad (2.54)$$

$$\sqrt{g_B} = \frac{d\Phi_T}{ds} \frac{I_P + \iota I_T}{B^2}, \quad (2.55)$$

with  $\iota(s) = \frac{d\Phi_P}{d\Phi_T} = \frac{1}{q(s)}$  the rotational transform,  $q(s)$  being the safety factor, and  $\tilde{w}_B(s, \theta_B, \phi_B)$  the respective function  $\tilde{w}$  of Boozer coordinates.

Hamada coordinates  $(s, \theta_H, \phi_H)$  have the particularity of being straight field line coordinates in which the current lines are also straight and the jacobian  $\sqrt{g_H}$  is a flux function. In Hamada coordinates we can write

$$\mathbf{B} = \nabla \Phi_T \times \nabla \theta_H - \iota \nabla \Phi_T \times \nabla \phi_H, \quad (2.56)$$

$$\mathbf{J} = \frac{dI_T}{ds} \nabla s \times \nabla \theta_H + \frac{dI_P}{ds} \nabla s \times \nabla \phi_H, \quad (2.57)$$

$$\mathbf{B} = \frac{\partial \tilde{u}_H}{\partial s} \nabla s + \left( I_T + \frac{\partial \tilde{u}_H}{\partial \theta_H} \right) \nabla \theta_H + \left( I_P + \frac{\partial \tilde{u}_H}{\partial \phi_H} \right) \nabla \phi_H, \quad (2.58)$$

$$\sqrt{g_H} = \frac{V'}{(2\pi)^2}. \quad (2.59)$$

Further details on the derivations of these expressions as well as the transformations between the different sets of flux coordinates can be found in the appendix A. In the remainder of this chapter, the notation  $(\psi, \theta, \phi)$  for a set of flux coordinates will be used in which  $\psi = \Psi_T$  is the flux label coordinate (instead of  $s$ ).

In the case of axisymmetry, the derivatives of all scalars with respect to the toroidal angle are null ( $\frac{\partial}{\partial \phi} \rightarrow 0$ ), which means that in general the contravariant and covariant forms of the magnetic field can be given by

$$\mathbf{B} = \left( q(\psi) + \frac{\partial \tilde{v}}{\partial \theta} \right) \nabla \Phi_P \times \nabla \theta + \nabla \phi \times \nabla \Phi_P, \quad (2.60)$$

$$\mathbf{B} = \frac{\partial \tilde{u}}{\partial \Phi_P} \nabla \Phi_P + \left( I_T + \frac{\partial \tilde{u}}{\partial \theta} \right) \nabla \theta + I_P \nabla \phi. \quad (2.61)$$

In the cylindrical system of coordinates  $(R, \phi_{geo}, Z)$ , the toroidal angle is chosen to be the

usual geometrical angle  $\phi_{geo}$ . Since the potential functions in axisymmetry are independent of the toroidal angle, we may substitute the general coordinate  $\phi$  by  $\phi_{geo}$  in 2.60 and 2.61. This implies then that  $B_{\phi_{geo}} = I_P(\Phi_P)$ , and that the poloidal magnetic field component is then given from 2.60 by  $\mathbf{B}_P = \nabla\phi \times \nabla\Phi_P$ , since the first term is in the toroidal direction. The magnetic field in cylindrical coordinates is written as

$$\mathbf{B} = |B_R|\hat{R} + |B_Z|\hat{Z} + |B_{\phi_{geo}}|\hat{\phi}_{geo} = \mathbf{B}_P + B_{\phi_{geo}}\nabla\phi_{geo}, \quad (2.62)$$

which makes the axisymmetric magnetic field in flux coordinates

$$\mathbf{B} = \nabla\phi \times \nabla\Phi_P + I_P\nabla\phi. \quad (2.63)$$

This is the standard way to write the axisymmetric magnetic field (9). Notice that changing  $\phi$  for  $\phi_{geo}$  changes the  $\theta$  angle as well as the functions  $\tilde{v}$  and  $\tilde{u}$ , but these changes have no effect on this way of writing the axisymmetric magnetic field.

## 2.5 Ordering of the background ions and heavy impurities

In this thesis, we assume the plasma to be composed of a background ion species  $I$ , background electrons  $e$ , and a heavy impurity species  $W$  (tungsten being the impurity of interest). One aim of this thesis is to model the particular case of a 1/1 internal kink mode in the core of a tokamak such as the one shown in section 1.7. The background species are thus assumed to be in the low collisionality regime as it is often the case in the tokamak core. The high collisionality is ususally appropriate for the heavy impurities with high charge number  $Z_W$  in the core of tokamaks. It is usual to consider that the banana regime (in which trapped particles have banana trajectories) exists at low collisionality in axisymmetric devices. Nevertheless, axisymmetry can often be broken by the existence of 3D MHD perturbations. In such cases other types of trapped particles can exist leading to the occurrence of different low collisionality regimes (26) (see section 1.5). In the presence of 3D MHD ideal perturbations like the 1/1 internal kink both banana trapped particles and helically trapped particles exist. We will consider that the collisionality is sufficiently high to not allow for the drift of helically trapped particles to dominate neoclassical transport of the ions. Neoclassical transport is thus predominantly due to banana trapped particles. In this way, we can make use of the general 3D geometry formalisms of (33) and (26) to calculate the parallel ion flows. Such a scenario represents the so-called  $1/\hat{v}_{ii}$  regime (see section 1.5) and as discussed in (20), it should be the most appropriate regime when axisymmetry is broken in tokamaks. The collisionality is here defined as

$$\hat{v}_{II} = v_{II} \frac{L_{\parallel}}{v_{T_I}}, \quad (2.64)$$

with  $L_{\parallel}$  the macroscopic length associated with gradients along the magnetic field line,  $v_{T_s} =$



## 2.5. Ordering of the background ions and heavy impurities

$\sqrt{2T_s/m_s}$  the thermal velocity of species  $s$ , and

$$\nu_{sk} = \frac{n_s Z_s^2 Z_k^2 e^4 \ln \Lambda}{(4\pi\epsilon_0)^2 m_s^2 \nu_{T_s}^2}, \quad (2.65)$$

is the typical collision frequency between species  $s$  and  $k$ . Here,  $\nu_{T_s}$  is the thermal velocity of electrons or ions (whichever is larger),  $\epsilon_0$  is the vacuum permittivity,  $Z_s$  is the charge number of species  $s$ ,  $e$  is the electron charge and  $\ln \Lambda$  is the Coulomb logarithm (see tables in (67)). In the  $1/\hat{\nu}_{ii}$  regime, the collisionality  $\hat{\nu}_{ii}$  satisfies  $(\delta B/B_{AXI})^{3/2} < \hat{\nu}_{ii} < \epsilon^{3/2}$ , with  $\epsilon$  the inverse aspect ratio,  $B_{AXI}$  the magnitude of the axisymmetric magnetic field, and  $\delta B$  the magnitude of the 3D ideal MHD perturbation (20). Following (49), (47), we use the small parameter  $\delta$  describing the smallness of the Larmor radius relative to the scale length of the magnetic field  $L_\perp$  as usual for neoclassical transport theory

$$\delta = \frac{\rho_{\theta_I}}{L_\perp} \ll 1. \quad (2.66)$$

We define the square of the toroidal Mach number of a species  $s$  as

$$M_s^2 = \frac{m_s \Omega^2 R^2}{2T_s}, \quad (2.67)$$

where  $R$  is the cylindrical radial coordinate, and  $\Omega$  is the common toroidal angular frequency with which all species rotate due to the balance between the momentum supplied from neutral beam injection and diffusion due to turbulent sources (68). Tungsten diverted tokamak experiments with unbalanced beam injection (like in the example in 1.7) show that impurities rotate toroidally supersonically along the toroidal direction

$$M_W^2 \sim 1, \quad (2.68)$$

while main ions are subsonic which means (47)

$$M_I^2 \sim 1/Z_W \sim \delta^{1/2}. \quad (2.69)$$

The common velocity due to NBI is given by  $\mathbf{U} = \Omega R \hat{e}_\phi \sim \delta^{1/4} v_{th_I}$  (see equation 2.82). This flow is a combination of the lowest order  $E \times B$  velocity and the parallel velocity which is constrained by strong poloidal damping of the flow. This implies that at lowest order in ion gyro radius, we have an electric field of order  $\delta^{-3/4} T_I / (q_I L)$ . It is also known that ambipolarity between ions and electrons set an electric field which is of order  $\delta^0 T_I / (q_I L)$ , which produces an  $E \times B$  flow of the order of the diamagnetic velocity, which in turn is of order  $\delta v_{th_I}$ . Furthermore, a poloidal

electric field is generated due to quasi-neutrality and the movement of ions associated with the poloidal centrifugal force. This poloidal electric field has to be of the order  $T_I/(q_I L)M_I^2 \sim \delta^{1/2}T_I/(q_I L)$ . However, the ordering  $1/Z_W \sim \delta^{1/2} \ll 1$ , implies that  $q_W E_{1/2} \sim T_I/L$  and  $M_W^2 \sim 1$ , which means that the poloidal electrical force and centrifugal forces acting on heavy impurities with charge  $Z_W$  appear at zeroth order, contrary to what happens for the main ions. These forces will redistribute the impurity density poloidally around the flux surface. Since the redistribution appears at zeroth order in  $\delta$ , we have  $N_W(\psi) \sim \tilde{n}_w(\psi, \theta, \phi)$ . Nevertheless, since  $q_I E_{1/2} \sim \delta^{1/2}$  and  $M_I^2 \sim \delta^{1/2}$ , the same forces acting on ions will only appear at order  $\delta^{1/2}$ . We thus have  $\tilde{n}_I(\psi, \theta, \phi) \sim \delta^{1/2}N_I(\psi)$ . Here  $N_s = \langle n_s \rangle$  is the contribution to the density of species  $s$  that does not vanish on flux averaging the density, and  $\tilde{n}_s$  is the correction to the density, which necessarily varies along the magnetic field. We also assume  $N_W(\psi)/N_I(\psi) \sim 1/Z_W^2 \delta \sim \delta^2$  everywhere in the plasma, i.e. that impurities are in the trace limit and thus we neglect the effects of self collisions and the feedback of the impurities on the ions due to collisions. The quantities of interest can now be expanded using the ordering parameter  $1/Z_W \sim \delta^{1/2} \ll 1$  defined above.

The electric field can be written as

$$E(\psi, \theta, \phi) = E_{-3/4}(\psi) + E_0(\psi) + E_{1/2}(\psi, \theta, \phi) + \dots, \quad (2.70)$$

the flow of species  $s$  as

$$\mathbf{U}_s = \mathbf{U}_{s1/4} + \mathbf{U}_{s1} + \mathbf{U}_{s3/2} + \dots, \quad (2.71)$$

the heat flux of species  $s$  as

$$\mathbf{q}_s = \mathbf{q}_{s1/4} + \mathbf{q}_{s1} + \mathbf{q}_{s3/2} + \dots, \quad (2.72)$$

the density of the ions as

$$n_I(\psi, \theta, \phi) = N_{I0}(\psi) + \tilde{n}_{I1/2}(\psi, \theta, \phi), \quad (2.73)$$

and the impurity density as

$$n_W(\psi, \theta, \phi) = n_{W0}(\psi, \theta, \phi). \quad (2.74)$$

The stationary case is considered in which we neglect time derivatives in the bulk plasma and electromagnetic fields, and we assume that any source terms (e.g. ICRH) would enter only at

order  $\delta^2$ . Note that we consider briefly the possibility of a toroidal momentum source due to ECRH at order  $\delta$  in chapter 4 to explain ASDEX-U experiments.

## 2.6 Ion background flows

Following the orderings described above, we obtain the perpendicular components of the ion flow by forming the cross product of  $\mathbf{B}$  with the momentum equation 2.5 for the ions. At lowest order  $\delta^{3/4}$ , we obtain the flow of equation 2.5, i.e.

$$\mathbf{U}_{I_{1/4\perp}} = \frac{\mathbf{B} \times \nabla \Phi_{-3/4}}{B^2} = \mathbf{U}_{1/4\perp}, \quad (2.75)$$

which corresponds to the perpendicular common flow of all species due to the NBI induced rotation. At order  $\delta$  of the momentum equation 2.5 for the ions, we have

$$\mathbf{U}_{I_{1\perp}} = \frac{\mathbf{B} \times \nabla \Phi_0}{B^2} + \frac{\mathbf{B} \times \nabla P_{I_0}(\psi)}{q_I N_{I_0}(\psi) B^2} = \frac{\mathbf{B} \times \nabla \psi}{B^2} \omega_{I_0}(\psi), \quad (2.76)$$

which includes the  $\mathbf{E} \times \mathbf{B}$  velocity due to the ambipolar electric field (see section 1.5) and the lowest order diamagnetic ion flow. Here  $P_s = n_s T_s$  is the pressure of species  $s$ . At order  $\delta^{3/2}$  we have

$$\mathbf{U}_{I_{3/2\perp}} = \frac{\mathbf{B} \times \nabla \Phi_{1/2}}{B^2} + \frac{\mathbf{B} \times \nabla P_{I_{1/2}}(\psi, \theta, \phi)}{q_I n_I(\psi) B^2} - \frac{m_I}{q_I} \frac{\mathbf{B} \times [\mathbf{U}_{I_{1/4}} \cdot \nabla \mathbf{U}_{I_{1/4}}]}{B^2}, \quad (2.77)$$

which comprises the ion flow components associated with the centrifugal effects. We need the background ion flow at this order to allow for the calculation of  $\Phi_{1/2}$  due to the quasi-neutrality corrections (see section 2.9). However, we neglect this flow as a source of transport drive due to the subsonic character of the ion flow. This allows for the usage of the usual formalism to calculate the necessary parallel ion flow from usual drift kinetic formalism (33), (26) (see equations 2.86 and sections, 2.7 and 2.8). At the order  $\delta^{-3/4} \lambda_I / L$ , where  $\lambda_s$  is the mean free path of species  $s$ , we find a constraint for the velocity  $\mathbf{U}_{I_{1/4}}$  from the flux averaged parallel component of the momentum equation 2.5 for the background ions.

The constraint is given by the vanishing of the parallel viscosity due to the velocity  $\mathbf{U}_{I_{1/4}}$  as

$$\langle \mathbf{B} \cdot \nabla \cdot \boldsymbol{\pi}_{1/4} \rangle = 0 \quad (2.78)$$

where  $\nabla \cdot \boldsymbol{\pi}_{1/4}$  is the viscosity due to gradients in the common velocity  $\mathbf{U}_{I_{1/4}}$ . This constraint can be used with the continuity equation 2.2 for the ions at lowest order which is given by

$$\nabla \cdot (N_{I_0}(\psi) \mathbf{U}_{I_{1/4}}) = N_{I_0}(\psi) \nabla \cdot \mathbf{U}_{I_{1/4}} = 0. \quad (2.79)$$

Due to the incompressibility of  $\mathbf{U}_{I_{1/4}}$  the constraint 2.78 can be written (9)

$$\begin{aligned}
 \langle \mathbf{B} \cdot \nabla \cdot \boldsymbol{\pi}_{1/4} \rangle &= 0 \Leftrightarrow \frac{3}{2} \mu_D \langle W_{bb} \hat{\mathbf{b}} \cdot \nabla \mathbf{B} \rangle \\
 &\Rightarrow W_{bb} = 0 \\
 &\Leftrightarrow \hat{\mathbf{b}} \cdot \nabla \mathbf{U}_{-1/4} \cdot \hat{\mathbf{b}} - \nabla \cdot \mathbf{U}_{-1/4} = 0 \\
 &\Leftrightarrow \hat{\mathbf{b}} \cdot \nabla \mathbf{U}_{-1/4} \cdot \hat{\mathbf{b}} = 0
 \end{aligned} \tag{2.80}$$

in which  $W_{bb}$  is component  $\hat{\mathbf{b}}\hat{\mathbf{b}}$  of the rate of strain tensor written in coordinates where the vertical axis aligns with  $\hat{\mathbf{b}}$ . This constraint is equivalent to the one found for the parallel viscosity in (13), (9) in which the flow is considered to be strong. The constraint 2.80 implies the essential equation for  $\mathbf{U}_{I_{1/4}}$ :

$$\mathbf{U}_{I_{1/4}} \cdot \nabla \mathbf{B} = 0, \tag{2.81}$$

which states that the zeroth velocity exists only in the direction of invariant magnetic field strength, and thus avoids magnetic pumping. Since the 1/1 internal kink or any other 3D MHD saturated perturbation in tokamaks is in general not a quasi-symmetric field the only valid approximation to equation 2.81 is that the strong zeroth order flow will be a toroidal flow, given by

$$\mathbf{U}_{I_{1/4}} = E_{-3/4} R \hat{\mathbf{e}}_\phi = -\Phi'_{-3/4} R \hat{\mathbf{e}}_\phi = -\Omega R \hat{\mathbf{e}}_\phi, \tag{2.82}$$

where  $\Omega$  is the toroidal rotation,  $R$  is the major radius and the prime denotes the radial derivative of the flux coordinate  $\psi$ . This is a well known result for tokamaks as it is seen that poloidal strong flows are usually damped at the timescale of ion-ion collisions, which is much shorter than the cross-field transport timescales. This tokamak result appears to hold for plasmas with symmetry breaking at realistic amplitudes. The parallel main ion flow at order  $\delta$  can also be obtained in the fluid approach from the ion continuity equation 2.2 (at order  $\delta$ ):

$$\nabla \cdot (N_{I_0(\psi)} \mathbf{U}_{I_1}) = N_{I_0(\psi)} \nabla \cdot \mathbf{U}_{I_1} = 0. \tag{2.83}$$

From 2.83, we obtain the parallel ion flow at order  $\delta$

$$\mathbf{U}_{I_{1\parallel}} = \omega_I(\psi) \left( u(\psi, \theta, \phi) + K_I(\psi) \right) \mathbf{B}, \tag{2.84}$$

where  $\omega_I$  is defined from equation 2.76, and the function  $u(\psi, \theta, \phi)$  is obtained from the magnetic differential equation given by

$$\mathbf{B} \cdot \nabla u = -\mathbf{B} \times \nabla \psi \cdot \nabla \left( \frac{1}{B^2} \right), \quad (2.85)$$

with the constraint  $u(B_{max}(\psi)) = 0$  and  $K_I(\psi)$  an integration constant that is obtainable from solving the drift kinetic equation for the ions, and therefore depends on the collisional regime and the collisional operator adopted in any calculations. As we are interested in following the ions and impurities in the frame flowing with  $\mathbf{U}_{I1/4}$ , and since the bulk ion flow is subsonic, we may use the results obtained in (33) where the ion drift kinetic equation in the low collisional  $1/\nu$  regime for general 3D geometry was solved to find that the ion parallel flow at order  $\delta$  can be written as

$$\mathbf{U}_{I1\parallel} = \frac{T_i}{q_i} A_{I1} \left( u + \frac{f_s}{\langle B^2 \rangle} \right) \mathbf{B} + \frac{T_I}{q_I} (A_{I1} - \eta A_{I2}) \frac{f_c(f_s + \langle u B^2 \rangle)}{\langle B^2 \rangle f_t} \mathbf{B}, \quad (2.86)$$

where  $\eta \approx 1.17$ , and  $f_s$  is given by

$$f_s = \frac{3}{4} \frac{\langle B^2 \rangle}{B_{max}^2} \int_0^1 \frac{\langle g_4 \rangle \lambda d\lambda}{\langle \sqrt{1 - \lambda B / B_{max}} \rangle}, \quad (2.87)$$

where  $g_4$  is defined below. Also, the effective fraction of circulating particles  $f_c$  (which often appears in neoclassical transport, see (9)) is defined as

$$f_c = \frac{3}{4} \frac{\langle B^2 \rangle}{B_{max}^2} \int_0^1 \frac{\lambda d\lambda}{\langle \sqrt{1 - \lambda B / B_{max}} \rangle}, \quad (2.88)$$

i.e. 2.87 with  $\langle g_4 \rangle \rightarrow 1$ . The effective fraction of trapped particles is  $f_t = 1 - f_c$ , and the thermodynamic forces which drive ion transport can be written as

$$A_{I1} = \frac{d \ln P_I}{d\psi} + \frac{q_I}{T_I} \frac{d\Phi_0(\psi)}{d\psi}, \quad (2.89)$$

and finally,

$$A_{I2} = \frac{d \ln T_I}{d\psi}. \quad (2.90)$$

The function  $g_4$  is

$$g_4 = \xi \int_{l(B_{max})}^l \hat{\mathbf{b}} \times \nabla \psi \cdot \nabla \xi^{-1} dl', \quad (2.91)$$

where  $\xi = (1 - \lambda B/B_{max})^{1/2}$  is a pitch angle variable and  $\lambda = B_{max}\epsilon/\mu$  where  $\lambda < 1$ , and the integration is performed along a magnetic field line parametrised by the variable  $l$ . Here,  $\epsilon = mw_{\parallel}^2 + \mu B + q_I \Phi_0 + q_I \Phi_{1/2}$  and  $\mu = m_W w_{\perp}^2 / (2B)$  are respectively the energy and magnetic moment of a bulk ion in the frame rotating with  $\mathbf{U}_{I_{1/4}}$ , since the ions are subsonic. If we define  $g_4 = \xi g_5$ , then the function  $g_5$  is obtained from solving the magnetic differential equation

$$\mathbf{B} \cdot \nabla g_5 = \mathbf{B} \times \nabla \psi \cdot \nabla \left( \frac{1}{\xi} \right), \quad (2.92)$$

with  $g_5(B_{max}) = 0$ .

The energy flux equation 2.15 for the ions at order  $\delta^0$  yields the lowest order perpendicular ion heat flux

$$\mathbf{q}_{I_{\perp}} = -\frac{5}{2} P_I \frac{\mathbf{B} \times \nabla T_I}{q_I B^2}. \quad (2.93)$$

From the energy equation 2.12 for the ions one obtains

$$\nabla \cdot \mathbf{q}_{I_{\perp}} = 0, \quad (2.94)$$

which leads to the lowest order ion parallel flux given by

$$\mathbf{q}_{I_{\parallel}} = -\frac{5}{2} P_I \frac{T_i}{q_i} A_{I2} \left( u + \frac{f_s}{\langle B^2 \rangle} \right) \mathbf{B}. \quad (2.95)$$

Finally, using the entropy equation 2.20 for the ions we get the constraint

$$\mathbf{B} \cdot \nabla T_I = 0. \quad (2.96)$$

which states that the ion temperature is a flux function for any collisionality regime. This indicates that MHD equilibria with flow should always adopt an isothermal assumption, though it is not always favoured (e.g. for investigating classes of MHD instabilities in rotating plasmas). The background ion flow and heat flux are important for capturing the correct collisional effects between the impurities and the background ions. These flows can be calculated numerically for general 3D geometry (see section 3.1.5). They can then be used in the collision operator implementation in VENUS-LEVIS as we will see in chapter section 3.2.2.

## 2.7 The drift kinetic equation

Since the parallel ion flow 2.84 and ion heat flux 2.95 are obtained ultimately from the drift kinetic equation, we now briefly introduce the drift kinetic formalism. A fuller derivation

is given in the appendix B. We have seen that the plasma can be described by following the trajectories of every particle in the system through a distribution function  $f_s(\mathbf{x}, \mathbf{v}, t)$ . Such a distribution obeys, in general, to the Boltzmann equation in 2.1 as mentioned already. A solution to the distribution function provides knowledge of the movement of the guiding centers of the helical trajectories of the particles in the plasma as well as the Larmor radius gyration. However, it is impossible to solve for such a general solution in realistic magnetic geometry. In order to solve for the distribution function it is often necessary to divide the distribution function into a part that describes the movement of the guiding centers  $\tilde{f}_s$ , and a part that describes the Larmor gyration of the particles  $\tilde{f}_s$ . To better understand what this means, let us write the velocity of a particle following a helical trajectory around a magnetic field line as follows

$$\mathbf{v} = v_{\parallel} \hat{\mathbf{b}} + \mathbf{v}_{\perp} = v_{\parallel} \hat{\mathbf{b}} + v_{\perp} (\cos \varphi \hat{\mathbf{e}}_1 + \sin \varphi \hat{\mathbf{e}}_2), \quad (2.97)$$

with  $(v_{\perp}, \varphi, v_{\parallel})$  a set of cylindrical velocity-space coordinates with the  $z$ -direction along the magnetic field direction  $\hat{\mathbf{b}}$ . Here  $v_{\perp}$  and  $v_{\parallel}$  are respectively the magnitudes of the perpendicular and parallel components of the particle velocity with respect to the direction of the magnetic field line and  $\varphi$  is the gyrophase associated with the Larmor gyration. The unit vectors  $\hat{\mathbf{e}}_1$  and  $\hat{\mathbf{e}}_2$  are orthogonal to  $\hat{\mathbf{b}}$ , and orthogonal to themselves, which are dependent on the position of the particle. Thus, the distribution function would in general be written as  $f_s(\mathbf{x}, v_{\perp}, \varphi, v_{\parallel}, t)$ . If we are only interested in following the guiding centers of the particles, then we can take an average along the gyro motion of the particles, which means taking an average in the gyrophase coordinate. The gyroaverage for a quantity  $\mathcal{A}$  is thus defined as

$$\bar{\mathcal{A}}(v_{\perp}, \varphi, v_{\parallel}) = \frac{1}{2\pi} \int_0^{2\pi} \mathcal{A}(v_{\perp}, \varphi, v_{\parallel}) d\varphi. \quad (2.98)$$

We call  $\tilde{f}_s(\mathbf{x}, v_{\perp}, v_{\parallel}, t)$  the gyroaveraged distribution function. The fluctuating part of the distribution function is defined as  $\tilde{f}_s(\mathbf{x}, v_{\perp}, \varphi, v_{\parallel}, t) = f_s - \tilde{f}_s$  with the property  $\tilde{\tilde{f}}_s = 0$ . The position of the particles can also be separated into the guiding center position  $\bar{\mathbf{x}}$  and the Larmor radius position vector  $\boldsymbol{\rho}_L$ :

$$\mathbf{x} = \bar{\mathbf{x}} + \boldsymbol{\rho}_L = \bar{\mathbf{x}} + \frac{\hat{\mathbf{b}} \times \mathbf{v}_{\perp}}{\Omega_{C_s}}, \quad (2.99)$$

with  $\Omega_{C_s} = \frac{q_s B}{m_s c}$  the cyclotron frequency for a particle of species  $s$ . We notice that since  $\bar{\mathbf{v}}_{\perp} = 0$ , then  $\bar{\boldsymbol{\rho}}_L = 0$ . This means that gyroaveraged distribution function depends only on the position of the guiding centers such that  $\tilde{f}_s(\bar{\mathbf{x}}, v_{\perp}, v_{\parallel}, t)$ . Neoclassical transport (which is studied by the drift kinetic equation) is caused mostly by the movement of the guiding centers, so the distribution function is also expanded with respect to the usual neoclassical expansion parameter  $\delta$  (see equation 2.66). The distribution function expanded in  $\delta$  is written as

$$f = f_0 + f_1 + \dots \quad (2.100)$$

The temporal derivatives are considered to be second order in  $\delta$ , and at zeroth order, the electric field is electrostatic. The zeroth order distribution function can be seen to obey

$$v_{\parallel} \hat{b} \cdot \nabla_{\mathbf{x}} f_0 = C(f_0). \quad (2.101)$$

It can be shown that the zeroth order distribution is a Maxwellian due to collisions (9). Thus,  $f_0$  is given by

$$f_0 = f_M(\mathbf{x}, \varepsilon) = n_s(\mathbf{x}) \left( \frac{m_s}{2\pi T_s(\mathbf{x})} \right)^{\frac{3}{2}} e^{-\frac{m_s \varepsilon}{T_s(\mathbf{x})}}, \quad (2.102)$$

in which  $\varepsilon = \frac{v^2}{2} + \frac{q_s}{m_s} \Phi(\mathbf{x})$  is the energy (divided by the mass) of a particle of species  $s$  and  $\Phi$  is the electrostatic potential. The drift kinetic function can then be written as

$$v_{\parallel} \hat{b} \cdot \nabla_{\mathbf{x}} \bar{f}_1 + \mathbf{v}_d \cdot \nabla_{\mathbf{x}} f_0 - \frac{q_s E_{\parallel} v_{\parallel}}{T_s} f_0 = C(\bar{f}_1), \quad (2.103)$$

which is an equation for the first order gyroaveraged distribution function. This equation will be important for understanding the calculation of the geometrical factors of the background ion flows in section 2.8. The drift velocity is given to order  $\delta$  by

$$\mathbf{v}_d = -\overline{\frac{d}{dt} \boldsymbol{\rho}_L} = -v_{\parallel}^2 \frac{1}{\Omega_C} \boldsymbol{\kappa} \times \hat{b} + \frac{v_{\perp}^2}{2\Omega_C B} \hat{b} \times \nabla B + \frac{c}{B^2} \mathbf{E} \times \mathbf{B}. \quad (2.104)$$

The drift velocity is thus an gyro averaged measure of the deviation of the guiding center of a particle from its original trajectory along the magnetic field line due to the gyro movement of the particle around the magnetic field. This drift does not account for effects such as centrifugal or Coriolis forces as we are now interested in the treatment of the ions which are subsonic. Such drifts arise for the guiding center treatment of supersonic species like heavy impurities as we will see in section 2.12 with the Hamiltonian formalism.

## 2.8 Understanding flows associated with geometry

The background parallel ion flow and heat flux are exactly obtained from this drift kinetic equation for subsonic main ions. A detailed derivation was done in (33). Here, we will discuss the meaning of the different components of the main ion parallel flows at order  $\delta$  (see equation 2.84). The drift kinetic equation that is solved for resolution of the parallel ion flows and heat flux (33) is



$$v_{\parallel} \hat{b} \cdot \nabla_{\mathbf{x}} f_1 + v_{\mathbf{d}} \cdot \nabla_{\mathbf{x}} f_0 = C(f_1). \quad (2.105)$$

This equation is solved by dividing the gyroaveraged distribution function into a part that is even in  $v_{\parallel}$ , which is notated  $f_1^+$  and a part that is odd in  $v_{\parallel}$  which is  $f_1^-$ . Since we want to calculate the parallel flow of the ions we are interested in the odd part of the distribution function. The odd part of the distribution function can be shown to be given by

$$f_1^-(\psi, l, \varepsilon, \mu, \sigma) = \int \frac{dl'}{v_{\parallel}} v_{\mathbf{d}} \cdot \nabla_{\mathbf{x}} f_0 + K(\psi, \varepsilon, \mu, \sigma), \quad (2.106)$$

with  $l$  the arc length along the magnetic field line and  $\sigma$  indicates the sign of  $v_{\parallel}$  such that  $v_{\parallel} = \sigma |v_{\parallel}|$ . The function  $K(\psi, \varepsilon, \mu, \sigma)$  is a constant of integration which is independent of  $l$  and is in general obtained from the constraint

$$\left\langle \frac{B}{v_{\parallel}} C^-(f_1) \right\rangle = 0. \quad (2.107)$$

The parallel flow is then obtained by

$$U_{\parallel} = \int d^3 v v_{\parallel} f_1^-(\psi, l, \varepsilon, \mu, \sigma) = \int d^3 v \int dl' v_{\mathbf{d}} \cdot \nabla_{\mathbf{x}} f_0 + \int d^3 v v_{\parallel} K(\psi, \varepsilon, \mu, \sigma) = U_D + U_K. \quad (2.108)$$

It is clear that the flow has two contributions. The  $U_D$  contribution, which is simply due to the geometry of the magnetic field and is related to the drift of the main ions from their original orbits. This contribution is related to the function  $u$  obtainable in the fluid description from the continuity equation (see equation 2.85). The second contribution  $U_K$  is due to geometrical and collisional effects and it is related to the geometrical factor  $f_s$ , the parameter  $\eta$  which depends on the collisionality regime and the effective fraction of circulating particles  $f_c$ . Both these contributions are important for the bootstrap current. The first component of the flow  $U_D$  is associated to the Pfirsch-Schlüter flow. This flow is the parallel extension of the perpendicular diamagnetic effect, which has its contribution mostly from a diamagnetic effect generated mainly by the banana orbits which are the ones that deviate the most from their original trajectory along the magnetic field lines due to the magnetic drift velocity. The second contribution  $U_K$  is carried mostly by the circulating main ions which modify their flow velocity due to the collisional equilibrium set between them and the trapped banana ions (indeed  $U_K$  depends on  $f_c$ ). The collisional equilibrium is written mathematically by the constraint 2.107. The flux average of  $U_{\parallel}$  is usually called 'bootstrap' flow, due to its contribution to the bootstrap current.

## 2.9 Quasi-neutrality and ambipolarity

In order to have a full description of the background plasma we still need to determine the electric fields at orders  $\delta^0$  and  $\delta^{1/2}$  in the expansion 2.70. The zeroth order electric field  $E_0$  can be determined from the ambipolarity constraint. The flux averaged toroidal momentum equation 2.5 in the absence of time derivatives or inductive electric fields can be written for a species  $s$  as

$$q_s \langle \Gamma_{s\psi} \rangle = \langle B^\phi e_\phi \cdot \nabla \cdot \boldsymbol{\pi}_{s1} \rangle - \langle B^\phi e_\phi \cdot \mathbf{F}_{r_s} \rangle - \langle B^\phi e_\phi \cdot \mathbf{S}_{m_s} \rangle, \quad (2.109)$$

and is an equation for the flux averaged cross-field flux. Here,  $\Gamma_{s\psi} = \Gamma_s \cdot \nabla \psi = n_s \mathbf{U}_s \cdot \nabla \psi$ . Ambipolarity between ions and electrons implies

$$q_I \langle \Gamma_{I\psi} \rangle + q_e \langle \Gamma_{e\psi} \rangle = 0. \quad (2.110)$$

Thus, in the absence of strong sources of toroidal momentum the sum of equation 2.109 for ions and electrons at order  $\delta$  is equivalent to

$$\langle B^\phi e_\phi \cdot \nabla \cdot \boldsymbol{\pi}_{I1} \rangle - \langle B^\phi e_\phi \cdot \nabla \cdot \boldsymbol{\pi}_{e1} \rangle = 0. \quad (2.111)$$

The viscous tensor  $\boldsymbol{\pi}_{s1}$  is now associated with the flows at order  $\delta$  for species  $s$ . Thus, the tensor is not written easily in terms of the rate of strain tensor. Its form has to be calculated from the kinetic equation. However, we know that the non-ambipolar flux of species  $s$  in the regime  $1/\nu$  is driven by the toroidal viscosity  $\langle B^\phi e_\phi \cdot \nabla \cdot \boldsymbol{\pi}_{s1} \rangle$  (24), thus, the two are proportional. This also implies that the toroidal viscosity has to scale with  $\nu$  in the same way as the non-ambipolar fluxes, that is with  $1/\nu$ . The electron viscosity is thus, much smaller than the ion viscosity since both terms are proportional to the square root of the mass of the respective species (20). Equation 2.111, and the associated solution for the electric field corresponds therefore to an ion root due to the fact that the ambipolar electric field is set by the ion flux in the absence of strong sources of momentum. The ambipolar electric field is in this case negative. The considerations just described imply that the constraint 2.111 can be written as (see equation 2.86)

$$\langle B^\phi e_\phi \cdot \nabla \cdot \boldsymbol{\pi}_{I1} \rangle = q_I \langle \Gamma_{1/\nu} \rangle \propto \langle BU_{I\parallel} \rangle = 0 \quad (2.112)$$

and thus the zeroth order electric field is given by

$$\langle BU_{I\parallel} \rangle \approx 0 \Leftrightarrow E_0 = -\frac{\partial \Phi_0}{d\psi} \approx \frac{1}{q_I N_{I_0}} \frac{\partial P_{I_0}}{d\psi} - 1.17 \frac{1}{q_I} \frac{dT_I}{d\psi}, \quad (2.113)$$

in order to maintain ambipolarity. If a strong source of ECRH is present a strong electron flux will exist due to the interaction of such fast electrons and the 3D perturbed magnetic field, which can create a strong non-ambipolar electron flux. This situation often happens in stellarators, which can thus be the origin of a solution for ambipolarity with a positive electric field, which is usually called electron root. It is possible that in ASDEX-U tokamaks with 1/1 internal kinked plasmas, the process electron root generation could occur due to ECRH (53).

The electric field at order  $\delta^{1/2}$  can be determined by the quasi-neutrality constraint at order  $\delta^{1/2}$ , which can be written as

$$\tilde{n}_i(\psi, \theta, \phi) \approx \tilde{n}_e(\psi, \theta, \phi). \quad (2.114)$$

Using quasi-neutrality with the parallel momentum equations for ions and electrons at order  $\delta^{1/2}$ , we obtain the following equation involving the magnetic differential operator:

$$\mathbf{B} \cdot \nabla \Phi_{1/2}(\psi, \theta, \phi) = -\frac{m_I T_I}{q_I T_e + q_e T_I} \mathbf{B} \cdot [\mathbf{U}_{1/4} \cdot \nabla \mathbf{U}_{1/4}]. \quad (2.115)$$

Substituting 2.82 into 2.115, we obtain the well known result for tokamaks

$$\frac{e E_{1/2}}{T_e} = -\frac{e \Phi_{1/2}}{T_e} = -\frac{m_I T_e}{2(T_I + Z_I T_e)} \Omega^2 (R^2 - \langle R^2 \rangle), \quad (2.116)$$

where we have used  $\langle \Phi_{1/2} \rangle = 0$  to set the constant of integration. The electric field at this order is important as its effect on the heavy impurity density asymmetries is of order  $\delta^0$  due to the large mass of such impurities. This field will thus have an impact in obtaining the heavy impurity flow at order  $\delta^1$  (see next section 2.10), and will appear as a guiding center drift at order in the guiding center equations used to follow heavy impurities (see section 2.12) in the VENUS-LEVIS code (see section 3.2.1). We remark here that the presence of impurities could in principle change the quasi-neutrality constraint and therefore  $E_{1/2}$ . However, in the trace limit, considered in this thesis, such effect should be small.

## 2.10 Heavy impurity flow

Heavy impurities are in the regime of high collisionality both in the core and in the edge of tokamaks. We may therefore use only a fluid description for heavy species. Heavy impurities flow with the common flow  $\mathbf{U}_{1/4}$ . However, since  $v_{thW}^2 \sim v_{thI}^2 / Z_W$ , the impurities will flow supersonically with this common velocity, i.e.  $M_W^2 \sim 1$  or larger. Under this condition, the first order perpendicular flow of the impurities is obtained from taking the  $\mathbf{B} \times \nabla \psi$  component of the momentum equation 2.5 for the impurities at order  $\delta^{1/4}$ . It is given by

$$\mathbf{U}_{W_{1/4\perp}} = \frac{\mathbf{B} \times \nabla \Phi_{-3/4}}{B^2} = \mathbf{U}_{1/4\perp}, \quad (2.117)$$

which corresponds to the perpendicular common flow of all species due to the NBI induced rotation (as is the case for the lowest order flow of the bulk ions). At order,  $\delta^1$  we can write

$$\mathbf{U}_{W_{1\perp}} = \frac{\mathbf{B} \times \nabla \Phi_0}{B^2}, \quad (2.118)$$

which is the  $\mathbf{E} \times \mathbf{B}$  velocity due to the ambipolar electric field (for e.g. NTV, see equation 2.113). At order  $\delta^{3/2}$ , we have

$$\mathbf{U}_{W_{3/2\perp}} = \frac{\mathbf{B} \times \nabla \Phi_{1/2}}{B^2} + \frac{\mathbf{B} \times \nabla P_{W_0}(\psi, \theta, \phi)}{q_W n_W B^2} - \frac{m_W}{q_W} \frac{\mathbf{B} \times [\mathbf{U}_{W_{1/4}} \cdot \nabla \mathbf{U}_{W_{1/4}}]}{B^2}. \quad (2.119)$$

This flow is important to be retained in the case of impurities because they are often supersonic and we want to retain the effect of the radial centrifugal force. We need to retain the impurity density gradient term for providing steady state analytical solutions as well. We may obtain the same constraint as the one obtained in 2.80 at order  $\delta^{1/4} \lambda_W / L$ . At order  $\delta^{5/4}$  (the lowest order), we have the continuity equation 2.2 for the impurities

$$\nabla \cdot (n_W \mathbf{U}_{W_{1/4}}) = 0, \quad (2.120)$$

which is different from the lowest order continuity equation for the ions, since the impurity flow has not at this point been shown to be incompressible. However, using the lowest order energy flux equation 2.15 for impurities, we have

$$\frac{q_W}{m_W} (\mathbf{q}_{W_{1/4}} \times \mathbf{B}) = 0, \quad (2.121)$$

and the energy equation 2.12 for the impurities at lowest order can be written as

$$\nabla \cdot \mathbf{q}_{W_{1/4}} = -\nabla \cdot \left( \frac{3}{2} P_W \mathbf{U}_{W_{1/4}} \right) - P_W \nabla \cdot \mathbf{U}_{W_{1/4}}, \quad (2.122)$$

and from the lowest order entropy equation 2.20, we obtain

$$\mathbf{B} \cdot \nabla T_W = 0. \quad (2.123)$$

This implies that the temperature of impurities is at lowest order a flux function, which finally yields that the flow  $\mathbf{U}_{W_{1/4}}$  is incompressible:

$$\nabla \cdot \mathbf{U}_{W_{1/4}} = 0. \quad (2.124)$$

This simply confirms that  $\mathbf{U}_{W_{1/4}}$  is the same as that for bulk ions, that it obeys to the same constraints, and it is indeed a common flow, as clear from 2.75. At higher order the tungsten temperature is not necessarily a flux function and the impurity flow at order  $\delta$  obeys the continuity equation at the next order

$$\nabla \cdot (n_W \mathbf{U}_{W_1}) = 0. \quad (2.125)$$

This equation may then be solved to find the first order parallel impurity flow if we know the form of the impurity density. The part of the impurity density varying in the direction tangential to the magnetic field may be obtained from the parallel component of the impurity momentum equation at order  $\delta^{3/2}$ . If the ion density and temperature gradients are not very large, collisional effects between impurities and ions are not enough to generate poloidal impurity density asymmetries. In such cases we have  $\Delta = Z_W^2 \delta \hat{v}_{II} \ll 1$  (47) i.e. we may neglect impurity density asymmetries due to collisions, by neglecting the effect of the friction force on the parallel component of the impurity momentum equation. Solving this equation, we obtain the impurity density

$$n_W(\psi, \theta) = N_W(\psi) \exp[M_W^2/2(\psi, \theta) - q_W \Phi_{1/2}/T_W(\psi)] = N_W(\psi) \exp[M^2(\psi, \theta)]. \quad (2.126)$$

However, we point out that the ordering considered, i.e.  $1/Z_W \sim \delta^{1/2}$  used in this thesis allows for the treatment of poloidal impurity density asymmetries which are self-generated by impurity-ion collisions (since we allow for  $\Delta = Z_W^2 \delta \hat{v}_{II} \sim 1$  as in (47)). Such effect may be important in the treatment of modes like edge harmonic oscillations.

Using this result in 2.125, we obtain the parallel impurity flow given by

$$\mathbf{U}_{W_{1\parallel}} = w \left[ \frac{d\Phi_0}{d\psi} + \frac{T_I}{q_W N_W} \frac{dN_W}{d\psi} + \frac{m_W \Omega R^2}{q_W} \frac{d\Omega}{d\psi} \right] \mathbf{B} + \frac{\mathcal{K}_W \mathbf{B}}{n_W}. \quad (2.127)$$

where the radial friction and flux were neglected. We also neglected the terms proportional to the impurity temperature gradient. The constant of integration  $\mathcal{K}_W$  in equation 2.127 is obtained from conservation of collisional momentum between ions and impurities, and the function  $w$  obeys the magnetic differential equation written as

$$\mathbf{B} \cdot \nabla (n_W w) = -\mathbf{B} \times \nabla \psi \cdot \nabla \left( \frac{n_W}{B^2} \right). \quad (2.128)$$

In the limit of  $M_W^2 \ll 1$ , there are no impurity asymmetries and the function  $w$  is identical to the function  $u$  for the ion flow. In axisymmetry, the functions  $u$ ,  $w$  and  $f_s$  may be obtained analytically (see later, section 2.11). However, in general 3D geometry, a numerical solution is necessary to describe these functions (see section 3.1.5).

## 2.11 Heavy impurity neoclassical flux

The impurity neoclassical flux is related to the parallel friction between impurities and ions (52) in the following way:

$$q_W \langle \Gamma_W \cdot \nabla \psi \rangle^{Neo} = \langle B w R_{W\parallel} \rangle. \quad (2.129)$$

The friction force may be obtained for a Coulomb operator in the form of the sum of a Lorentz operator and a momentum restitution term and is composed of both a drag force and a thermal force (49),(9):

$$R_{W\parallel} = -m_I N_I v_{IW} \left( \mathbf{U}_{W\parallel} - \mathbf{U}_{I\parallel} - \frac{3}{5} \frac{q_I}{P_I} \right). \quad (2.130)$$

The final form of the impurity-ion friction is obtained by substituting the values of the flows and the first order heat flux,

$$\begin{aligned} \frac{R_{W\parallel}}{v_{IW} N_I m_I} = & - \left[ w - \frac{\langle w B^2 \rangle}{n_W \langle \frac{B^2}{n_W} \rangle} \right] \left[ \frac{\partial \Phi_0}{\partial \psi} + \frac{T_I}{q_W N_W} \frac{\partial N_W}{\partial \psi} \right] B - \left[ \frac{w R^2}{\langle R^2 \rangle} - \frac{\langle w R^2 B^2 \rangle}{n_W \langle R^2 \rangle \langle \frac{B^2}{n_W} \rangle} \right] \frac{m_W \Omega \langle R^2 \rangle}{q_W} \frac{\partial \Omega}{\partial \psi} B \\ & + \left[ u - \frac{\langle u B^2 \rangle}{\langle B^2 \rangle} + \left( \frac{1}{\langle B^2 \rangle} - \frac{1}{n_W \langle \frac{B^2}{n_W} \rangle} \right) (f_s + \langle u B^2 \rangle) \left( \frac{f_c}{f_t} + 1 \right) \right] \left[ \frac{\partial \Phi_0}{\partial \psi} + \frac{T_I}{q_I N_{I_0}} \frac{\partial N_{I_0}}{\partial \psi} \right] B \\ & - \left[ \frac{3}{2} u - \frac{3}{2} \frac{\langle u B^2 \rangle}{\langle B^2 \rangle} + \left( \frac{1}{\langle B^2 \rangle} - \frac{1}{n_W \langle \frac{B^2}{n_W} \rangle} \right) (f_s + \langle u B^2 \rangle) \left( 1.17 \frac{f_c}{f_t} + \frac{3}{2} \right) \right] \frac{1}{q_I} \frac{\partial T_I}{\partial \psi} B, \end{aligned} \quad (2.131)$$

where momentum conservation was used by applying the constraint

$$\left\langle R_{W\parallel} \frac{B}{n_W} \right\rangle = 0. \quad (2.132)$$

Thus, the impurity flux is written as

$$\frac{\langle \Gamma_W \cdot \nabla \psi \rangle^{Neo}}{\langle n_W \rangle \langle B^2 \rangle} = D_\Phi^{Neo} \frac{q_I}{T_I} \frac{\partial \Phi_0}{\partial \psi} - D_{N_W}^{Neo} \frac{q_I}{q_W} \frac{\partial \ln N_W}{\partial \psi} - D_\Omega^{Neo} \frac{q_I m_W \Omega R^2}{q_W T_I} \frac{\partial \Omega}{\partial \psi} - D_{N_I}^{Neo} \frac{\partial \ln N_{I_0}}{\partial \psi} - D_{T_I}^{Neo} \frac{\partial \ln T_I}{\partial \psi}, \quad (2.133)$$

where the diffusion coefficients are defined as (52)

$$D_\Phi^{Neo}(\psi) = D_{class} \left[ \langle n_W w (u - w) B^2 \rangle + \frac{\langle w B^2 \rangle^2}{\langle \frac{B^2}{n_W} \rangle} - \frac{\langle u B^2 \rangle \langle n_W w B^2 \rangle}{\langle B^2 \rangle} + \left( \frac{\langle n_W w B^2 \rangle}{\langle B^2 \rangle} - \langle w B^2 \rangle \left\langle \frac{B^2}{n_W} \right\rangle^{-1} \right) (f_s + \langle u B^2 \rangle) \left( \frac{f_c}{f_t} + 1 \right) \right], \quad (2.134)$$

$$D_{N_W}^{Neo}(\psi) = D_{class} \left[ \langle n_W w^2 B^2 \rangle - \frac{\langle w B^2 \rangle^2}{\langle \frac{B^2}{n_W} \rangle} \right], \quad (2.135)$$

$$D_\Omega^{Neo}(\psi) = D_{class} \left[ \frac{\langle n_W w^2 R^2 B^2 \rangle}{\langle R^2 \rangle} - \frac{\langle w B^2 \rangle \langle w R^2 B^2 \rangle}{\langle R^2 \rangle \langle \frac{B^2}{n_W} \rangle} \right], \quad (2.136)$$

$$D_{N_I}^{Neo}(\psi) = -D_{class} \left[ \langle n_W w u B^2 \rangle - \frac{\langle u B^2 \rangle \langle n_W w B^2 \rangle}{\langle B^2 \rangle} + \left( \frac{\langle n_W w B^2 \rangle}{\langle B^2 \rangle} - \langle w B^2 \rangle \left\langle \frac{B^2}{n_W} \right\rangle^{-1} \right) (f_s + \langle u B^2 \rangle) \left( \frac{f_c}{f_t} + 1 \right) \right], \quad (2.137)$$

and

$$D_{T_I}^{Neo}(\psi) = \frac{1}{2} D_{class} \left[ \langle n_W w u B^2 \rangle - \frac{\langle u B^2 \rangle \langle n_W w B^2 \rangle}{\langle B^2 \rangle} + \left( \frac{\langle n_W w B^2 \rangle}{\langle B^2 \rangle} - \langle w B^2 \rangle \left\langle \frac{B^2}{n_W} \right\rangle^{-1} \right) (f_s + \langle u B^2 \rangle) \left( \frac{f_c}{f_t} (2\eta - 3) + \frac{1}{f_t} \right) \right]. \quad (2.138)$$

Here, the classical diffusion coefficient is written as

$$D_{class} = \frac{v_{IW} N_{I_0} m_I T_I}{\langle n_W \rangle \langle B^2 \rangle q_I q_W n_W} \quad (2.139)$$

and we used the fact that  $\frac{v_{IW}}{n_W}$  is a flux function. In the saturated state, the flux averaged flux of impurities  $\langle \Gamma_W \cdot \nabla \psi \rangle^{Neo}$  vanishes by definition. We may obtain an approximated expression for the time invariant impurity density radial profile from equation 2.133. The impurity flux 2.133 is similar to the expressions of (51) and (52). The usual transport drives due to the main

ion density and temperature gradients are observed, as well as the drive due to the ambipolar electric field. However, an extra drive due to the strong radial centrifugal force felt by the heavy impurities is present in this case, contrary to what happens in stellarators [(51), (52)] in which strong rotation is not possible.

It is worth exploring the limits of  $M_W^2 \ll 1$  in a 3D plasma, and separately  $M_W^2 \sim 1$  in the axisymmetric limit, since these simple cases can be understood more easily and analytic solutions are already known. We will then be able to see how the transport coefficients 2.134-2.138 are modified by strong flows and 3D. In the limit of no sonic flows, we have that there are no impurity asymmetries which means  $n_W = N_w(\psi)$  and  $w = u$ . We therefore find that the transport coefficients under the limit of sub-sonic flows and axisymmetry are

$$D_\Phi^{Neo}(\psi) = 0, \quad (2.140)$$

$$D_{N_W}^{Neo}(\psi) = D_\Omega^{Neo}(\psi) = D_{class} \left[ \langle u^2 B^2 \rangle - \frac{\langle u B^2 \rangle^2}{\langle B^2 \rangle} \right], \quad (2.141)$$

$$D_\Omega^{Neo}(\psi) = D_{class} \left[ \frac{\langle u^2 R^2 B^2 \rangle}{\langle R^2 \rangle} - \frac{\langle u B^2 \rangle \langle u R^2 B^2 \rangle}{\langle R^2 \rangle \langle B^2 \rangle} \right], \quad (2.142)$$

$$D_{N_I}^{Neo}(\psi) = -D_{N_W}^{Neo}(\psi) \quad (2.143)$$

and

$$D_{T_I}^{Neo}(\psi) = \frac{1}{2} D_{N_W}^{Neo}(\psi). \quad (2.144)$$

In this limit, we see that there is no transport due to the ambipolar electric field since  $D_\Phi^{Neo}(\psi) = 0$ . Even though  $D_\Omega^{Neo}$  does not vanish, there is no important transport driven by rotation since all of the transport coefficients are of the same magnitude in this limit, and thus the driving term due to rotation in 2.133 is now small when compared with the other driving terms since  $M_W^2 \ll 1$ . We may also note that the factor  $f_s + \langle u B^2 \rangle$  associated with the mean part of the parallel flow of the bulk ions vanishes in the expressions 2.140-2.144. This means that the mean parallel flow does not influence impurity transport in this limit. We remark here that this limit is similar to stellarator applications for cases where there is no source of impurity density asymmetries from e.g. ICRH, ECRH or strong trapping of the bulk ions. However, sonic flows, which are prohibited in stellarators, provide also a driving term of transport in the form of the radial centrifugal force (third term in 2.133), which can be important in tokamaks in the presence of 3D long lived modes.



In the limit of axisymmetry, but large flows, we find the following analytical solutions for the functions  $u$ ,  $w$  and  $f_s$ :

$$uB^2 = -\frac{B_\phi(\psi)}{\iota(\psi)} \left(1 - \frac{B^2}{B_{max}(\psi)^2}\right), \quad (2.145)$$

$$wB^2 = -\frac{B_\phi(\psi)}{\iota(\psi)} \left(1 - \frac{B^2 n_{w_{max}}(\psi)}{n_w B_{max}(\psi)^2}\right), \quad (2.146)$$

$$f_s = \frac{B_\phi(\psi)}{\iota(\psi)} \left(f_c - \frac{\langle B^2 \rangle}{B_{max}(\psi)^2}\right). \quad (2.147)$$

Using 2.145 and 2.146 in 2.134-2.138 we obtain the diffusion coefficients for strong flows in axisymmetry

$$D_\Phi^{Neo}(\psi) = 0 \quad (2.148)$$

$$D_{N_W}^{Neo}(\psi) = D_{class} \frac{B_\phi^2}{\iota^2} \left[ \left\langle \frac{n_W}{B^2} \right\rangle - \left\langle \frac{B^2}{n_W} \right\rangle^{-1} \right], \quad (2.149)$$

$$\begin{aligned} D_\Omega^{Neo}(\psi) = D_{class} \frac{B_\phi^2}{\iota^2} \langle R^2 \rangle^{-1} & \left[ \left\langle \frac{R^2 n_W}{B^2} \right\rangle - \left\langle \frac{B^2}{n_W} \right\rangle^{-1} \langle R^2 \rangle \right. \\ & \left. + \frac{n_{W_{max}}}{B_{max}^2} \left( \left\langle \frac{R^2 n_W}{B^2} \right\rangle \left\langle \frac{B^2}{n_W} \right\rangle^{-1} - \langle R^2 \rangle \right) \right], \end{aligned} \quad (2.150)$$

$$D_{N_I}^{Neo}(\psi) = -D_{class} \frac{B_\phi^2}{\iota^2} \left[ \left\langle \frac{n_W}{B^2} \right\rangle - \left\langle \frac{B^2}{n_W} \right\rangle^{-1} \right], \quad (2.151)$$

and

$$\begin{aligned} D_{T_I}^{Neo}(\psi) = \frac{1}{2} D_{class} \frac{B_\phi^2}{\iota^2} & \left[ \left\langle \frac{n_W}{B^2} \right\rangle - \left\langle \frac{B^2}{n_W} \right\rangle^{-1} \right. \\ & \left. + \left( \frac{\langle n_W \rangle}{\langle B^2 \rangle} - \left\langle \frac{B^2}{n_W} \right\rangle^{-1} \right) f_c (2\eta - 3) \right]. \end{aligned} \quad (2.152)$$

Again  $D_\Phi^{Neo}(\psi) = 0$  (equation 2.148). Hence, the analysis of the 2D limit with strong flows and 3D with no flows, leads to the conclusion that the radial ambipolar electric field (e.g due to NTV) can only drive impurity transport when there is **both**  $M_W^2 \sim 1$  and 3D effects. We may

also see from 2.148-2.152 that the classic diffusion coefficient may be enhanced by a factor  $\frac{B_\phi^2}{\langle B^2 \rangle r^2}$  in the limit of  $M_W^2 \ll 1$ . If  $M_W^2 \sim 1$ , the enhancement of the diffusion coefficient may be of order  $n_W = \exp[M^2(\psi, \theta)]$ , which can be quite large. We may also observe that the diffusion coefficients 2.149, 2.151 and 2.152 agree with the results obtained in (47) and (48), but an extra diffusion coefficient 2.11 associated with the drive of the strong radial centrifugal force felt by the impurities appears here, which was not considered in (47) and (48).

## 2.12 The guiding-center equations of motion in the presence of strong flows

In order to model numerically impurity physics associated with neoclassical transport it is convenient to use the guiding-center description. From the orderings presented in this chapter, we know that we have to consider the effects of supersonic flows. The hamiltonian formalism (69) allows for such strong flows. The guiding-center Hamiltonian of a heavy impurity particle in the presence of a strong flow  $\mathbf{U}_{1/4}$  and a velocity  $\mathbf{U}_{W_1}$  (which we choose to keep, due its importance for collisions with main ions) is given by

$$H = \frac{m_W(\mathbf{w}_\parallel + \mathbf{U}_{1/4} + \mathbf{U}_{W_1})^2}{2} + q_W(\Phi_{-3/4} + \Phi_0 + \Phi_{1/2}) + \mu B. \quad (2.153)$$

We remind here that this ordering agrees with (69) since the Larmor radius for the impurities is smaller by  $\delta^{1/4}$  than the Larmor radius of the ions. The Hamiltonian equations are from the formalism in (69) are written as

$$\dot{\mathbf{x}} = \frac{\mathbf{B}^*}{m_W \mathbf{B} \cdot \mathbf{B}^*} \frac{\partial H}{\partial \mathbf{w}_\parallel} + \frac{\mathbf{B} \times \nabla H}{q_W \mathbf{B} \cdot \mathbf{B}^*} \quad (2.154)$$

and

$$\dot{w}_\parallel = \frac{\mathbf{B} \mathbf{B}^* \cdot \nabla H}{m_W \mathbf{B} \cdot \mathbf{B}^*}, \quad (2.155)$$

with

$$\mathbf{B}^* = \mathbf{B} + \frac{m_W}{q_W} \nabla \times [\mathbf{U}_{1/4} + \mathbf{U}_{W_1} + \mathbf{w}_\parallel]. \quad (2.156)$$

Inserting the Hamiltonian 2.156 in equation 2.154 and 2.155 yields, after some algebra, an equation for the guiding-center position  $\bar{\mathbf{x}}$  in the lab frame and an equation for the parallel velocity in the rotating frame  $w_\parallel$

$$\dot{\mathbf{x}} = \mathbf{U}_{1/4} + \mathbf{U}_{W_1} + \mathbf{w}_\parallel + \frac{\mathbf{F}_d \times \mathbf{B}}{q_W \mathbf{B} \cdot \mathbf{B}^*}, \quad (2.157)$$

$$\dot{w}_\parallel = -\frac{\mathbf{F}_d \cdot \mathbf{B}^* \mathbf{B}}{m_W \mathbf{B} \cdot \mathbf{B}^*}, \quad (2.158)$$

in which  $\mathbf{F}_d$  can be written as

$$\mathbf{F}_d = -\mu \nabla B - m_W w_{\parallel}^2 \hat{b} \cdot \nabla \hat{b} - m_Z \frac{\partial w_{\parallel}}{\partial t} - m_W \mathbf{w}_{\parallel} \cdot \nabla \mathbf{U}^* - m_W \mathbf{U}^* \cdot \nabla \mathbf{w}_{\parallel} - m_W \mathbf{U}^* \cdot \nabla \mathbf{U}^* - q_W \nabla \Phi_{1/2} \quad (2.159)$$

where  $\mathbf{U}^* = \mathbf{U}_{1/4} + \mathbf{U}_{W_1}$ . The drifts in equation 2.159 are, by order of appearance, due to the magnetic mirror force, the curvature force, the Coriolis force, the parallel acceleration force, the centrifugal force, and the electric force due to  $\mathbf{E}_{1/2}$ . We can however, neglect the Coriolis and centrifugal force due to the impurity flow  $\mathbf{U}_{W_1}$  because it is much smaller than  $\mathbf{U}_{1/4}$ . Therefore, the force exerted in the guiding centers becomes

$$\mathbf{F}_d = -\mu \nabla B - m_W \mathbf{w}_{\parallel} \cdot \nabla \mathbf{w}_{\parallel} - m_Z \frac{\partial w_{\parallel}}{\partial t} - m_W \mathbf{w}_{\parallel} \cdot \nabla \mathbf{U}_{1/4} - m_W \mathbf{U}_{1/4} \cdot \nabla \mathbf{w}_{\parallel} - m_W \mathbf{U}_{1/4} \cdot \nabla \mathbf{U}_{1/4} - q_W \nabla \Phi_{1/2}. \quad (2.160)$$

Here, we see that indirect dependence on the  $\mathbf{E}_{-3/4}$  through the centrifugal and Coriolis effects due to  $\mathbf{U}_{1/4}$ . The  $q_W \mathbf{E}_{1/2}$  appears as the electric force felt by the impurities in the rotating frame. The ambipolar electric field  $\mathbf{E}_0$  is not obvious however. This is because its effect comes mainly in the collisions with the background ions. The Hamiltonian formulation does not provide such collisional forces. The numerical implementation of the guiding-center equations 2.157 and 2.158 are explained in the next chapter. They are solved using the VMEC and VENUS-LEVIS code packages. The VMEC code provides the suitable magnetic configuration given by  $\mathbf{B}$  in these equations as well as a way to calculate the background ion  $\mathbf{U}_{I_1}$  and impurity  $\mathbf{U}_{W_1}$  flows. Then, VENUS-LEVIS follows the tungsten particles by solving the equations just described with a suitable collision operator that has a proper friction force and thermal force. Such an operator can be obtained from a perturbed Maxwellian for the main ions which can be written as

$$f_I = f_{I_0}(\psi, \theta, v) \left[ 1 - \left( \frac{\mathbf{U}_{back}}{v_{th_I}^2} - \frac{\mathbf{q}_I}{P_I v_{th_I}^2} \left( 1 - \frac{w^2}{5v_{th_I}^2} \right) \right) \cdot \mathbf{v} \right], \quad (2.161)$$

in which  $\mathbf{U}_{back} = \mathbf{U}_{I_1} - \mathbf{U}_{W_1}$  is the main ion velocity in the frame rotating with  $\mathbf{U}^* = \mathbf{U}_{1/4} + \mathbf{U}_{W_1}$ . Thus, the background flows  $\mathbf{U}_{I_1}$ ,  $\mathbf{U}_{W_1}$  (which incorporate the effect of the ambipolar electric field  $\mathbf{E}_0$ ) and the ion heat flux  $\mathbf{q}_{I_1}$  obtained in this chapter are of great importance to properly described the impurity physics.

## 2.13 Conclusion

By realizing that the background ions and the heavy impurities obey different orderings this chapter develops a systematic set of equations for the study of heavy impurity transport in the presence of 3D MHD perturbations and strong toroidal rotation. The model extends well known stellarator theory for heavy impurity transport, by considering the effect of strong rotation (which is not present in stellarator physics). This effect of rotation is important in tokamaks because, strong toroidal rotation (for the heavy impurities) is observed empirically, even when a long living mode, like for example, the 1/1 internal kink mode, is present, as we will see in chapters 3 and 4. The background ion flow 2.86 and heat flux 2.95, as well as

the impurity flow 2.127 are developed in detail in this chapter. These are important for the numerical modelling of such problems, as they are crucial for the new implementation of the collision operator in VENUS-LEVIS (see section 3.2.2) which complements the guiding center description presented in section 2.12. We also obtain an analytical expression for the heavy impurity flux which captures both the 3D and strong rotation effects. This expression can be used to gain insight on the behaviour of heavy impurity transport in tokamak plasmas with 3D MHD perturbations and strong toroidal rotation.

### 3 Numerical tools for the study of heavy impurity transport in the presence of 3D MHD ideal perturbations

In this chapter, we present the numerical implementation of the theoretical framework described in the previous chapter using the VMEC and VENUS-LEVIS code. The main workflow of the overall code package can be seen in figure 3.1. We start the chapter by explaining how the VMEC code solves the MHD force balance equation 2.36 using a variational approach to minimise the MHD energy. We then explain how we use VMEC to obtain the magnetic configurations of interest, particularly tokamak plasmas with a 1/1 internal kink mode. It follows the explanation of the new auxiliary codes developed in this thesis to obtain the geometrical factors associated with the background ion flows. First, we transform the magnetic geometry obtained from VMEC to straight field line coordinates (Boozer or Hamada). Then, the magnetic configuration in one of these set of coordinates can be used to solve the necessary magnetic differential equations for a solution of the geometrical factors. The 3D magnetic configuration and associated background ion flow and heat flux can be used as an input for the VENUS-LEVIS code. VENUS-LEVIS can then follow the minority species, such as heavy impurities, in the background just described. The VENUS-LEVIS implementation of the guiding center formalism shown in section 2.12 is described. Finally, we explain the new collision operator implemented in VENUS-LEVIS to capture both friction and thermal forces acting on heavy impurities.

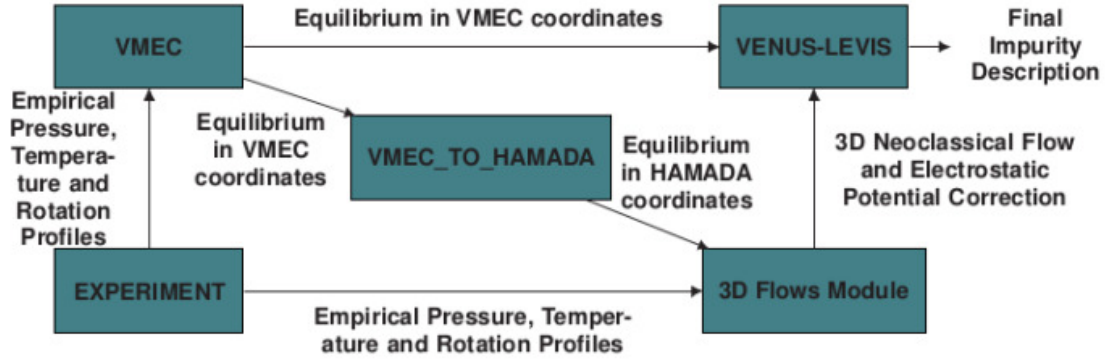


Figure 3.1 – Schematic of the overall code package used for obtaining numerical results in this work. The auxiliary codes to convert to Boozer or Hamada coordinates and to calculate the 3D ion flows and heat flux were developed in this thesis. The guiding center equations in VENUS-LEVIS were adapted and a new collision operator was implemented to properly model heavy impurity transport in the presence of 3D MHD ideal perturbations and strong flows.

### 3.1 The VMEC code

To obtain the magnetic equilibrium configurations obeying the MHD force balance equation 2.36, we make use of VMEC (57), (58). It is worth noting here that according to the orderings described in section 2.5, the background ions are subsonic and thus we treat the MHD force balance equation in the absence of strong flows. VMEC is an invaluable tool for these type of problems as it is an ideal MHD equilibrium code that can find solutions of the MHD force balance equation by minimising the MHD energy through a variational method. The possibility of giving as input the current profiles of the prescribed external coils allows it to solve for the MHD force balance without a fixed plasma boundary, which is of great importance to study both stellarator and 3D tokamak plasmas (with 3D MHD ideal saturated perturbations). A last remark is made here about the existence of nested closed flux surfaces in 3D magnetic equilibria. It is not possible to show their existence in a rigorous way for general 3D magnetic configurations. However, it was shown in (70) that 3D force balance solutions with nested flux surfaces are possible under certain constraints. We assume that this is the case for the experimental cases we want to treat.

#### 3.1.1 VMEC coordinates

VMC provides a description of a magnetic equilibrium configuration solution as an output. This output is thus comprised of the major radius  $R$  measuring the distance from the center of the tokamak, the vertical cylindrical coordinate  $Z$  measuring the distance relative to the plasma midplane ( $\theta = 0$ ), and the magnetic field magnitude  $B$ . These quantities are described in a set of flux coordinates  $(s_V, \theta_V, \phi_V)$  in which the poloidal angle is chosen in such a way as to allow for a good convergence of the solution (57), as we will see in next section. This set of

coordinates is called VMEC coordinates. The flux label coordinate  $s_V$  is given by

$$s_V = \frac{\Psi_T}{\Psi_{T_{edge}}}, \quad (3.1)$$

which is thus the toroidal flux normalized to its value  $\Psi_{T_{edge}}$  at the last closed flux surface (boundary of the plasma). The toroidal VMEC angle is chosen to be the toroidal cylindrical geometrical angle in the counter-clockwise direction (left-handed system), and so we have

$$\phi_V = -\phi_{Geo}, \quad (3.2)$$

as per the definitions in section 2.4 and appendix A. Thus, the contravariant magnetic field, the contravariant density current, and the covariant magnetic fields are given in VMEC coordinates as

$$\mathbf{B} = \left( \frac{d\Psi_T}{ds_V} + \frac{\partial \tilde{v}_V}{\partial \theta_V} \right) \nabla s_V \times \nabla \theta_V + \left( -\frac{d\Psi_P}{ds_V} + \frac{\partial \tilde{v}_V}{\partial \phi_V} \right) \nabla s_V \times \nabla \phi_V, \quad (3.3)$$

$$\mathbf{J} = \left( \frac{dI_T}{ds_V} - \frac{\partial \tilde{w}_V}{\partial \theta_V} \right) \nabla s_V \times \nabla \theta_V + \left( \frac{d\Psi_P}{ds_V} - \frac{\partial \tilde{w}_V}{\partial \phi_V} \right) \nabla s_V \times \nabla \phi_V, \quad (3.4)$$

$$\mathbf{B} = \frac{\partial \tilde{u}_V}{\partial s_V} \nabla s_V + \left( I_T + \frac{\partial \tilde{u}_V}{\partial \theta_V} \right) \nabla \theta_V + \left( I_P + \frac{\partial \tilde{u}_V}{\partial \phi_V} \right) \nabla \phi_V, \quad (3.5)$$

in which  $\tilde{v}_V$ ,  $\tilde{w}_V$ ,  $\tilde{u}_V$  are the periodic potential functions defined in appendix A for VMEC coordinates. In addition to  $R$ ,  $Z$  and  $B$ , the full output of VMEC provides the components of 3.3, 3.5 and 3.4

$$B^{\theta_V} = \frac{\frac{d\Psi_T}{ds_V} + \frac{\partial \tilde{v}_V}{\partial \theta_V}}{\sqrt{g_V}}, \quad (3.6)$$

$$B^{\phi_V} = \frac{-\frac{d\Psi_P}{ds_V} + \frac{\partial \tilde{v}_V}{\partial \phi_V}}{\sqrt{g_V}}, \quad (3.7)$$

$$J^{\theta_V} = \frac{\frac{dI_T}{ds_V} - \frac{\partial \tilde{w}_V}{\partial \theta_V}}{\sqrt{g_V}}, \quad (3.8)$$

$$J^{\phi_V} = \frac{\frac{dI_P}{ds_V} - \frac{\partial \tilde{w}_V}{\partial \phi_V}}{\sqrt{g_V}}, \quad (3.9)$$

$$B_s = \frac{\partial \tilde{u}_V}{\partial s_V}, \quad (3.10)$$

$$B_{\theta_V} = I_P + \frac{\partial \tilde{u}_V}{\partial \theta_V}, \quad (3.11)$$

$$B_{\phi_V} = I_T + \frac{\partial \tilde{u}_V}{\partial \phi_V}, \quad (3.12)$$

as well as the jacobian  $\sqrt{g}_V(s_V, \theta_V, \phi_V) = (\nabla s_V \cdot \nabla \theta_V \times \nabla \phi_V)^{-1}$  of VMEC coordinates. Since these scalars are periodic functions of  $(\theta_V, \phi_V)$  they can be expanded in a Fourier series. This is done in VMEC for a periodic function  $X$  in such a way that

$$X(s_V, \theta_V, \phi_V) = \sum_{m,n} [X_{mn}^c(s_V) \cos(m\theta_V - n\phi_V) + X_{mn}^s(s_V) \sin(m\theta_V - n\phi_V)], \quad (3.13)$$

in which  $m$  and  $n$  are respectively the poloidal and toroidal mode numbers associated with VMEC coordinates. The superscripts  $c$  and  $s$  indicate respectively the cosine and sine Fourier components of  $X$ . The choice of  $\theta_V$  is thus more specifically associated with the convergence of such a Fourier series expansion of the VMEC solution (57). If up-down symmetry (which is a special case of stellarator symmetry) is assumed, then  $R$ ,  $B$ ,  $\sqrt{g}_V$ ,  $B^{\theta_V}$ ,  $B^{\phi_V}$ ,  $B_{\theta_V}$ ,  $B_{\phi_V}$  are written simply as a cosine series, while  $Z$  and  $B_s$  can be written as a sine series only. All these quantities and relations will be useful for obtaining the geometrical factors for the background ions as well as for following the tungsten particles with VENUS-LEVIS.

VMEC solves the MHD force equation via a user defined flux averaged equilibrium pressure profile  $P(s_V)$  and a user defined measure of the poloidal magnetic field. This measure can be provided by giving the total toroidal current profile  $I_t(s_V)$  or the rotational transform  $\iota(s_V)$ , which is equivalent to the safety factor profile  $q(s_V) = 1/\iota(s_V)$ . Note that we neglect centrifugal effects in the magnetic equilibria since the ions are strongly subsonic. Hence, the rotation profile is not an input to the VMEC code. After processing the equilibrium, we consider the effects of such equilibrium and the rotation on impurities, as described in chapter 2. The pressure and, current or safety factor, profiles can be input to VMEC in several ways. The methods of choice are either a 20 degree polynomial power series (with a maximum of 20 powers) or a cubic spline approximation. We use the polynomial approximation for the pressure and the cubic spline approximation for the rotational transform. The magnetic field due to the external coils can be provided as an input for free-boundary simulations. The vacuum magnetic field generated by these coils is obtained with the auxiliary code MAKEGRID. MAKEGRID uses the Biot-Savart law

$$\mathbf{B}(\mathbf{x}) = \frac{\mu_0}{4\pi} \int_V \mathbf{J}(\mathbf{x}') \frac{\mathbf{x} - \mathbf{x}'}{|\mathbf{x} - \mathbf{x}'|} dV' \quad (3.14)$$

to calculate an externally applied magnetic field from prescribed currents flowing through each coil.



### 3.1.2 VMEC's variational formulation of ideal MHD

In order to find solutions of the MHD force balance equation, VMEC uses a variational formulation instead of directly solving the MHD force balance equation 2.36. This means that a variation of the MHD plasma energy is done, until it is minimised. Following (57), the MHD plasma energy for a static equilibrium is composed of magnetic energy and fluid energy, which can be written in VMEC coordinates as

$$W = W_m + W_f = \int \left( \frac{B^2}{\mu_0 2} + \frac{P(s_V)}{\Gamma - 1} \right) \sqrt{g_V} ds_V d\theta_V \phi_V = \int \frac{B^2}{\mu_0 2} \sqrt{g_V} ds_V d\theta_V \phi_V + \int_0^1 \frac{M(s_V)}{\Gamma - 1} V'^{1-\Gamma} ds_V \quad (3.15)$$

where, in the second equality, we have used the fact that the equilibrium pressure is a given flux function. We also used the adiabatic closure given by equation 2.30 in the absence of strong flows.  $M(s_V)$  is the mass function. We can then take the variation of the energy 3.15 relative to an artificial time parameter  $t$ . It is worth noting here that the VMEC coordinates are fixed, because we want these coordinates to be our independent variables. During the process of energy minimisation, the energy will be changed by changing the plasma shape which is given by the variation of the cylindrical coordinates  $(R, \phi_{geo}, Z)$ . Nevertheless,  $\phi_V = -\phi_{geo}$  and thus the 'time' variation of the cylindrical angle  $\phi_{geo}$  is also taken to be zero. An additional quantity is assumed to vary in time. This quantity is the function  $\tilde{v}_V$  appearing in contravariant magnetic field representation 3.3. Therefore, every equilibrium solution provided by VMEC will have a specific  $\tilde{v}_V$ , and thus a specific poloidal angle  $\theta_V$  associated with it. This angle is the one that most efficiently minimises the solution, and converges the equilibrium. The variation of a general quantity  $\varkappa$  in the variation of energy in VMEC is thus taken as

$$\delta \varkappa = \frac{d\varkappa}{dt} = \frac{\partial \varkappa}{\partial R} \frac{\partial R}{\partial t} + \frac{\partial \varkappa}{\partial Z} \frac{\partial Z}{\partial t} + \frac{\partial \varkappa}{\partial \tilde{v}_V} \frac{\partial \tilde{v}_V}{\partial t}. \quad (3.16)$$

Using equation 3.16, the variation of the energy is given by (57)

$$\frac{dW}{dt} = - \int \left( F_R \frac{\partial R}{\partial t} + F_Z \frac{\partial Z}{\partial t} + F_{\tilde{v}_V} \frac{\partial \tilde{v}_V}{\partial t} \right) ds_V d\theta_V \phi_V \quad (3.17)$$

$$- \int_{s_V=1} \sqrt{g}|_V \left( \frac{B^2}{\mu_0 2} + \frac{P(s)}{\Gamma - 1} \right) \left( \frac{\partial s_V}{\partial R} \frac{\partial R}{\partial t} + \frac{\partial s_V}{\partial Z} \frac{\partial Z}{\partial t} \right) d\theta_V \phi_V \quad (3.18)$$

in which the second term gives the energy at the boundary (last closed flux surface). In fixed boundary simulations this term vanishes, as the boundary does not vary, but in free boundary cases this term is nonzero. The forces are given by

$$\begin{aligned}
F_R = & -\frac{\partial}{\partial s_V} \left[ |\sqrt{g_V}| \frac{\partial s}{\partial R} \left( \frac{B^2}{2\mu_0} + P \right) \right] - \frac{\partial}{\partial \theta_V} \left[ |\sqrt{g_V}| \frac{\partial \theta_V}{\partial R} \left( \frac{B^2}{2\mu_0} + P \right) \right] \\
& - \frac{\partial}{\partial \phi_V} \left[ |\sqrt{g_V}| \frac{\partial \phi_V}{\partial R} \left( \frac{B^2}{2\mu_0} + P \right) \right] + \frac{|\sqrt{g_V}|}{\mu_0} \nabla \cdot [(\mathbf{B} \cdot \nabla R) \mathbf{B}] \\
& + \frac{|\sqrt{g_V}|}{\mu_0} \left( \frac{B^2}{2\mu_0} + P - \frac{R^2 (B^{\phi_V})^2}{\mu_0} \right),
\end{aligned} \tag{3.19}$$

$$\begin{aligned}
F_Z = & -\frac{\partial}{\partial s_V} \left[ |\sqrt{g_V}| \frac{\partial s}{\partial Z} \left( \frac{B^2}{2\mu_0} + P \right) \right] - \frac{\partial}{\partial \theta_V} \left[ |\sqrt{g_V}| \frac{\partial \theta_V}{\partial Z} \left( \frac{B^2}{2\mu_0} + P \right) \right] \\
& - \frac{\partial}{\partial \phi_V} \left[ |\sqrt{g_V}| \frac{\partial \phi_V}{\partial Z} \left( \frac{B^2}{2\mu_0} + P \right) \right] + \frac{|\sqrt{g_V}|}{\mu_0} \nabla \cdot [(\mathbf{B} \cdot \nabla Z) \mathbf{B}],
\end{aligned} \tag{3.20}$$

$$F_{\tilde{v}_V} = \frac{d\Psi_T}{ds_V} \frac{|\sqrt{g_V}|}{\mu_0 \sqrt{g_V}} \left( \frac{B_{\phi_V}}{\partial \theta_V} - \frac{B_{\theta_V}}{\partial \phi_V} \right). \tag{3.21}$$

The minimisation of energy in the fixed boundary case is equivalent to minimising the variations of the plasma shape given by

$$\frac{\partial R}{\partial t} = F_R, \tag{3.22}$$

$$\frac{\partial Z}{\partial t} = F_Z, \tag{3.23}$$

$$\frac{\partial \tilde{v}_V}{\partial t} = F_{\tilde{v}_V}. \tag{3.24}$$

The minimised state results when these forces are null. The precision to which these constraints have to be satisfied can be given as an input in VMEC.

### 3.1.3 VMEC equilibrium for modelling a JET pulse with 1/1 internal kink

In this thesis, we use VMEC to model tokamak plasmas with long living non-resonant 3D MHD saturated perturbations and obtain a suitable magnetic configuration. Particularly, we are interested in modelling long living 1/1 internal kink modes that can be present during hybrid plasma scenario operation. These modes of interest are used tokamaks, like JET and ASDEX, and will be used in ITER (see section 1.7).

The 1/1 internal kink mode is a rigid shift of the flux surfaces near the magnetic axis of the plasma. The displacement makes the plasma have one poloidal excursion while going one time along the toroidal direction, being thus characterised by a poloidal mode number  $m = 1$  and toroidal mode number  $n = 1$  in the magnetic field spectrum. It usually happens when the safety factor  $q(s_V)$  near the plasma center relaxes from higher values than unity (71). If the

safety profile reaches  $q = 1$  or lower, it usually leads to a nonlinear evolution of the mode with the generation of a magnetic island. It is often the case in hybrid scenario operation that a long living 1/1 mode is present with flat or reversed (non-monotonic) safety factor profiles. These profiles usually have their minimum value  $q_{min} > 1$  indicating that they are saturated and no magnetic island is present. The mode can thus live during operation without further deterioration via reconnection. We are interested in such scenarios. One of these scenarios can be seen in JET pulse #92181 (see figure 3.2).

In figure 3.2a, we see the timetrace of the line averaged electron density, central electron temperature and central SXR (soft X-ray) tomography signal for JET pulse #92181. This experiment is a hybrid pulse with H-mode configuration, with axial magnetic field  $B \approx 2.11 T$ , plasma current  $I_p \approx 1.82 MA$ , Ohmic power  $P_{OHM} \approx 3.5 MW$ , NBI power  $P_{NBI} \approx 22 MW$ , and ICRH power  $P_{ICRH} \approx 1.5 MW$ . In figure 3.2b, the time evolution of the toroidal mode number of the magnetic field perturbation is shown. In the time interval 45s – 46.66s relevant for the transport times considered in this thesis, the toroidal mode number evolution (see fig. 3.2b) shows three distinct phases. In an initial phase, the plasma is weakly 3D and thus essentially axisymmetric (before  $t = 46.51s$ ). This phase is followed by the appearance of growing fish-bones (between  $t = 46.51s$  and  $t = 46.61s$ ), and then culminates in a third phase in which a strong continuous 1/1 internal kink mode is established in the plasma (after  $t = 46.61s$ ). The SXR tomography is an experimental diagnostic which uses the direct measure of the radiation emitted by the heavy impurity ions in the plasma. As stated in figure 1.6 when the tungsten ions reach the core region of the plasma they can collide with the background ions. As a consequence the thermal energy is transformed into radiation. This is because the thermal energy of the plasma excites some of the electrons still bound to the tungsten ions (the ones with the most energetic orbits), which in the de-excitation phase will emit in the soft X-ray spectrum. The line of sight intensity of such radiation is directly measured by the SXR diagnostic and then an Abel inversion is made to construct a 2D map of the SXR emissivity on the poloidal cross section of the plasma. Such emissivity is thus a measure of the position of the tungsten ions in the plasma. It is seen from figure 3.2a that the SXR radiation (measured at the center of the plasma) becomes large at around 46.6s. This indicates the appearance of a strong long living 1/1 mode. Relevant comparisons for the work in this thesis are therefore to be made between the first and the third phases just described. Indeed, at these times, we see different SXR radiation patterns possibly linked to (causing or affected by) the enhanced kink amplitude. For example, figures 3.3a and 3.3b show, respectively, the SXR tomography for JET pulse #92181 at an early time when the pulse is mostly axisymmetric, and at a time within the phase in which a strong 1/1 mode is present in the plasma. We see, in figure 3.3a that impurities accumulate off-axis, while in figure 3.3b impurities accumulate on-axis. Although the temperature and density change slightly over the three phases (see figure 3.2), we neglect these effects in favour of isolating the 3D effects<sup>1</sup>. The rotation profile throughout the relevant time interval is found to be almost unchanged. Indeed, the magnetic equilibrium can ‘slip’

<sup>1</sup>The neglect of the effects in thermal and density profiles on the impurity transport will be justified later, where we will see that such effect cannot cause transport on the timescales observed.

to a new 3D state quite quickly, but the temperature, density and rotation profiles change on slower timescales (cross-field transport timescales).

In order to model such a mode with VMEC, we need to provide a suitable pressure profile, the safety factor (or equivalently a rotational transform), and a guess of the geometry of the last closed flux surface. While the pressure profile and the last closed flux surface geometry are easily obtained from experimental reconstruction, the safety factor reconstruction is often not good enough in the core. To match the amplitude of the 1/1 internal kink displacement in VMEC with the experimental measurement of the 1/1 kink mode, we may adjust the safety factor profile in VMEC. By moving the low shear region of the  $q$ -profile increasingly close to unity (from above), the amplitude of the kink mode increases. We select the  $q$ -profile that yields a VMEC generated kink amplitude that best agrees with soft X-ray tomography for a pulse with a 1/1 continuous mode, and observed tungsten accumulation. Experimental soft X-ray (SXR) tomography identifies the magnetic axis position, and its deviation from a similar axisymmetric plasma defines the 1/1 kink amplitude. In order to obtain the displacement of the saturated kink mode displacement we may look at tomography during the third phase, in which the 1/1 mode is strong. The impurities will rotate in the poloidal direction following the helical excursion of the kink mode. Thus, the hot light spot in the SXR tomography will rotate in the poloidal direction with time. This helical movement of the light spot can be used to approximately obtain the kink mode displacement, which as mentioned can be reproduced with VMEC.

We use the safety factor and pressure profiles in figure 3.4 to obtain a 1/1 internal kink mode (see figures 3.7 and 3.6), to model the time at 3.3b in the phase of the pulse in which the plasma is strongly 3D. To compare with the time phase in which the plasma is mostly axisymmetric, we obtain an axisymmetric equilibrium (see figure 3.5) with the same profiles, but imposing axisymmetry (by setting the only possible toroidal mode number  $n$  to zero). We could instead allow weak 3D associated with large  $q_{min}$ , but the mentioned approach is clearer and easier. The radial displacement between the two equilibria is approximately  $9cm$  in order to best match the experiment. We can see the evolution of the magnetic axis and the last closed flux surface along the toroidal angle for the axisymmetric equilibrium and 1/1 internal kink respectively in figures 3.5a and 3.6a. We see that the magnetic axis for the axisymmetric equilibrium is always on the  $Z = 0$  plane, while for the 1/1 internal kink it has a helical excursion as expected. The boundary does not change in both cases. The flux surfaces for  $s_V = 0.0391$ ,  $s_V = 0.1261$ , and  $s_V = 0.8652$  can be seen for the axisymmetric equilibrium in figure 3.5c. All the surfaces are axisymmetric and symmetrical relative to the  $Z = 0$  plane. We can see the same view of such surfaces for the 1/1 internal kink mode in figure 3.6c. We see that the innermost surfaces in the core region of the tokamak are helically kinked as expected. A poloidal cross section of the flux surfaces at  $\phi_V = 0$  can be seen for the axisymmetric in figure 3.5c. It is identical for every toroidal angle. The vertical and horizontal red lines mark the magnetic axis for the axisymmetric case. Such cross section is shown for the 1/1 internal kink mode at four different toroidal angles in figure 3.7, in which we can see the helical displacement of the core region of the plasma. The spectrum of different modes of the

magnetic field magnitude of the 1/1 internal kink equilibrium are presented in figure 3.8. We can see that the  $(m, n) = (1, 1)$  mode is observed with stronger amplitude in the zone in which the safety factor is close to unity.

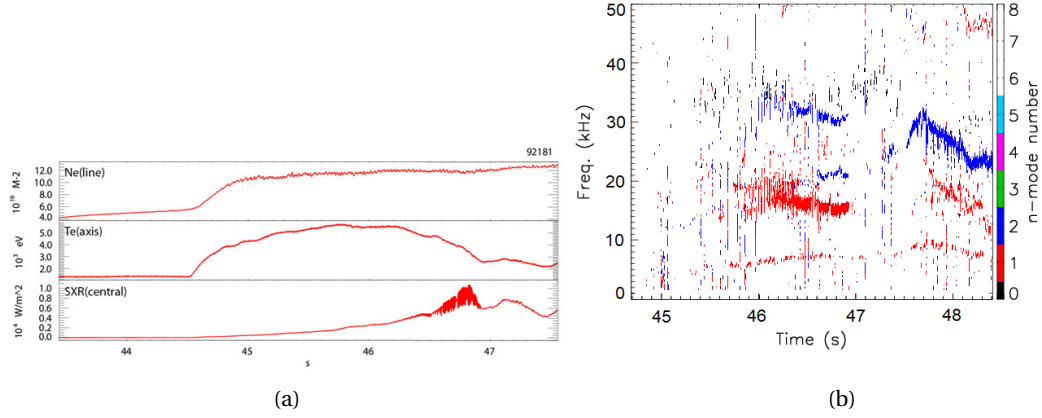


Figure 3.2 – Timetraces for JET pulse #92181. (a) Electron density and temperature close to the magnetic axis, and SXR signal at the central region of the plasma. (b) Evolution of the toroidal mode number frequency for different toroidal mode numbers  $n$ .

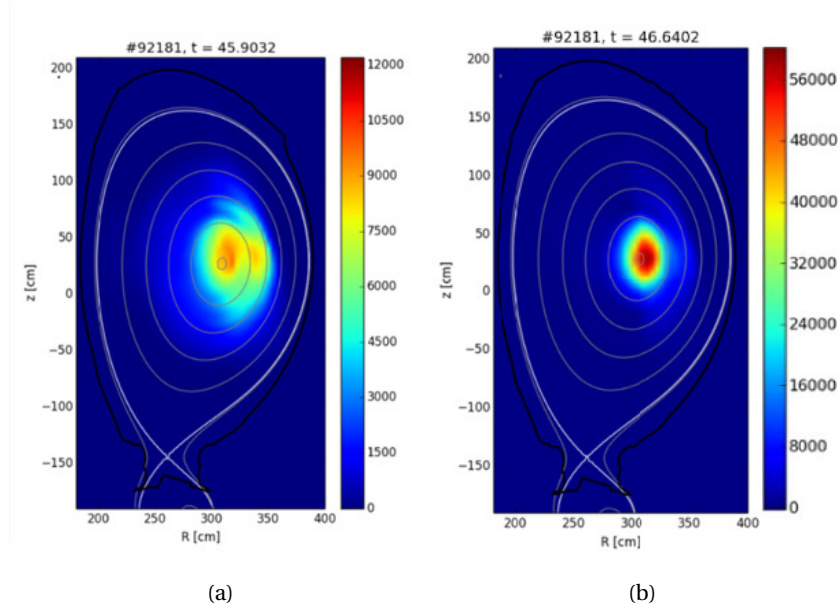


Figure 3.3 – Soft X-ray (SXR) tomography at different times of pulse #92181. (a) SXR signal at  $t \approx 45.9 \text{ s}$  of fig. 3.2, where the  $n = 1$  magnetic signal is weak and thus the plasma is essentially axisymmetric. (b) SXR signal at  $t \approx 46.64 \text{ s}$  of fig. 3.2, where the  $n = 1$  magnetic signal is strong and thus a strong 1/1 internal kink mode is present in the plasma. The axis position is given by the highest intensity region since impurities follow the axis of the kink.

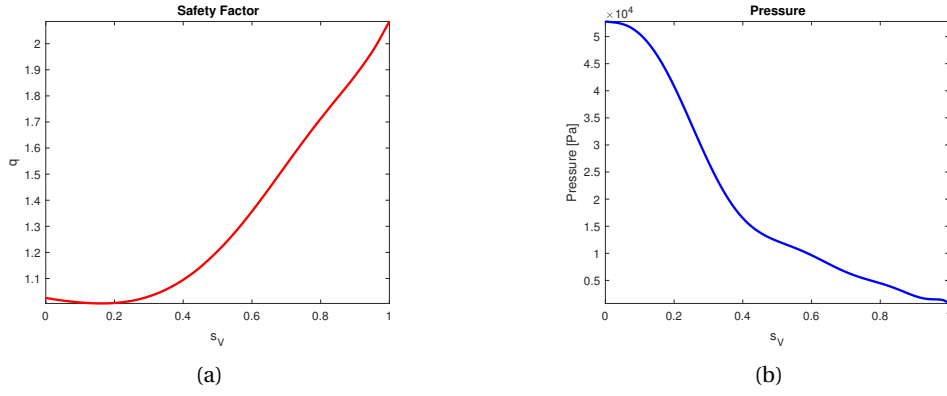


Figure 3.4 – Input profiles of VMEC to obtain the main 1/1 internal kink mode studied in this thesis. (a) Safety factor profile. (b) Pressure profile.

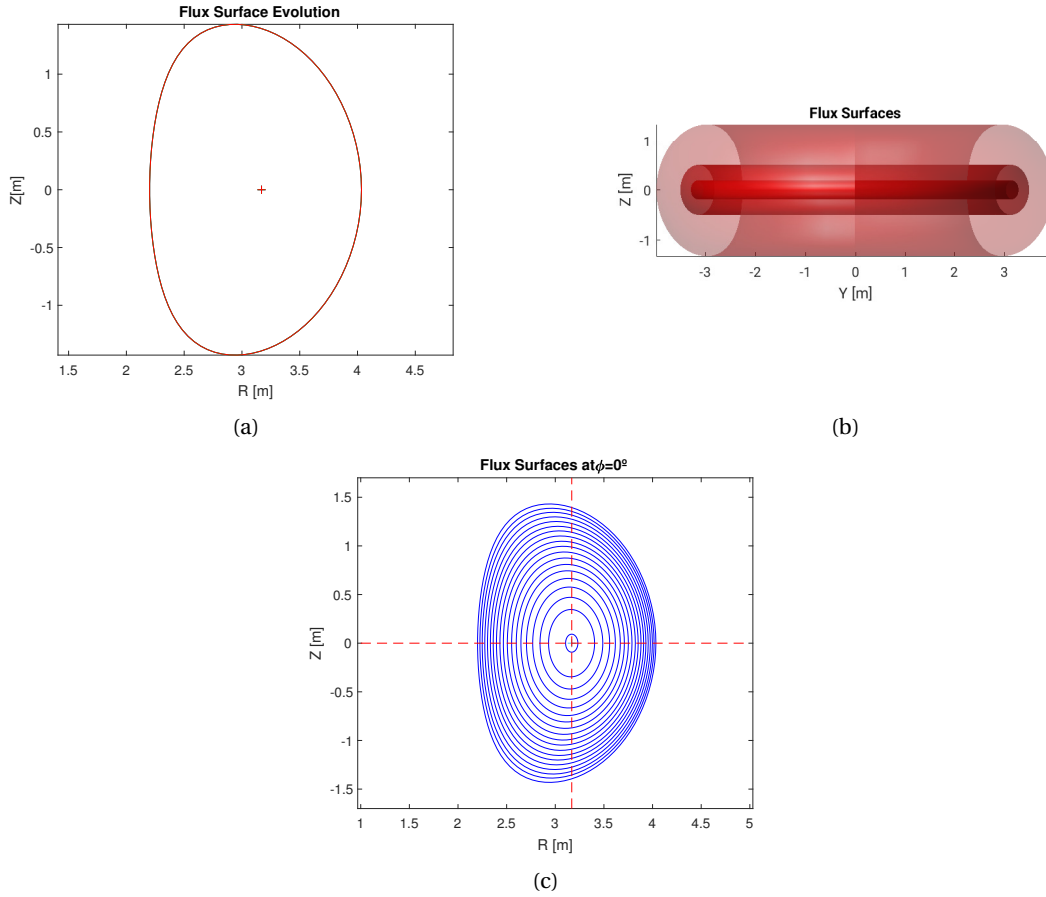


Figure 3.5 – Axisymmetric equilibrium obtained with the same profiles (see figure 3.4) as the 1/1 internal kink mode in figures 3.7 and 3.6, but imposing the toroidal mode numbers  $n = 0$ . (a) Flux surface evolution along the toroidal angle  $\theta_V$ . (b) Flux surfaces  $s_V = 0.0391$ ,  $s_V = 0.1261$  and  $s_V = 0.8652$  ( $ZY$ -plane view). (c) Poloidal cross-section of flux surfaces at  $\theta_V = 0^\circ$ .

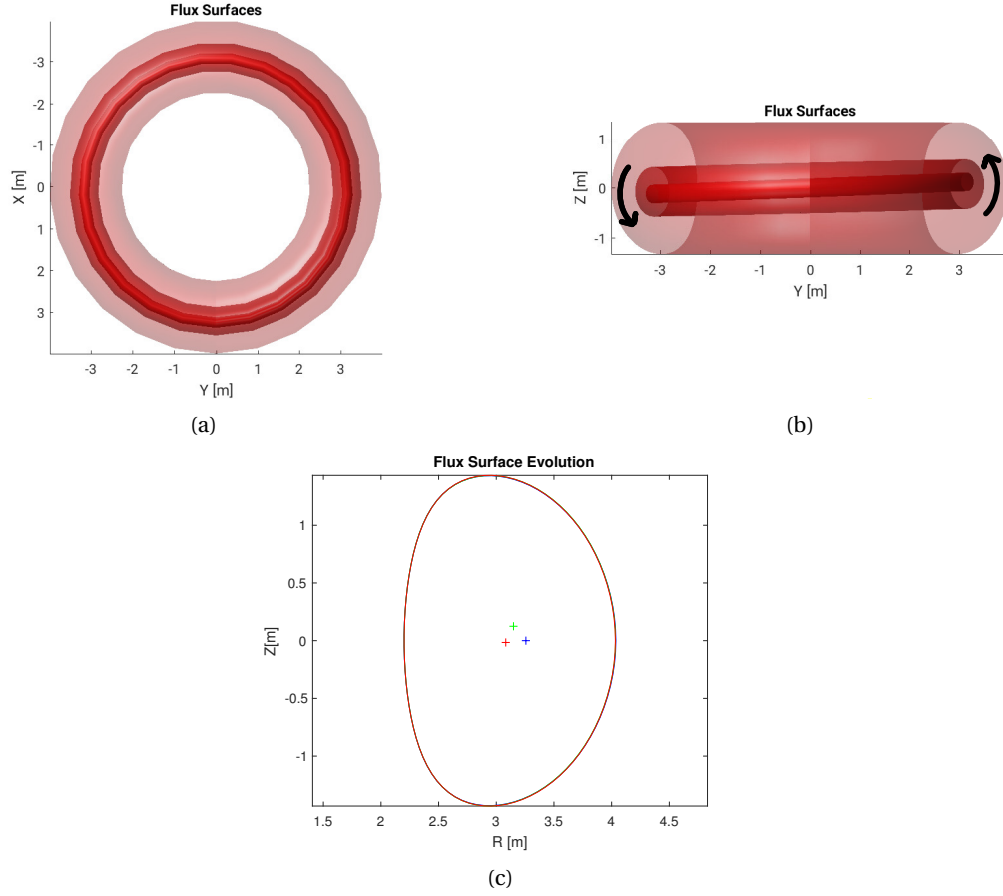


Figure 3.6 – Flux surfaces  $s_V = 0.0391$ ,  $s_V = 0.1261$  and  $s_V = 0.8652$  for the largest displacement 1/1 internal kink mode studied in this thesis. This mode is used to model the JET pulse #92182 in the strong 3D region and it is obtained with the profiles in figure 3.4. (a) Flux surfaces  $s_V = 0.0391$ ,  $s_V = 0.1261$  and  $s_V = 0.8652$  (XY-plane). (b) Flux surfaces  $s = 10$ ,  $s = 30$  and  $s = 200$  (ZY-plane). The black arrows indicate the movement of the kinked magnetic axis from axisymmetry to 3D. (c) Flux surface evolution along the toroidal angle  $\theta_V$ .

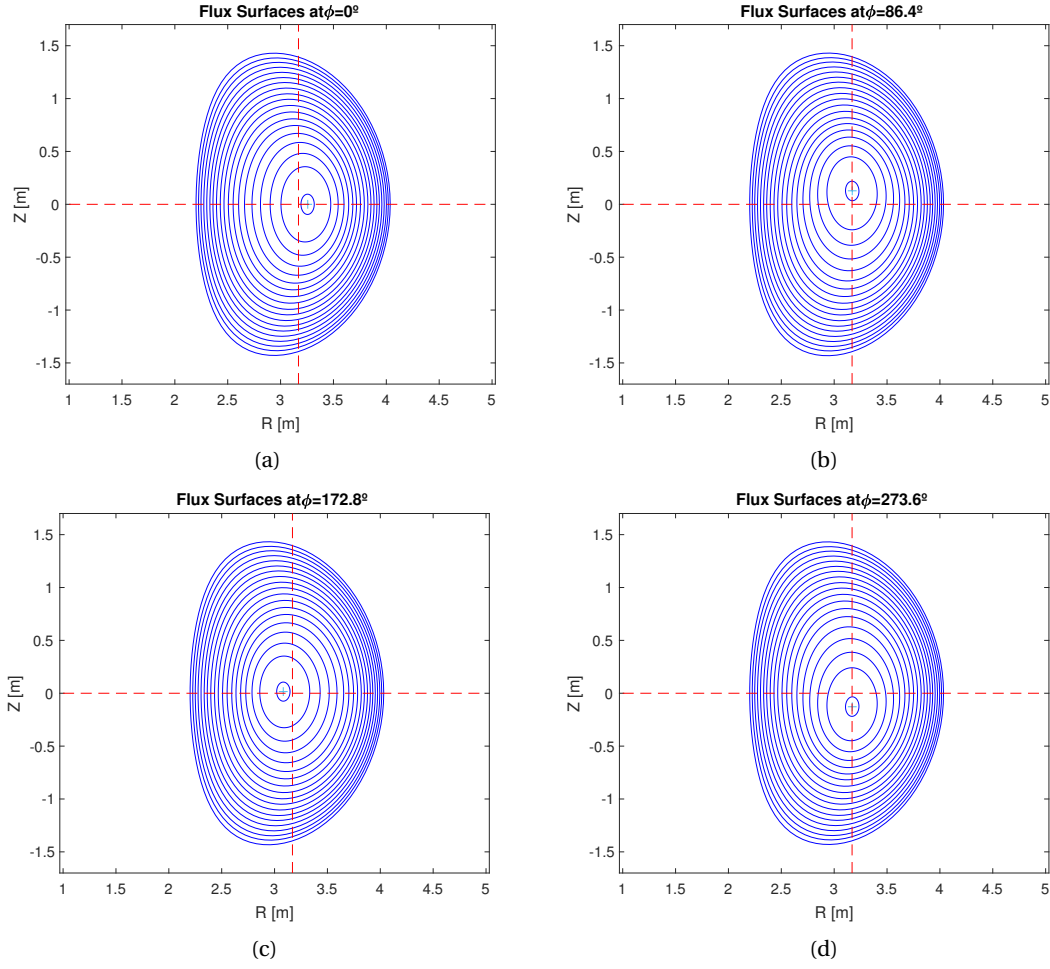


Figure 3.7 – Flux surfaces for the largest displacement 1/1 internal kink mode studied in this thesis. (a) At  $\theta_V = 0^\circ$ . (b) At  $\theta_V = 86.4^\circ$ . (c) At  $\theta_V = 172.8^\circ$ . (d) At  $\theta_V = 273.6^\circ$ .

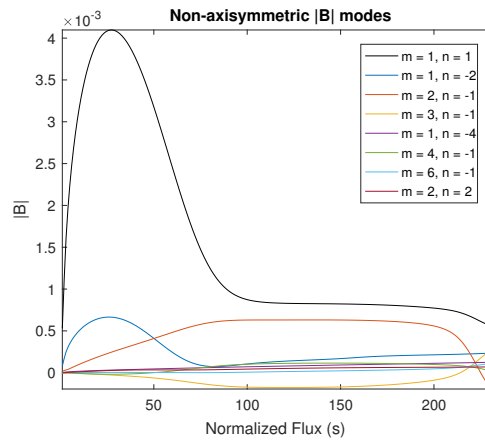


Figure 3.8 – Non-axisymmetric modes for the 1/1 internal kink mode studied in this thesis and used to model the pulse #92181.



The numerical magnetic equilibria just described (see figures 3.5, 3.6 and 3.7) can be used as a direct input for the VENUS-LEVIS code to follow the tungsten particles as it is, i.e. using VMEC coordinates. Nevertheless, we still need to calculate the background ion flow and the heat flux (see section 2.6) from these magnetic configurations. Calculating the geometrical factors necessary to solve for such quantities is more easily achieved by transforming the numerical magnetic equilibria from VMEC coordinates to Boozer or Hamada coordinates. In order to do this, auxiliary codes have been developed which are described in the next two sections 3.1.4 and 3.1.5.

### 3.1.4 Converting from VMEC to Boozer and Hamada coordinates

In order to convert VMEC coordinates to Boozer or Hamada coordinates, we start by noticing that the VMEC coordinates can be made straight by redefining the poloidal coordinate (see section 3.1.1). Notice that we do not have to redefine the toroidal coordinate for the procedure of developing VMEC-like straight field line coordinates. Hence, the new poloidal coordinate is

$$\theta_V^* = \theta_V + \frac{d\Psi_T^{-1}}{ds_V} \tilde{v}_V(s_V, \theta_V, \phi_V). \quad (3.25)$$

In this new set of coordinates the jacobian can be written as

$$\sqrt{g_V^*} = \frac{\sqrt{g_V}}{1 + \frac{d\Psi_T^{-1}}{ds_V} \frac{\partial \tilde{v}}{\partial \theta_V}}. \quad (3.26)$$

These quantities are easily obtained from the VMEC output. And thus, we can transform all quantities from VMEC coordinates into this set of VMEC straight field line coordinates. These quantities are computed in Fourier space for the poloidal and toroidal angles, and for the flux coordinate  $s_V$ , a cubic spline interpolation is made. In these coordinates, the magnetic operator  $\mathbf{B} \cdot \nabla$  has already been simplified. However, the right hand side of the magnetic differential equation necessary to be solved to obtain the geometrical factors  $u$  and  $g_4$  (see equations 2.85 and 2.92 in section 2.6) are further simplified by working in Boozer or Hamada coordinates. Transforming from VMEC-like straight field line coordinates to Boozer or Hamada coordinates, is easier than directly from VMEC coordinates. The reason being that in order to do such a transformation we also have to solve magnetic differential equations which feature the magnetic differential operator. Such magnetic differential equations are

$$\mathbf{B} \cdot \nabla \tilde{w}_V^*(s_V, \theta_V^*, \phi_V^*) = \frac{dP}{ds_V} + \frac{dI_T}{ds_V} B^{\theta_V^*} + \frac{dI_P}{ds_V} B^{\phi_V^*}, \quad (3.27)$$

$$\mathbf{B} \cdot \nabla \tilde{u}_V^*(s_V, \theta_V^*, \phi_V^*) = B^2 - I_T B^{\theta_V^*} - I_P B^{\phi_V^*}. \quad (3.28)$$

These magnetic differential equations are valid in any set of flux coordinates and its derivation can be seen in appendix A. They are here used to obtain the functions  $\tilde{w}_V^*$  and  $\tilde{u}_V^*$  for the VMEC straight field line coordinates. These functions are important for the calculation of the generator functions of Boozer and Hamada coordinates that can be written (see appendix A for more details) respectively as

$$G_B(s_V, \theta_V^*, \phi_V^*) = \frac{\tilde{u}_V^*(s_V, \theta_V^*, \phi_V^*)}{\frac{d\Psi_T}{ds_V}(I_p + \iota I_T)}, \quad (3.29)$$

$$G_H(s_V, \theta, \phi) = -\frac{\tilde{w}_V^*(s_V, \theta_V^*, \phi_V^*)}{\frac{d\Psi_T}{ds_V}(I_p + \iota I_T)}. \quad (3.30)$$

These generators are used to obtain the Boozer angles

$$\theta_B = \theta_V^* + \frac{d\Psi_P}{ds_V} G_B(s_V, \theta_V^*, \phi_V^*), \quad (3.31)$$

$$\phi_B = \phi_V + \frac{d\Psi_T}{ds_V} G_B(s_V, \theta_V^*, \phi_V^*), \quad (3.32)$$

and Hamada angles

$$\theta_H = \theta_V^* + \frac{d\Psi_P}{ds_V} G_H(s_V, \theta_V^*, \phi_V^*), \quad (3.33)$$

$$\phi_H = \phi_V + \frac{d\Psi_T}{ds_V} G_H(s_V, \theta_V^*, \phi_V^*). \quad (3.34)$$

The magnetic differential equations 3.27 and 3.28 are solved in the Fourier space by inverting the magnetic differential operator. In straight field line coordinates, the operator is written in Fourier space as  $(m \frac{d\Psi_P}{ds_V} - n \frac{d\Psi_T}{ds_V}) / \sqrt{g}$ . At rational surfaces in which the safety factor is  $q = m/n$ , the operator can be zero, which causes numerical singularities. The 3D 1/1 internal kink equilibrium obtained with VMEC avoids  $q = 1$ . However, other small residual exactly resonant 3D modes are present in the equilibrium (see figure 3.8). These 3D residual modes may cause current sheets that, in the framework of ideal MHD will manifest themselves as singularities. To remove such residual singularities we use a resonance detuning operator  $\Delta_{mn}$  (55). The detuning operator is written as

$$\Delta_{mn} = \Delta \left[ (m+1) \frac{d\Psi_P}{ds_V} - n \frac{d\Psi_P}{ds_V} \right], \quad (3.35)$$

with  $\Delta$  an input parameter usually taken to be  $\Delta = 10^{-4}$  as it provides the most efficient calculation, i.e. it efficiently smooths the undesirable residual singularities without having a noticeable effect on the overall behaviour of the solution. The inverted magnetic operator in

Fourier space is thus redefined as

$$\frac{\sqrt{g}}{m \frac{d\Psi_P}{ds_V} - n \frac{d\Psi_T}{ds_V}} \rightarrow \frac{\sqrt{g}(m \frac{d\Psi_P}{ds_V} - n \frac{d\Psi_T}{ds_V})}{\left(m \frac{d\Psi_P}{ds_V} - n \frac{d\Psi_T}{ds_V}\right)^2 + \Delta_{mn}^2}. \quad (3.36)$$

This procedure is applied for solving all magnetic differential equations in this thesis. The Boozer angles and Hamada angles can be used to reconstruct all the quantities of interest. Since for the calculation of geometrical factors, we need the poloidal and toroidal covariant components of the magnetic field, we need the Hamada coordinates description to be complete, and thus we need to calculate the  $\tilde{u}_H(s_V, \theta_H, \phi_H)$  in Hamada coordinates (see equation 2.58). This function can be obtained by solving the following magnetic differential equation

$$\mathbf{B} \cdot \nabla \tilde{u}_H(s_V, \theta_H, \phi_H) = B^2 - \langle B^2 \rangle \quad (3.37)$$

in Hamada coordinates.

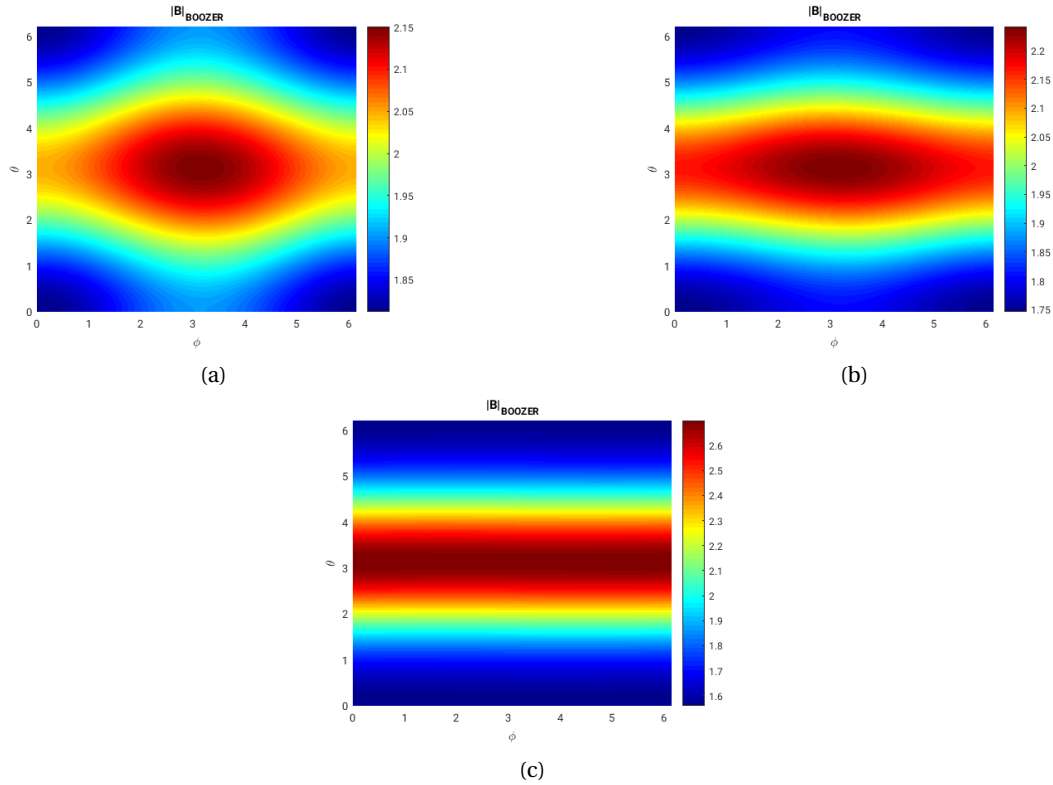


Figure 3.9 – Magnetic field magnitude in Boozer coordinates for the  $\theta\phi$ -plane for the 1/1 internal kink presented in figure 3.7. (a) At  $s_V = 0.0391$ , there is no symmetry on the magnetic field. (b) At  $s_V = 0.1261$ , the field still does not possess any symmetry. (c) At  $s_V = 0.8652$ , the field is axisymmetric.

For the 1/1 internal kink equilibrium presented in 3.7 the relative error calculated according to

$L^\infty$  norm is for the Boozer transformation of  $e_\infty = 0.25\%$ , and for the Hamada transformation of  $e_\infty = 0.31\%$ . Contour plots in the  $\theta - \phi$  plane of the magnetic field magnitude in Boozer coordinates are presented in figure 3.9. It is observed that no symmetry is present in the 1/1 internally kinked region of the plasma, so that it can be expected that significant NTV will occur. The main velocity profile  $U_{1/4}$  will be assumed toroidal in this 3D equilibrium, with 3D effects appearing at order  $U_1$  and  $U_{3/2}$  as explained earlier. We remark here that the ions are strongly subsonic  $M_I^2 \sim \delta^{1/2}$  and as such the toroidal rotation is still consistent with the general observation that 3D plasmas cannot flow strongly. This is so because the MHD magnetic configuration is essentially established by the main ions which are not flowing supersonically. The impurities are of trace density and thus they can flow supersonically in this 3D magnetic configuration without affecting the common flow which is dominantly set by the ion species. This can be understood by the fact that the ion-ion collision frequency is much larger than impurity-impurity collision frequency, due to the trace impurity limit being considered. Therefore, the parallel viscosity of the impurity population which provides a contribution to the common flow, will act on a much slower timescale than that of the ions. Thus the common flow is essentially set by the subsonic bulk ions.

The magnetic field configuration in Hamada or Boozer coordinates may now be used to fully define the geometrical factors  $u$ ,  $f_c$  and  $f_s$  needed for the background ion flows at each order.

### 3.1.5 Numerical calculation of geometrical factors and background flows

The geometrical factors  $u$ ,  $f_c$ ,  $f_s$  which have to be calculated to describe completely the background ion flows and heat flux were described in section 2.6. The geometrical factor  $w$  necessary to obtain the heavy impurity flow  $U_{w_1}$  was presented in section 2.10. The geometrical factor  $u$  is obtained from the solution of the magnetic differential equation given by

$$\mathbf{B} \cdot \nabla u = -\mathbf{B} \times \nabla \psi \cdot \nabla \left( \frac{1}{B^2} \right), \quad (3.38)$$

in which the integration constant is chosen to be  $u(B_{max}) = 0$ . The effective fraction of circulating particles is written as

$$f_c = \frac{3}{4} \frac{\langle B^2 \rangle}{B_{max}^2} \int_0^1 \frac{\lambda d\lambda}{\langle \sqrt{1 - \lambda B/B_{max}} \rangle}. \quad (3.39)$$

The geometrical factor  $f_s$  is written as

$$f_s = \frac{3}{4} \frac{\langle B^2 \rangle}{B_{max}^2} \int_0^1 \frac{\langle g_4 \rangle \lambda d\lambda}{\langle \sqrt{1 - \lambda B/B_{max}} \rangle}, \quad (3.40)$$

in which the  $g_4 = \xi g_5$ , with  $g_5$  obtained from solving the magnetic differential equation

$$\mathbf{B} \cdot \nabla g_5 = \mathbf{B} \times \nabla \psi \cdot \nabla \left( \frac{1}{\xi} \right), \quad (3.41)$$

with  $g_5(B_{max}) = 0$ . The geometrical factor  $w$  can be obtained from solving

$$\mathbf{B} \cdot \nabla (n_W w) = -\mathbf{B} \times \nabla \psi \cdot \nabla \left( \frac{n_W}{B^2} \right). \quad (3.42)$$

The magnetic differential equations 3.38 and 3.41 are solved in the same way as the ones described in section 3.1.4, either in Boozer or Hamada coordinates. The integrals in the equations 3.39 and 3.40 are performed over  $\lambda$  and the integrand is singular when approaching  $\lambda = 1$ . A hyperbolic tangent quadrature is used to numerically integrate the integrals. Such quadrature allows a better resolution in  $\lambda$  when approaching  $\lambda = 1$ . This value of  $\lambda$  marks the boundary layer between passing and trapped particles domains. The resonance present for passing particles in such a layer plays a key role in the neoclassical enhancement of the transport when compared to classical transport. The gain in resolution is thus important because it allows for a better numerical measure of the effect of the resonance as the ion diamagnetic flow  $\mathbf{U}_{I_1}$ , and as a consequence it allows to obtain a better description of its impact on heavy impurity transport. The geometrical factor  $f_s + \langle u B^2 \rangle$  obtained for the axisymmetric equilibrium presented in figure 3.5 and the 1/1 internal kink presented in figure 3.7 are shown in figure 3.10. The axisymmetric case is compared against the analytical solution and a good agreement is found.

The magnetic differential equation 3.42 can also be solved as 3.38 and 3.41. However, this equation has the particularity of depending on the impurity asymmetries. The drive of such asymmetries can depend on the case we are interested in study. In the cases of interest in this thesis the mechanism of interest is the presence of strong flows. Thus, in order to obtain the impurity density asymmetries that are necessary to solve equation 3.42 we need a model for the strong rotation  $\Omega(s_V)$  or equivalently the electric field  $E_{-3/4}$  (see equation 2.82). This value can be used to obtain the electric field  $E_{1/2}$  (see equation 2.116). With  $E_{-3/4}$  and  $E_{1/2}$  one is able to obtain the impurity asymmetries from equation 2.126. The rotation profile  $\Omega(s_V)$  can be obtained from the specific experiment in study. More details on such profile are given in next chapter (see section 4.2).

With  $u$ ,  $f_c$ ,  $f_s$  and  $w$  obtained, the background ion flow  $U_{I_1}$  and heat flux  $q_{I_1}$  (see section 2.6), as well as the impurity flow  $U_{W_1}$  (see section 2.10) can be easily obtained. These quantities and the magnetic equilibrium obtained with VMEC can then be input in the VENUS-LEVIS code to serve as an equilibrium in which we can follow the tungsten particles. The VMEC equilibrium is important in most computations in VENUS-LEVIS because it provides the magnetic field  $\mathbf{B}$ , while the flows and heat flux are of great importance when performing collisions of tungsten particles with the background. The next section will describe this code and how we use it to study tungsten transport.

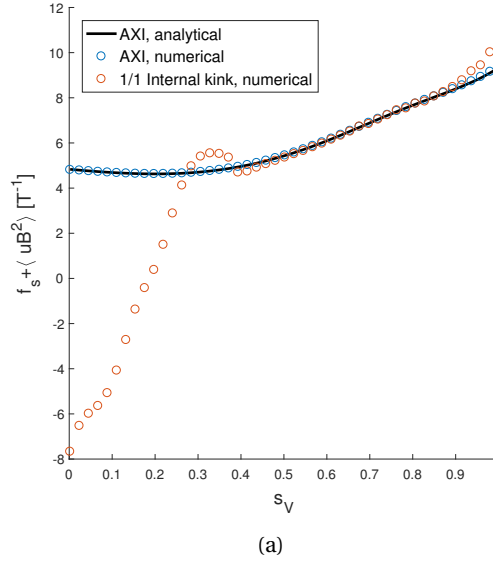


Figure 3.10 – Numerical solutions of the geometrical  $f_s + \langle uB^2 \rangle$  for the axisymmetric equilibrium in figure 3.5 and the 1/1 internal kink in figure 3.7. The numerical axisymmetric solution agrees well with the analytical solution (black). The geometrical factor inverts its sign in the internal kink region when compared to the axisymmetric case. This has an important effect on the flux average parallel ion flow  $\mathbf{U}_{I_1}$  as we will see in chapter 4.

### 3.2 VENUS-LEVIS for tracing heavy impurity guiding centers in the presence of strong flows and 3D geometry

The VENUS-LEVIS code is used to follow minority species in a bulk ion and electron background. In VENUS-LEVIS the minority impurity species is treated as in a full-f PIC code. However, the bulk species are treated as a static background and we neglect the effect of the minority species on themselves and on the background through collisions. Thus, we will treat impurities in the trace limit (as mentioned in section 2.5) which is a valid assumption in the core of a tokamak prior to strong radiation and temperature hollowing. VENUS-LEVIS has the possibility of following minority species with a guiding center description or with full 6D trajectories. We use the guiding center formalism in this work, as the heavy impurity Larmor radius is smaller than the Larmor radius of the bulk ions by a factor of  $\delta^{1/4}$ . Since heavy impurities flow supersonically, it is convenient to follow them in the frame rotating with the common velocity  $\mathbf{U}_{1/4}$ . It is also convenient to treat collisions in the frame where the bulk ions are flowing with their diamagnetic velocity. Nevertheless, it is important to capture the effect of the ambipolar electric field due to the different geometrical factors present in both ion flow  $\mathbf{U}_{I_1}$  and impurity flow  $\mathbf{U}_{W_1}$ . We thus have to follow impurities in the frame rotating with both the common velocity  $\mathbf{U}_{1/4}$  and the velocity  $\mathbf{U}_{W_1}$ , because this is the frame that can account properly (through the collision operator, see section 3.2.2), for the effect of the diamagnetic flows of the ions, and the difference between the ion and impurity flow components, that

### 3.2. VENUS-LEVIS for tracing heavy impurity guiding centers in the presence of strong flows and 3D geometry

depend on the ambipolar electric field  $\mathbf{E}_0$ . Notice that in axisymmetry this difference is zero and effectively only the ion diamagnetic effect is finite and we could follow the impurities in the the frame moving only with  $\mathbf{U}_{1/4}$  as done in ((55), (56)). The guiding center equations implemented in VENUS-LEVIS use the formalism described in (69), allowing for the required strong flow corrections (see section 2.12). At each time step in VENUS-LEVIS, the guiding center equations are solved for obtaining the position of the particle guiding centers and their parallel gyroradii. Then, collisions with the background are performed with a collision operator. We present the implementation of this guiding center formalism in the VENUS-LEVIS code in the next section. The following section 3.2.2 will explain the new implementation in VENUS-LEVIS of a collision operator which captures both the chosen background flow and heat flux.

#### 3.2.1 The guiding center description with strong flows

The guiding center equations implemented in VENUS-LEVIS uses the formalism described in (69) which was presented in section 2.12, allowing for the necessary strong flow corrections. VENUS-LEVIS evolves both the guiding center position  $\bar{x}_W$  in the lab frame and the parallel gyroradius  $\rho_{W\parallel}$  of the impurities in the frame rotating with  $\mathbf{U}^* = \mathbf{U}_{1/4} + \mathbf{U}_{W1}$ . The parallel gyroradius is used instead of the parallel velocity in the rotating frame for convenience (the total vector  $\mathbf{B}$  appears explicitly instead of  $\hat{b}$  inside the differential operators). These quantities are evolved at each time step according to the equations

$$\dot{\bar{x}}_W = \left( \mathbf{U}_{1/4} + \mathbf{U}_{W1} + \frac{q_W}{m_W B} \rho_{W\parallel} \right) \frac{\mathbf{B}^*}{\hat{b} \cdot \mathbf{B}^*} + \frac{\mathbf{E}^* \times \mathbf{B}}{\mathbf{B} \cdot \mathbf{B}^*}, \quad (3.43)$$

$$\rho_{W\parallel} \dot{=} \frac{\mathbf{E}^* \cdot \mathbf{B}}{\mathbf{B} \cdot \mathbf{B}^*}, \quad (3.44)$$

in which the modified magnetic field (see section 2.12) and the modified electric field are written as

$$\mathbf{B}^* = \mathbf{B} + \rho_{W\parallel} \nabla \times \mathbf{B} + \frac{m_W}{q_W} \nabla \times [\mathbf{U}_{1/4} + \mathbf{U}_{W1}], \quad (3.45)$$

$$\mathbf{E}^* = \mathbf{E}_{-3/4} + \mathbf{E}_{1/2} - \left( \frac{\mu}{q_W} + \frac{q_W}{m_W B} \rho_{W\parallel}^2 B \right) \nabla B - \frac{m_W}{q_W} \frac{\nabla(U_{1/4})^2}{2} - \rho_{W\parallel} \nabla(\mathbf{U}_{1/4} \cdot \mathbf{B}), \quad (3.46)$$

where the centrifugal and Coriolis terms due to the velocity  $\mathbf{U}_{W1}$  are neglected as they are small when compared with the other terms. The time integration of these equations at each time step is achieved using a 4th order Runge-Kutta algorithm with an adaptative timestep. The method has been shown to preserve energy and momentum to machine precision (60) for axisymmetric equilibria. We have also observed conservation of energy and momentum in the presence of strong flows for axisymmetric equilibria. The strong flow terms were implemented in VENUS-LEVIS for a general flow  $\mathbf{U}_{1/4}$

$$\mathbf{U}_{1/4} = U_{1/4}^{\theta_V} \mathbf{e}_{\theta_V} + U_{1/4}^{\phi_V} \mathbf{e}_{\phi_V}, \quad (3.47)$$

allowing for the possibility of poloidal and toroidal flows. This implementation of the different terms follows from the their definitions in curvilinear coordinates, and are given by

$$\frac{\nabla(U_{1/4}^2)}{2} = \mathbf{U}_{1/4} \cdot \vec{\nabla} \mathbf{U}_{1/4} = U_{1/4}^k \partial_k U_{1/4_j} - U_{1/4}^k \Gamma_{j,k}^i U_{1/4_i}, \quad (3.48)$$

$$\nabla(\mathbf{U}_{1/4} \cdot \mathbf{B}) = \mathbf{B} \cdot \vec{\nabla} \mathbf{U}_{1/4} + \mathbf{U}_{1/4} \cdot \vec{\nabla} \mathbf{B} = B^k \partial_k U_{1/4_j} - B^k \Gamma_{j,k}^i U_{1/4_i} + U_{1/4}^k \partial_k B_j - U_{1/4}^k \Gamma_{j,k}^i B_i, \quad (3.49)$$

$$\nabla \times \mathbf{U}_{1/4} = \frac{\epsilon^{ijk}}{\sqrt{g}} \partial_i U_{1/4_j} \mathbf{e}_k \quad (3.50)$$

in which identical indexes are understood to indicate summation over all coordinates, and the Christoffel symbols of second kind are given by

$$\Gamma_{j,k}^i = \frac{1}{2} g^{mi} (\partial_k g_{jm} + \partial_j g_{km} - \partial_m g_{jk}), \quad (3.51)$$

with  $g_{ij}$  the metric tensor.  $\epsilon^{ijk}$  is the Levi-Civita symbol.

The implementation of such general flows was used to account for the possibility of a symmetry direction of the 1/1 internal kink mode or other saturated modes of interest. However, as it could be seen in 3.9, the 1/1 internal kink does not possess any symmetry. We thus consider the common flow velocity to still be toroidal (as for axisymmetry), and to still exist, as observed in the experiment. Thus, for the simulations presented in this thesis we consider  $\mathbf{U}_{1/4} = -\Omega \mathbf{e}_\phi$  as per equation 2.82. The terms 3.48, 3.49 and 3.50 are computed in VMEC coordinates to use in the guiding-center equations. Nevertheless, for solving 2.115 for such a general 3D flow, Boozer or Hamada coordinates are used to simplify the magnetic differential equation. The guiding-center equations themselves do not take into account any collisional effects. Such effects are accounted for by a collision operator within the VENUS-LEVIS code. Its implementation will be discussed in next section 3.2.2. We now briefly discuss the particle initialisation for the sake of completeness. The impurity markers are initialised in VENUS-LEVIS using a rejection method to sample the following Maxwellian

$$f_0 = f_M(s_V, \theta_V, w_{\parallel}, w_{\perp}) = N_W(s_V) \left( \frac{m_W}{2\pi} \right)^{\frac{3}{2}} T_W(s_V)^{-\frac{3}{2}} e^{-\frac{m_W(w_{\parallel}^2 + w_{\perp}^2)}{T_W(s_V)}} e^{-10 \sin(\theta_V)}, \quad (3.52)$$

in which the factor  $e^{-10 \sin(\theta_V)}$  is added to mimic the fact that the tungsten enters the plasma from the divertor plates located in the bottom of the poloidal cross section (see figure 1.6).



### 3.2.2 Collisions between impurities and the background plasma

A realistic description of collisional neoclassical transport on heavy impurities requires a numerical description that has an accurate model for the parallel friction force and parallel thermal force between ions and impurities. In order to account for the effect of the ambipolar electric field on collisions we need to account for the difference between the components of the ion flow  $\mathbf{U}_I$  and impurity flow  $\mathbf{U}_{W_1}$  (see equations 2.86 and 2.127) that depend on the ambipolar electric field. If we follow the impurities in the frame moving with  $\mathbf{U}^* = \mathbf{U}^{1/4} + \mathbf{U}_{W_1}$  (see previous section 3.2.1), the flow of the background ions is effectively  $\mathbf{U}_{back} = \mathbf{U}_I - \mathbf{U}_{W_1}$ , and thus accounts not only for the diamagnetic effects of the ion flow, but also for the difference between the ion and impurity flows due to the ambipolar electric field term. We may then write the bulk ion distribution in the frame rotating with  $\mathbf{U}^*$  as a perturbed Maxwellian given by

$$f_I = f_{I_0}(\psi, \theta, v) \left[ 1 - \left( \frac{\mathbf{U}_{back}}{v_{th_I}^2} - \frac{\mathbf{q}_I}{P_I v_{th_I}^2} \left( 1 - \frac{v^2}{5v_{th_I}^2} \right) \right) \cdot \mathbf{v} \right], \quad (3.53)$$

where  $f_{I_0}(\psi, \theta, v)$  is the background ion Maxwellian and  $v$  is the velocity of the bulk ions in the frame rotating with  $\mathbf{U}_*$ . We then solve the Langevin equation at each timestep to obtain the velocity of each heavy impurity particle after a collision with the background ions. The Langevin equation to be solved can be written as

$$d\mathbf{w}_{coll} = \mathcal{A}^{WI} dt + \sigma_{ij}^{WI} d\mathbf{W} \quad (3.54)$$

where  $d\mathbf{w}_{coll}$  is the impurity velocity displacement after a collision with the bulk ions,  $\mathcal{A}^{WI}$  is the drift vector associated with the bulk ions background, and the tensor  $\sigma_{ij}^{WI}$  is related to the diffusion matrix of the bulk ions  $\mathcal{D}_{ij}^{WI}$  by

$$\mathcal{D}_{ij}^{WI} = \frac{1}{2} \sigma_{ij}^{WI} \sigma_{ij}^{WI T}. \quad (3.55)$$

Here,  $d\mathbf{W}$  is a vector of the independent Wiener processes. The drift vector and diffusion matrices can be obtained in terms of the Rosenbluth potentials  $\varphi_I$  and  $\psi_I$ :

$$\mathcal{A}^{WI} = \left( 1 + \frac{m_Z}{m_I} \right) L^{WI} \nabla_{\mathbf{w}} \varphi_I \quad (3.56)$$

and

$$\mathcal{D}_{ij}^{WI} = -L^{WI} \nabla_{\mathbf{w}}^2 \psi_I, \quad (3.57)$$

where  $L_{WI} = (q_I q_W / (m_W \epsilon_0))^2 \ln \Lambda$  and the Rosenbluth potentials are defined (9) as

$$\varphi_I(\mathbf{w}) = -\frac{1}{4\pi} \int \frac{1}{|\mathbf{w} - \mathbf{v}'|} f_I(\mathbf{v}') d^3 v' \quad (3.58)$$

$$\psi_I(\mathbf{w}) = -\frac{1}{8\pi} \int |\mathbf{w} - \mathbf{v}'| f_I(\mathbf{v}') d^3 v'. \quad (3.59)$$

For the background ion distribution function of interest 3.53, the Rosenbluth potentials are written as

$$\varphi_I(\mathbf{w}) = -\frac{N_I}{4\pi\beta^{1/2}} \left[ \frac{\zeta(w_b)}{w_b} + \mathbf{U}_{back} \cdot \mathbf{w} \beta \left( \frac{\zeta(w_b)}{w_b^3} - \frac{\zeta'(w_b)}{w_b^2} \right) - \frac{4}{5} \frac{\mathbf{q}_I \cdot \mathbf{w} \beta^2}{m_I N_I} \zeta'(w_b) \right], \quad (3.60)$$

$$\begin{aligned} \psi_I(\mathbf{w}) = & -\frac{N_I \beta^{1/2}}{8\pi} \left[ \frac{\zeta(w_b) + w_b \zeta(w_b)}{2w_b^2} + \frac{\zeta'(w_b)}{2} \right. \\ & \left. + \mathbf{U}_{back} \cdot \mathbf{w} \beta \left( \frac{\zeta(w_b) + w_b^2 \zeta(w_b)}{2w_b^3} - \frac{\zeta'(w_b)}{2w_b^2} \right) - \frac{4}{5} \frac{\mathbf{q}_I \cdot \mathbf{w} \beta^2}{m_I N_I} \left( \frac{\zeta(w_b)}{2w_b^3} - \frac{\zeta'(w_b)}{2w_b^2} \right) \right]. \end{aligned} \quad (3.61)$$

with  $\beta = v_{thI}^{-2}$ ,  $\zeta(w_b)$  the error function and  $w_b = w/v_{thI}$ . The drift vector is thus given by

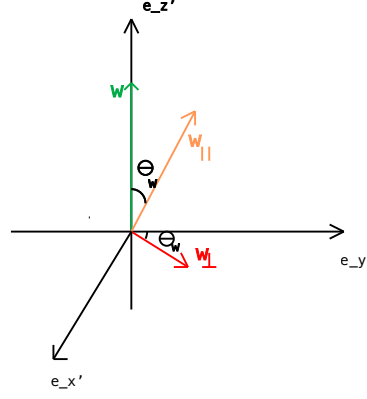
$$\begin{aligned} \mathcal{A}^{WI} = & -\left(1 + \frac{m_Z}{m_I}\right) L^{WI} \frac{N_I \beta^{3/2}}{4\pi} \left\{ \frac{\zeta'(w_b) w_b + \zeta(w_b)}{w_b^3} \right. \\ & \left. + \mathbf{U}_{back} \cdot \mathbf{w} \beta \left[ \frac{-3\zeta(w_b) + (3w_b + 2w_b^2)\zeta'(w_b)}{w_b^5} \right] - \frac{4}{5} \frac{\mathbf{q}_I \cdot \mathbf{w} \beta^2}{m_I N_I} 4\zeta'(w_b) \right\} \mathbf{w} \\ & - \left(1 + \frac{m_Z}{m_I}\right) L^{WI} \frac{N_I \beta^{1/2}}{4\pi} \left[ \mathbf{U}_{back} \beta \left( \frac{\zeta(w_b)}{w_b^3} - \frac{\zeta'(w_b)}{w_b^2} \right) - \frac{4}{5} \frac{\mathbf{q}_I \beta^2}{m_I N_I} \zeta'(w_b) \right], \end{aligned} \quad (3.62)$$

and the diffusion matrix by

$$\begin{aligned} \mathcal{D}_{ij}^{WI} = & L^{WI} \frac{N_I \beta^{1/2}}{8\pi} \left\{ \frac{\zeta'(w_b) w_b + (2w_b^2 - 1)\zeta(w_b)}{2w_b^3} + \mathbf{U}_{back} \cdot \mathbf{w} \beta \left[ \frac{(2w_b^2 + 3)\zeta(w_b) + 3w_b \zeta'(w_b)}{w_b^5} \right] \right. \\ & \left. - \frac{4}{5} \frac{\mathbf{q}_I \cdot \mathbf{w} \beta^2}{m_I N_I} \left[ \frac{-3\zeta(w_b) + (2w_b^3 + 3w_b)\zeta'(w_b)}{2w_b^5} \right] \right\} \left( \mathcal{S} - \frac{\mathbf{w} \mathbf{w}}{w w} \right) \\ & + L^{WI} \frac{N_I \beta^{1/2}}{8\pi} \left\{ \frac{-w_b \zeta'(w_b) + \zeta(w_b)}{w_b^3} + \mathbf{U}_{back} \cdot \mathbf{v} \beta \left[ \frac{(6 + 2w_b^2)\zeta(w_b) - (2w_b^3 + 6w_b)\zeta'(w_b)}{w_b^5} \right] \right. \\ & \left. - \frac{4}{5} \frac{\mathbf{q}_I \cdot \mathbf{w} \beta^2}{m_I N_I} \left[ \frac{6\zeta(w_b) - (2w_b^5 + 4w_b^3 + w_b)\zeta'(w_b)}{w_b^5} \right] \right\} \frac{\mathbf{w} \mathbf{w}}{w w} \\ & + L^{WI} \frac{N_I \beta^{1/2}}{8\pi} \beta \left[ \frac{(2w_b^2 - 3)\zeta(w_b) + 3w_b \zeta'(w_b)}{w_b^5} (\mathbf{U}_{back} \cdot \mathbf{w} + \mathbf{w} \cdot \mathbf{U}_{back}) \beta \right. \\ & \left. + \frac{-3\zeta(w_b) + (2w_b^3 + w_b)\zeta'(w_b)}{w_b^5} \left( \frac{\mathbf{q}_I \cdot \mathbf{w} + \mathbf{w} \cdot \mathbf{q}_I}{m_W} \right) \beta^2 \right]. \end{aligned} \quad (3.63)$$

These expressions for the drift vector 3.62 and diffusion matrix 3.63 are simpler to treat if the initial velocity of the particle before a collision is aligned with one axis of the local frame chosen to perform the collision (in velocity space). Thus, we use the frame  $(x', y', z')$ , shown in figure 3.11, in which the velocity  $w$  of the heavy impurity particle before a collision is aligned

### 3.2. VENUS-LEVIS for tracing heavy impurity guiding centers in the presence of strong flows and 3D geometry



(a)

Figure 3.11 – Frame  $(x', y', z')$  in which the velocity of the particle before collision is aligned with the  $z'$  axis.

with the  $z'$  axis. After the collision, the velocity in this direction will change and there will be a variation of the velocity in the  $x'$  and  $y'$  directions. However, VENUS-LEVIS only has information about the parallel velocity  $w_{\parallel}$  and the magnitude of the perpendicular velocity  $w_{\perp}$  of the particle. To map the final velocity variations back in the in this magnetic-field-aligned velocity coordinates we need to define for each particle undergoing a collision, which is their initial velocity components along each of the perpendicular (relative to the magnetic field) directions, the directions  $\nabla\psi$  and  $\hat{b} \times \nabla\psi$ . We only know the parallel velocity and the strength of the perpendicular velocity when in the guiding center formalism, and we do not follow the gyroangle coordinate. We thus, for each collision, generate a random uniform gyroangle  $\phi_w$  between  $[0, 2\pi]$ . The angle  $\theta_w$  (see figure 3.11) between the initial parallel velocity  $w_{\parallel}$  and the total velocity vector  $w$  is defined before the collision as

$$\theta_w = \cos^{-1} \left( \frac{w_{\parallel}}{w} \right), \quad (3.64)$$

the perpendicular velocity magnitude in the  $\nabla\psi$  and  $\hat{b} \times \nabla\psi$  directions are respectively

$$w_{\perp 1} = w \sin(\theta_w) \cos(\phi_w). \quad (3.65)$$

$$w_{\perp 2} = w \sin(\theta_w) \sin(\phi_w). \quad (3.66)$$

In the frame  $(x', y', z')$  the drift vector components are

$$\mathcal{A}_{x'}^{WI} = 0 \quad (3.67)$$

$$\mathcal{A}_{y'}^{WI} = -w_{\perp} U_{back\parallel} \beta \left( \frac{\zeta(w_b) + w_b \zeta'(w_b)}{w_b^4} \right) + \frac{4w_{\perp} q_{I\parallel}}{5m_I N_I} \beta^2 \frac{\zeta'(w_b)}{w_b} \quad (3.68)$$

$$\mathcal{A}_{z'}^{WI} = w_{\perp} U_{back\parallel} \beta \left( \frac{-\zeta(w_b) + (2w_b + 2w_b^3) \zeta'(w_b)}{x^4} \right) + \frac{4w_{\perp} q_{I\parallel}}{5m_I N_I} \beta^2 \frac{(2w_b^2 - 1) \zeta'(w_b)}{w_b} \quad (3.69)$$

and diffusion matrix entries can be written as

$$\mathcal{D}_{x'y'}^{WI} = \begin{pmatrix} \mathcal{D}_{y'y'}^{WI} & 0 & 0 \\ 0 & \mathcal{D}_{y'y'}^{WI} & \mathcal{D}_{y'z'}^{WI} \\ 0 & \mathcal{D}_{z'y'}^{WI} & \mathcal{D}_{z'z'}^{WI} \end{pmatrix} \quad (3.70)$$

with

$$\mathcal{D}_{y'y'}^{WI} = \frac{(2w_b^5 - 1) \zeta(w_b) + w_b \zeta'(w_b)}{2w_b^3} + w_{\parallel} U_{back\parallel} \beta \left( \frac{(2w_b^3 - 3) \zeta(w_b) + 3w_b \zeta'(w_b)}{2w_b^5} \right) \quad (3.71)$$

$$+ \frac{4w_{\parallel} q_{I\parallel}}{5m_I N_I} \beta^2 \left( \frac{-6\zeta(w_b) + (4w_b^3 + 6w_b) \zeta'(w_b)}{2w_b^5} \right) \quad (3.72)$$

$$\mathcal{D}_{y'z'}^{WI} = -w_{\perp} U_{back\parallel} \beta \left( \frac{(2w_b^2 - 3) \zeta(w_b) + 3w_b \zeta'(w_b)}{2w_b^5} \right) + \frac{4w_{\perp} q_{I\parallel}}{5m_I N_I} \beta^2 \left( \frac{3\zeta(w_b) - (2w_b^2 + 3) \zeta'(w_b)}{2w_b^5} \right) \quad (3.73)$$

$$\begin{aligned} \mathcal{D}_{z'z'}^{WI} &= \frac{\zeta(w_b) - w_b \zeta'(w_b)}{x^3} - w_{\parallel} U_{back\parallel} \beta \left( \frac{3\zeta(w_b) - (2w_b^3 + 3w_b) \zeta'(w_b)}{w_b^5} \right) \\ &+ \frac{4w_{\parallel} q_{I\parallel}}{5m_I N_I} \beta^2 \left( \frac{3\zeta(w_b) - (2w_b^5 + 2w_b^3 + 3w_b) \zeta'(w_b)}{2w_b^5} \right). \end{aligned} \quad (3.74)$$

Since this matrix is not diagonal, the matrix  $\sigma_{ij}^{WI}$  is not directly obtainable. One must first diagonalize the matrix  $\mathcal{D}_{xy}^{WI}$ . We thus have  $\sigma_{ij}^{WI} = \mathcal{P} \mathcal{V} \mathcal{P}^T$  in which

$$\mathcal{V}_{ij} = \begin{pmatrix} \sqrt{\mathcal{D}_{y'y'}^{WI}} & 0 & 0 \\ 0 & \sqrt{\lambda_+} & 0 \\ 0 & 0 & \sqrt{\lambda_-} \end{pmatrix} \quad (3.75)$$

### 3.2. VENUS-LEVIS for tracing heavy impurity guiding centers in the presence of strong flows and 3D geometry

and the proper values of the matrix  $\mathcal{D}_{ij}^{WI}$  are defined as

$$\lambda_1 = \mathcal{D}_{y'y'}^{WI} \quad (3.76)$$

$$\lambda_2 = \lambda_+ = \frac{\mathcal{D}_{y'y'}^{WI} + \mathcal{D}_{z'z'}^{WI} + \sqrt{(\mathcal{D}_{y'y'}^{WI} - \mathcal{D}_{z'z'}^{WI})^2 + 4\mathcal{D}_{y'z'}^{WI^2}}}{2} \quad (3.77)$$

$$\lambda_3 = \lambda_- = \frac{\mathcal{D}_{y'y'}^{WI} + \mathcal{D}_{z'z'}^{WI} + \sqrt{(\mathcal{D}_{y'y'}^{WI} - \mathcal{D}_{z'z'}^{WI})^2 + 4\mathcal{D}_{y'z'}^{WI^2}}}{2} \quad (3.78)$$

and the orthogonal matrix  $P_{ij}$  of the proper vectors of  $\mathcal{D}_{ij}^{WI}$  is

$$\mathcal{V}_{ij} = \begin{pmatrix} 1 & 0 & 0 \\ 0 & \frac{\mathcal{D}_{y'z'}^{WI}}{\sqrt{(\lambda_+ - \mathcal{D}_{y'y'}^{WI})^2 + \mathcal{D}_{y'z'}^{WI^2}}} & \frac{\mathcal{D}_{y'z'}^{WI} - \lambda_+}{\sqrt{(\lambda_+ - \mathcal{D}_{y'y'}^{WI})^2 + \mathcal{D}_{y'z'}^{WI^2}}} \\ 0 & \frac{\lambda_+ - \mathcal{D}_{y'z'}^{WI}}{\sqrt{(\lambda_+ - \mathcal{D}_{y'y'}^{WI})^2 + \mathcal{D}_{y'z'}^{WI^2}}} & \frac{\mathcal{D}_{y'z'}^{WI}}{\sqrt{(\lambda_+ - \mathcal{D}_{y'y'}^{WI})^2 + \mathcal{D}_{y'z'}^{WI^2}}} \end{pmatrix} \quad (3.79)$$

Finally, the velocity variation due to collisions in the  $(x', y', z')$  coordinates is given by

$$d\mathbf{w}_{coll_x} = \mathcal{A}_{x'}^{WI} dt + \sigma_{x'x'}^{WI} dW_{x'} \quad (3.80)$$

$$d\mathbf{w}_{coll_y} = \mathcal{A}_{y'}^{WI} dt + \sigma_{y'y'}^{WI} dW_{y'} \quad (3.81)$$

$$d\mathbf{w}_{coll_z} = \mathcal{A}_{z'}^{WI} dt + \sigma_{z'z'}^{WI} dW_{z'} \quad (3.82)$$

with  $dW_i$  independent random numbers sampled from a gaussian of zero mean and variance  $\sqrt{dt}$  and a fixed timestep is used. The velocity variations due to the collisions in the magnetic field aligned coordinate system are then obtain by

$$d\mathbf{w}_{\perp 1} = \cos(\phi_w) d\mathbf{w}_{coll_x} - \sin(\phi_w) \cos(\theta_w) d\mathbf{w}_{coll_y} + \sin(\phi_w) \sin(\theta_w) d\mathbf{w}_{coll_z}, \quad (3.83)$$

$$d\mathbf{w}_{\perp 2} = \sin(\phi_w) d\mathbf{w}_{coll_x} + \cos(\phi_w) \cos(\theta_w) d\mathbf{w}_{coll_y} - \cos(\phi_w) \sin(\theta_w) d\mathbf{w}_{coll_z}, \quad (3.84)$$

$$d\mathbf{w}_{\parallel} = \sin(\theta_w) d\mathbf{w}_{coll_y} + \cos(\theta_w) d\mathbf{w}_{coll_z}. \quad (3.85)$$

These velocity variations correctly account for both the effects of a friction force and thermal force acting on the minority species, due to collisions with a background species with both a flow and heat flux. The previous collision operator implemented in VENUS-LEVIS only took into account collisions with a background species  $s$ , for which the distribution function was a Maxwellian with a possible mean flow ((55), (56)). Such, collision operator did not capture any thermal force effect and accounted only in part for the effect of a friction force. The effect of the thermal force can be seen in figure 3.12 for an axisymmetric simulation with no density gradient and a finite temperature gradient. We can see the particles being transported

radially outward due to the effect of the thermal screening. The asymmetries due to collisional effects can also be seen which cause an up-down asymmetry usual of collisional neoclassical transport. The collision operator just described and the guiding center equations with strong flow corrections should thus contain all the physics to study neoclassical transport of heavy impurities. Next chapter, will make use of the numerical tools described in the present chapter, to properly model heavy impurity transport in the presence of a 1/1 internal kink mode of interest in tokamak operation (see section 1.7)

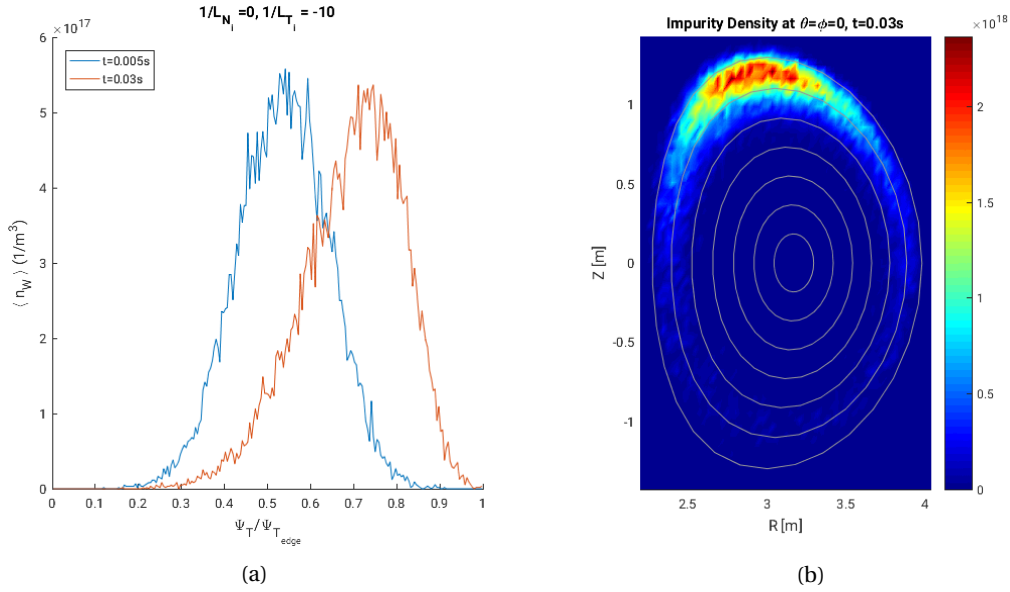


Figure 3.12 – Effects of the thermal force due to heat flux of the background ions for an axisymmetric equilibrium with only a ion temperature gradient. Such effects are only possible due to the newly implemented collision operator. (a) The thermal force pushes the tungsten out screening it from the core as expected. (b) Up-down poloidal asymmetries are generated due to the collisional forces.

### 3.2.3 Conclusion

In this chapter, we presented the numerical tools developed to model heavy impurity transport in tokamaks with 3D MHD ideal perturbations, strong rotation and ambipolar electric field. The way the VMEC code is used to obtain the 3D magnetic equilibrium of interest was explored. It was then shown how we use such magnetic equilibria to obtain the corresponding background ion flow and heat flux, as well as the heavy impurity flow. Then, it was shown how we make use of all these quantities in the VENUS-LEVIS code used to construct the population of heavy impurities. We explained how we use this code to calculate the guiding-center equations for the heavy impurities. The implementation was shown to capture all the relevant drifts for heavy impurity physics, such as the centrifugal and Coriolis drifts. Finally, a new collision operator implementation was presented. This collision operator captures the friction

### 3.2. VENUS-LEVIS for tracing heavy impurity guiding centers in the presence of strong flows and 3D geometry

---

and the thermal forces felt by impurities when colliding with the background ions (which were not correctly captured in the previous implementation). The background ion flow, heat flux, and the impurity flow are crucial elements of the collision operator. Following the impurities in the frame rotating with the common flow  $\mathbf{U}_{1/4}$  and the impurity flow  $\mathbf{U}_{W_1}$  is crucial for capturing the effect of the ambipolar electric field on the collision operator. The calculation of such flows and heat flux was made possible by the development of the auxiliary codes. The numerical tools described and presented in this chapter are therefore suitable for the study of heavy impurity transport in the presence of 3D MHD ideal perturbations, strong flows and ambipolar electric field, and will be used to study the particular and important case of the 1/1 internal kink mode in the next chapter.





## 4 The effect of 3D MHD ideal perturbations on Heavy impurity transport

This chapter presents numerical results obtained from simulating the behaviour of strongly rotating tungsten in the presence of a  $1/1$  internal kink plasma and ambipolar electric field. To accomplish this, we make use of the numerical tools presented in chapter 3. First, we analyse the behaviour of the flux averaged neoclassically resolved flow of the background ions in a  $1/1$  internal kink. This interesting novel flow components presented affects impurity transport in the kinked region of the plasma. It is seen that inconsistent modelling of flows and in particular the flow associated with the ambipolar electric field, has a crucial impact on impurity transport. This is shown by breaking down the physics of interest when solving for the saturated impurity density states obtained from VENUS-LEVIS simulations. We first analyse the behaviour of heavy impurities for the axisymmetric case presented in figure 3.5. Then we analyse the effect that the  $1/1$  internal kink mode equilibrium has on tungsten transport in the presence of other physical mechanisms like strong rotation and ambipolar electric field. To do this analysis we use the  $1/1$  internal kink shown in figure 3.7, which models the strong 3D phase of JET pulse #92181. We then analyse the transitory phase of the VENUS-LEVIS simulations, before the tungsten density saturates. This analysis allows for a calculation of the tungsten diffusion coefficients under the effect of different physical mechanisms of interest. We then, analyse how the change of amplitude of the kink perturbation impacts the tungsten density. Finally, we allow the ambipolar electric field to be positive in the kink region (electron root) in order to mimic the effect of electron cyclotron heated (heated with ECRH)  $1/1$  internally kinked plasmas on heavy impurity transport. This model allows for gaining some insight on the physics seen during certain interesting operational scenarios on ASDEX-U (53). In order, to make a comparison against the analytical results presented in chapter 2, we present here again the impurity friction force

$$\begin{aligned}
\frac{R_{W\parallel}}{v_{IW} N_I m_I} = & - \left[ w - \frac{\langle w B^2 \rangle}{n_W \langle \frac{B^2}{n_W} \rangle} \right] \frac{T_I}{q_W N_W} \frac{\partial N_W}{\partial \psi} B \\
& - \left[ w - \frac{\langle w B^2 \rangle}{n_W \langle \frac{B^2}{n_W} \rangle} - \left( \frac{1}{\langle B^2 \rangle} - \frac{1}{n_W \langle \frac{B^2}{n_W} \rangle} \right) (f_s + \langle u B^2 \rangle) \left( \frac{f_c}{f_t} + 1 \right) \right] \frac{\partial \Phi_0}{\partial \psi} B \\
& - \left[ \frac{w R^2}{\langle R^2 \rangle} - \frac{\langle w R^2 B^2 \rangle}{n_W \langle R^2 \rangle \langle \frac{B^2}{n_W} \rangle} \right] \frac{m_W \Omega \langle R^2 \rangle}{q_W} \frac{\partial \Omega}{\partial \psi} B \\
& + \left[ u - \frac{\langle u B^2 \rangle}{\langle B^2 \rangle} + \left( \frac{1}{\langle B^2 \rangle} - \frac{1}{n_W \langle \frac{B^2}{n_W} \rangle} \right) (f_s + \langle u B^2 \rangle) \left( \frac{f_c}{f_t} + 1 \right) \right] \frac{T_I}{q_I N_{I_0}} \frac{\partial N_{I_0}}{\partial \psi} B \\
& - \left[ \frac{3}{2} u - \frac{3}{2} \frac{\langle u B^2 \rangle}{\langle B^2 \rangle} + \left( \frac{1}{\langle B^2 \rangle} - \frac{1}{n_W \langle \frac{B^2}{n_W} \rangle} \right) (f_s + \langle u B^2 \rangle) \left( 1.17 \frac{f_c}{f_t} + \frac{3}{2} \right) \right] \frac{T_I}{q_I T_I} \frac{\partial T_I}{\partial \psi} B \quad (4.1)
\end{aligned}$$

for which the terms which will be important for the discussions in this chapter are highlighted with different colours.

#### 4.1 The background ion flow

The geometrical factors obtained numerically for VMEC equilibrium configurations (see section 3.1.5) can be used to calculate both the background ion flow and heat flux. Here, we analyse the differences between the flux averaged parallel bulk ion diamagnetic flow obtained for the axisymmetric equilibrium in figure 3.5 and the 1/1 internal kink equilibrium in figure 3.7. This particular part of the diamagnetic flow is quite interesting as it impacts heavy impurity transport only when heavy impurity density asymmetries are present. We may observe, from equation 2.86, that the averaged parallel diamagnetic flow is proportional to both the geometrical factor  $f_s + \langle u B^2 \rangle$ , and the background ion density and temperature gradients. Thus, its effect is associated with the terms in **orange** in the impurity ion friction force 4.1, which vanishes when no impurity asymmetries are present in a flux surface ( $n_W = \langle n_W \rangle$ , and thus  $\left( \frac{1}{\langle B^2 \rangle} - \frac{1}{n_W \langle \frac{B^2}{n_W} \rangle} \right) = 0$ ). This means that for the case studied here, that when no externally generated strong glows (due to NBI) are present in the plasma, this component of the diamagnetic flow has no effect on the transport of tungsten. The effect of this flow on impurity collisional transport may also change drastically for different 3D perturbations, because the geometrical functions  $u$  and  $f_s$  depend mainly on the geometry of the magnetic configuration. Moreover, this effect exists even when no ambipolar electric field is considered, and can therefore be used to understand if the VENUS-LEVIS code implementation is capturing the correct effects in such case.

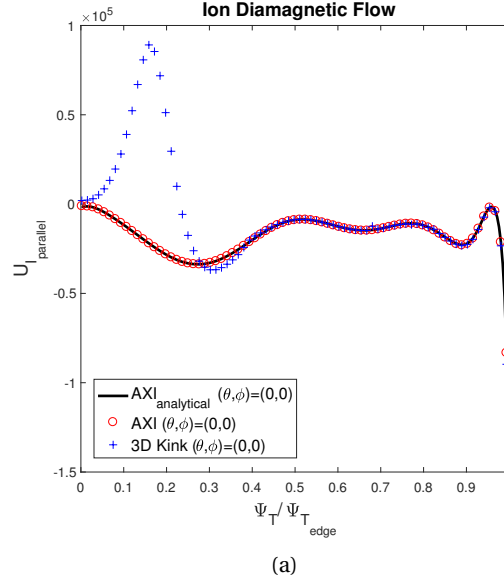


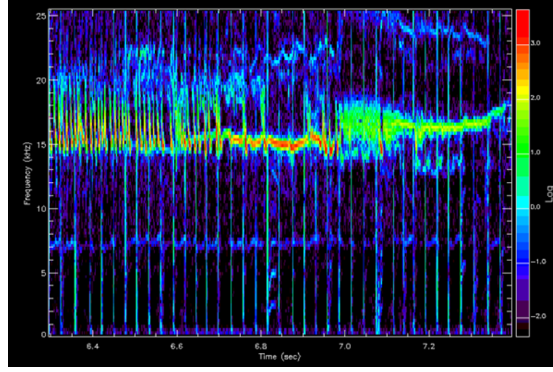
Figure 4.1 – Background ion mean diamagnetic parallel flow obtained numerically for the axisymmetric case in figure 3.5 and for the 1/1 internal kink in figure 3.7. The flow for the axisymmetric equilibrium agrees well with the analytical solution (black line).

In figure 4.1, the analytically known flux averaged parallel bulk ion diamagnetic flow for the axisymmetric case is compared against the numerical calculation. Both profiles are in perfect agreement as expected. The numerical flux averaged parallel bulk ion diamagnetic flow for the axisymmetric and 3D cases are also compared in figure 4.1. We see that outside the region of influence of the 1/1 internal kink the flows are identical due to the fact that the equilibrium outside the kinked core region is essentially axisymmetric. However, we also see that in the kinked region, an inversion of the sign of the flow is observed, which is expected as the geometrical factor  $f_s + \langle uB^2 \rangle$  was seen to invert its sign in the kinked region (see figure 3.10 of section 3.1.5). In the axisymmetric case, these terms produce inward and outward transport of impurities for a density and a temperature gradient respectively. However, the inversion of sign of the averaged parallel bulk ion diamagnetic flow in the region of the kink can cause a density gradient to instead provide a screening of impurities from the axis, while a temperature gradient can cause inward transport of impurities. The same type of effect can be seen for the flux averaged ion background ion heat flux which is also proportional to the factor  $f_s + \langle uB^2 \rangle$  and the background ion temperature gradient.

## 4.2 Axisymmetry with strong flows

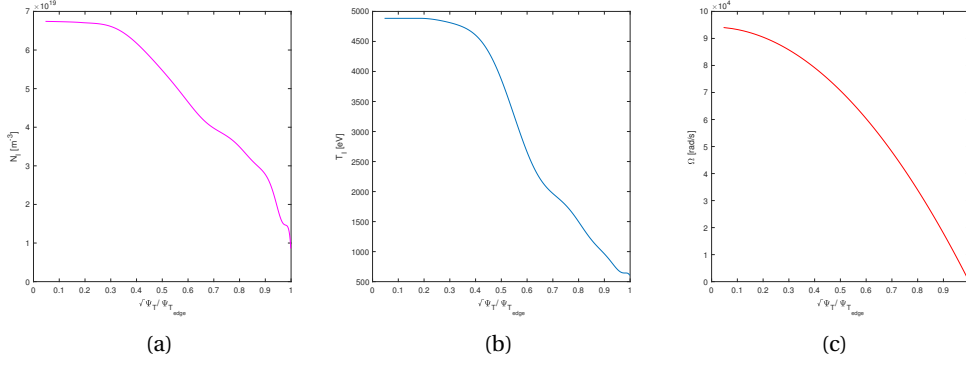
In this thesis, we want to understand the effect that a 1/1 long living internal kink mode like the one present in JET-pulse #92181 (see figures 3.2 and 3.3) can have on heavy impurity transport. We are thus interested in comparing the weakly 3D phase of figure 3.3a (in which

the plasma is mostly axisymmetric) and the strong 3D phase of figure 3.3b. Thus, we model the behaviour of tungsten in the presence of the axisymmetric VMEC equilibrium shown in figure 3.7 and the 1/1 internal kink VMEC equilibrium in figure 3.7. As stated before (see section 3.1.3), these two equilibria are obtained using exactly the same pressure and safety factor profiles except that the axisymmetric one is constrained to have no 3D perturbations (we impose a toroidal mode number  $n = 0$  only). These equilibria can be used as an input in VENUS-LEVIS to follow the tungsten particles, together with the background ion flow  $U_{I_1}$  and heat flux  $q_{I_1}$ , and the impurity flow  $U_{W_1}$ . The electric field  $E_{-3/4}$  necessary for the calculation of the impurity flow  $U_{W_1}$  (see section 3.1.5) is established from the experimental measurement of the NBI induced toroidal rotation (see eq. 2.82) which is also important for the centrifugal forces entering the guiding center equations 3.43 and 3.44. The core rotation due to NBI can be identified correctly from the frequency of the  $n = 1$  mode. Such information can be obtained from the MHD coil spectrogram from JET pulse #92181 which can be seen in figure 4.2. We see that the  $n = 1$  mode has a rotation of approximately  $f_{mode} = 15\text{KHz}$  throughout the pulse. We consider the NBI generated rotation profile to be given by  $\Omega(s_V) = 2\pi f_{mode}(1 - s_V)$ , which is similar to the one observed in the pulse #92181 (see definition of  $s_V$  below). The higher order electric field profile  $\Phi'_0(\psi)$  is also needed. This profile can in general be affected by the existence of strong additional sources of toroidal momentum like ECRH. For the JET related simulations presented here, we neglect the effect of strong sources and consider that the profile  $\Phi'_0(\psi)$  is due to NTV, obtained from the temperature and pressure profiles through equation 2.113. The rotation profile as well as the background ion density and temperature profiles can be seen in figure 4.3. The background ion temperature and density were obtained from equilibrium reconstruction from JET pulse #92181, according to the background ion pressure profiles used in VMEC and shown in figure 3.4. We choose to plot these quantities against the radial coordinate  $\sqrt{s_V} = \sqrt{\Psi_T/\psi_{T_{edge}}} = r/a$ , with  $r$  being the minor radius of the tokamak and  $a$  its value at the last closed flux surface. All the simulations in this chapter use a number of markers  $N_{markers} = 30720$  to simulate the tungsten particles. A larger number of markers has not seen to changed the saturated impurity density states. Furthermore, the tungsten particles simulated have a ionization state with  $Z_W = 40$  and a mass number of 184.



(a)

Figure 4.2 – MHD coils spectrogram for JET pulse #92181. A mode frequency of  $f_{mode} = 15\text{KHz}$  for the  $n = 1$  mode is observed.



(a)

(b)

(c)

Figure 4.3 – Background ion density  $N_I$  and temperature  $T_I$ , and toroidal rotation used for the simulations of JET pulse #92181.

We consider first the axisymmetric equilibrium where we present two simulations with and without rotation (see fig. 4.4a). In the axisymmetric case we do not consider the ambipolar electric field (from NTV) as a parameter since it can be seen from equation 2.148 that the effect of the electric field associated with  $\Phi_0$  vanishes in the axisymmetric limit. We present in figure 4.4a the flux averaged saturated tungsten density in the axisymmetric case, with rotation (red line) and without rotation (black line). The impurity density is considered saturated if it does not change significantly after the characteristic time of cross field transport, which is of the order of 0.1s. In the axisymmetric case without rotation (described by the black line in figure 4.4a), the profile peaks on the axis ( $s_V \approx 0$ ) which means that impurities accumulate on-axis for the axisymmetric case without rotation. This is due to the fact that the friction effect due to the density gradient of the bulk ions overcomes the thermal screening due to the bulk ion temperature gradient (see blue terms in the friction force 4.1) for pulse #92181 (see figures 4.3a and 4.3b). The red line in figure 4.4a corresponds to the axisymmetric case with the rotation profile of figure 4.3c. In this case, the rotation is strong enough to drive outward

transport due to a radial centrifugal force (see **red** term in equation 4.1). This means that if no 3D effects are considered, axisymmetric theory dictates off-axis impurity density peaking for background temperature, density and rotation profiles similar to the ones of the pulse #92181. This is indeed the case in the early phase of #92181 where the plasma is 2D (see figures 3.2 and 3.3a). A better comparison with the experimental SXR tomography 3.3a is made via the poloidal contour plot shown in figure 4.4a. Here, we see the accumulation off-axis which is due to the strong radial centrifugal force as well as the poloidal trapping of impurities due to the poloidal centrifugal force. Figure 4.4b compares reasonably well with the experimental SXR tomography in figure 3.3a.

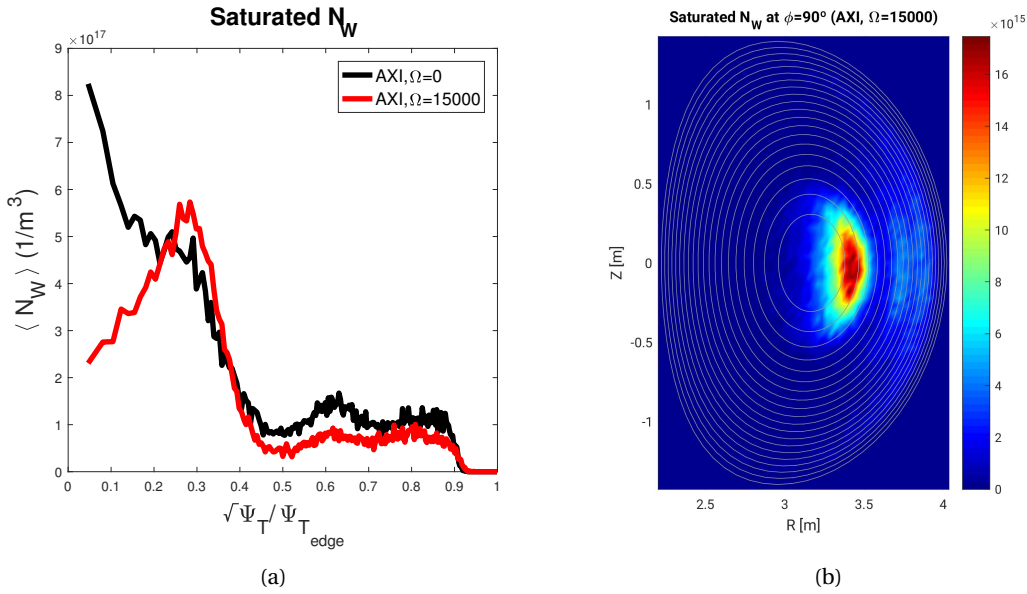


Figure 4.4 – Saturated flux averaged radial profiles of the heavy impurity density obtained with VENUS-LEVIS showing the effect of rotation in axisymmetry.

### 4.3 Synergetic effect of the 1/1 internal kink mode with rotation on heavy impurity transport

We consider now how the 1/1 internal kink long living mode like the one in the pulse #92181 affects heavy impurity transport. First, the effect of the NTV electric field is neglected. While this case is inconsistent, it allows to isolate the effect of the flux averaged diamagnetic flow and heat flux, which was discussed in section 4.1. Figure 4.5 presents the flux averaged tungsten density for various simulations, which helps in understanding the effect of this 3D diamagnetic flow, while changing the main NBI induced toroidal rotation.

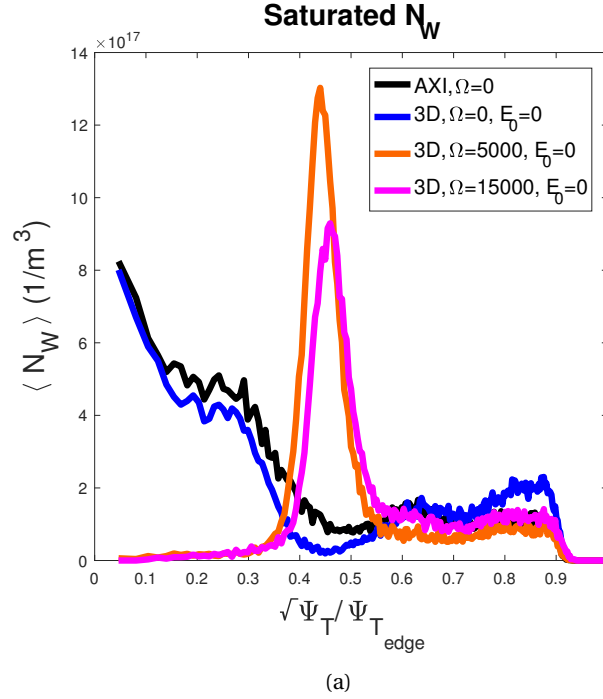


Figure 4.5 – Saturated flux averaged radial profiles of the heavy impurity density obtained with VENUS-LEVIS showing the effect of the 1/1 internal kink mode on heavy impurity transport, while changing the rotation. The NTV electric field is not included in these simulations. The off-axis accumulation observed for finite rotation is due to the background ion parallel diamagnetic mean flow (see figure 4.1) and heat flux.

The blue line in figure 4.5 is obtained in the presence of an equilibrium with a 1/1 internal kink, but we do not include any rotation. We may see that for this case impurities accumulate on-axis. This is a consequence of having zero strong rotation and thus no poloidal asymmetries of the impurity density in the system. The effect of the bulk ion parallel diamagnetic mean flow on heavy impurity transport vanishes in this limit, as was discussed in section 4.1 (see orange terms in equation 4.1), and can be observed in equations 2.140-2.144. Since the NTV electric field is also neglected the transport is only driven by balance between the bulk ion density and temperature gradients (blue terms in equation 4.1) which is the same as for the axisymmetric case without rotation (black line) of figure 4.5. This is because, in the absence of density asymmetries (see 2.140-2.144), the diffusion coefficients associated with the density and temperature gradients have the same dependence on the geometrical functions  $u$  and  $w$  for both axisymmetric and 3D cases. Therefore, the result for this case (blue line) is similar for the 2D case without rotation (black line of figure 4.5).

The orange line in figure 4.5 considers finite rotation with the 1/1 internal kink equilibrium. A rotation profile with  $f_{mode} = 5kHz$  is chosen, which is a moderate level of rotation, and thus, it is not strong enough to drive outward transport due to the radial centrifugal force. Nevertheless, off-axis accumulation is still observed for the orange line in figure 4.5a. The

cause is the bulk ion diamagnetic mean parallel flow, whose effect arises for finite poloidal asymmetries of the impurity density. While the smaller rotation does not provide a strong radial force, it still provides a poloidal centrifugal force which causes enhanced trapping of impurities. The poloidal asymmetry of the density activates the effect of the diamagnetic mean flow in the collisional force felt by the impurities (see **orange** terms in equation 4.1). As seen in figure 4.1, the background ion mean parallel flow inverts its sign in the 1/1 internal kink region, when compared to the axisymmetric case. The same happens to the background ion mean parallel heat flux. As a consequence, bulk ion density gradient now screens the impurities from the core and the bulk ion temperature gradient pushes the impurities to the core, contrary to what usually happens in axisymmetry. Since the density gradient wins over the temperature gradient for the profiles in figure 4.3, we observe off-axis accumulation. Finally, the magenta line of figure 4.5 is a 3D case with the same rotation amplitude as the one observed experimentally (with  $f_{mode} = 15kHz$ ). A slightly stronger outward flux of impurities is observed for this case in comparison with the previous case (orange line). The stronger rotation provides now a strong radial force as in the axisymmetric case (red line of figure 4.5a), which further pushes the impurities radially outward when compared to the orange line. These cases are however not consistent, because no ambipolar electric field was considered. We include the NTV electric field effect in the next section.

### 4.4 Synergetic effect of the 1/1 internal kink mode, rotation and NTV electric field on heavy impurity transport

The effect of the NTV electric field is now included in order to model the rotating 3D case consistently. We compare this 3D consistent case with the axisymmetric case with rotation in figure 4.6. The green line in 4.6 includes the effect of the 1/1 internal kink equilibrium, a strong rotation with  $f_{mode} = 15kHz$  and the finite effect of the ambipolar electric field due to bulk ion NTV. The effect of the NTV electric field in the presence of the strong flow asymmetries (see **green** term in equation 4.1) is enough to drive strong on-axis accumulation as we see from the green line in figure 4.6. The green case is therefore very important as it shows that with all the effects of interest considered for the 3D case we observe on-axis impurity accumulation, in contrast with the axisymmetric case shown by the red line in figure 4.6. This accumulation is consistent with the experiment, in the phase of discharge #92181 during which the rotating 3D 1/1 kink has developed (see figure 3.3b). It is noted here that we kept the density, temperature and rotation profiles constant when comparing the 2D and 3D phases of the experiment. This is necessary to identify the role of 3D physics effects, at the cost of detailed modelling of the experiment at different times in the pulse. Although, the density and rotation do not change much between the two phases according to experiment (see figures 3.2 and 4.2), the temperature changes slightly between these two phases of the pulse (see figure 3.2). The reason for the small change in the profiles is due to the fact that the different MHD phases of the operations are short. The neglect of the change in the temperature profiles will be justified in section 4.6 by analysing the transport coefficients. It will be seen that the transport in the



#### 4.4. Synergetic effect of the 1/1 internal kink mode, rotation and NTV electric field on heavy impurity transport

presence of 3D effects, strong flow and ambipolar electric field is fast enough to explain the transport timescales observed empirically.

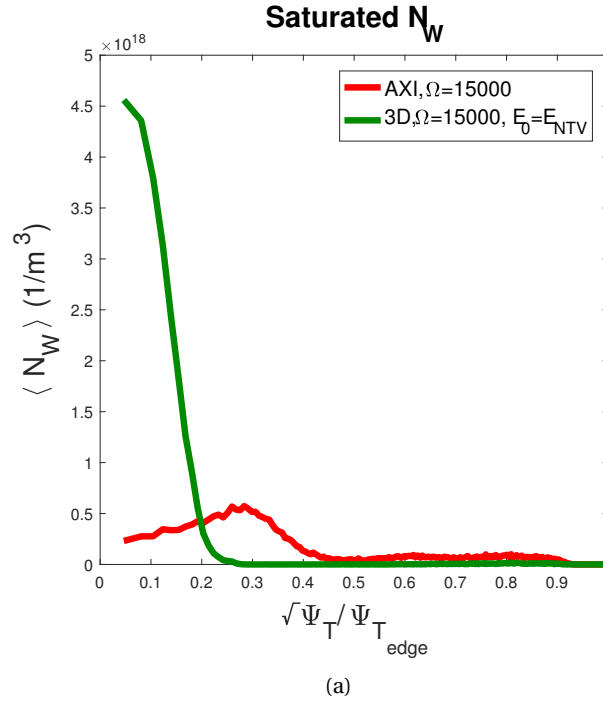


Figure 4.6 – Saturated flux averaged radial profiles of the heavy impurity density obtained with VENUS-LEVIS showing the synergetic effect of the 1/1 internal kink mode and strong rotation on heavy impurity transport. The NTV electric field is enough to drive strong accumulation on-axis (green line), in contrast with the axisymmetric case with strong rotation (red line) which shows off-axis accumulation. The red curve is the same as the red curve in 4.4a.

The impurity density behaviour can be better compared to the experimental SXR tomography measurements by observing the poloidal contour plot of the impurity density (at toroidal angle of  $\phi = 90^\circ$ ) for the two cases shown in figure 4.6. Thus, in the same figure we show again the poloidal contour plot for the axisymmetric case with rotation 4.7b and the 1/1 internal kink mode with rotation and NTV electric field effects 4.7b. We see that for the 1/1 internal kink case in figure 4.7b the NTV induced electric field is enough to drive a radial inward transport that de-traps the impurities from the centrifugal trapping observed in the 2D case of figure 4.7a. The impurities then accumulate on-axis and follow the kink (as can be seen in figure 4.8). The results of figure 4.7 compare well with the SXR tomography for the weakly 3D 3.3a and strong 3D 3.3b phases of JET pulse #92181.

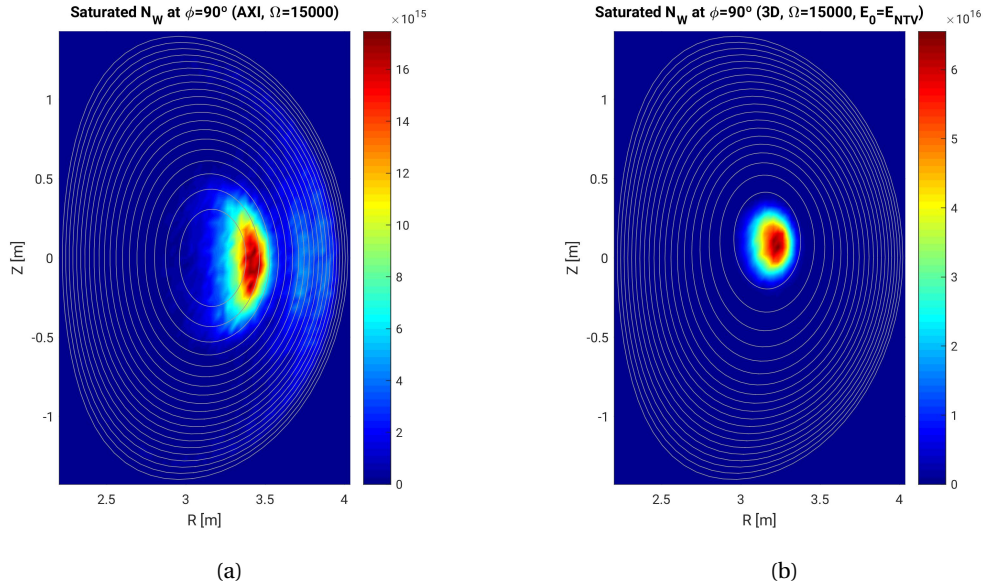


Figure 4.7 – Poloidal contour plot of the saturated heavy impurity density at a toroidal angle of  $\phi_V = 90^\circ$  obtained with VENUS-LEVIS. (a) Axisymmetric equilibrium. Models the initial phase of pulse #92181 (see fig. 3.3a). (b) Self consistent 3D case with rotation and NTV, which models the strongly 3D phase of JET pulse #92181 (see fig. 3.3b).

#### 4.5 Heavy impurity density hole in the presence of a 1/1 internal kink mode and ECRH

We now present a simulation of the 1/1 internal kink mode, with the same strong rotation ( $f_{mode} = 15\text{ KHz}$ ), but we use an ambipolar electric field  $E_0 = -E_{NTV}$ . This electric field is chosen to better understand the heavy impurity behaviour in the presence of a 1/1 internal kink mode, strong rotation and an ambipolarity electric field set by an electron root solution of the ambipolarity constraint 4.2. This ad-hoc model of the electric field can be used to gain insight into the operational scenarios in ASDEX-U in which a long living 1/1 internal kink is present at the same time as ECRH heating is applied. In these scenarios, the simultaneous presence of these two effects is seen to help screen tungsten (53). This screening of the tungsten ions is not explainable via a poloidal electric field correction due to quasi-neutrality, because the impurity density asymmetry seems to be mainly due to strong rotation (53). However, the presence of ECRH and the 1/1 mode could in principle create a strong electron flux, which would possibly change the solution of the ambipolarity constraint 4.2 to an electron root (72). Such a scenario places the hot electrons in the superbanana collisional regime. With the electrons in such a regime, the approximation of equation 2.112 is not valid. Indeed, in this case the flux of hot electrons is faster than the flux of ions because it is proportional to the electron-ion collision frequency. In the presence of ECRH the ambipolarity constraint is given

#### 4.5. Heavy impurity density hole in the presence of a 1/1 internal kink mode and ECRH

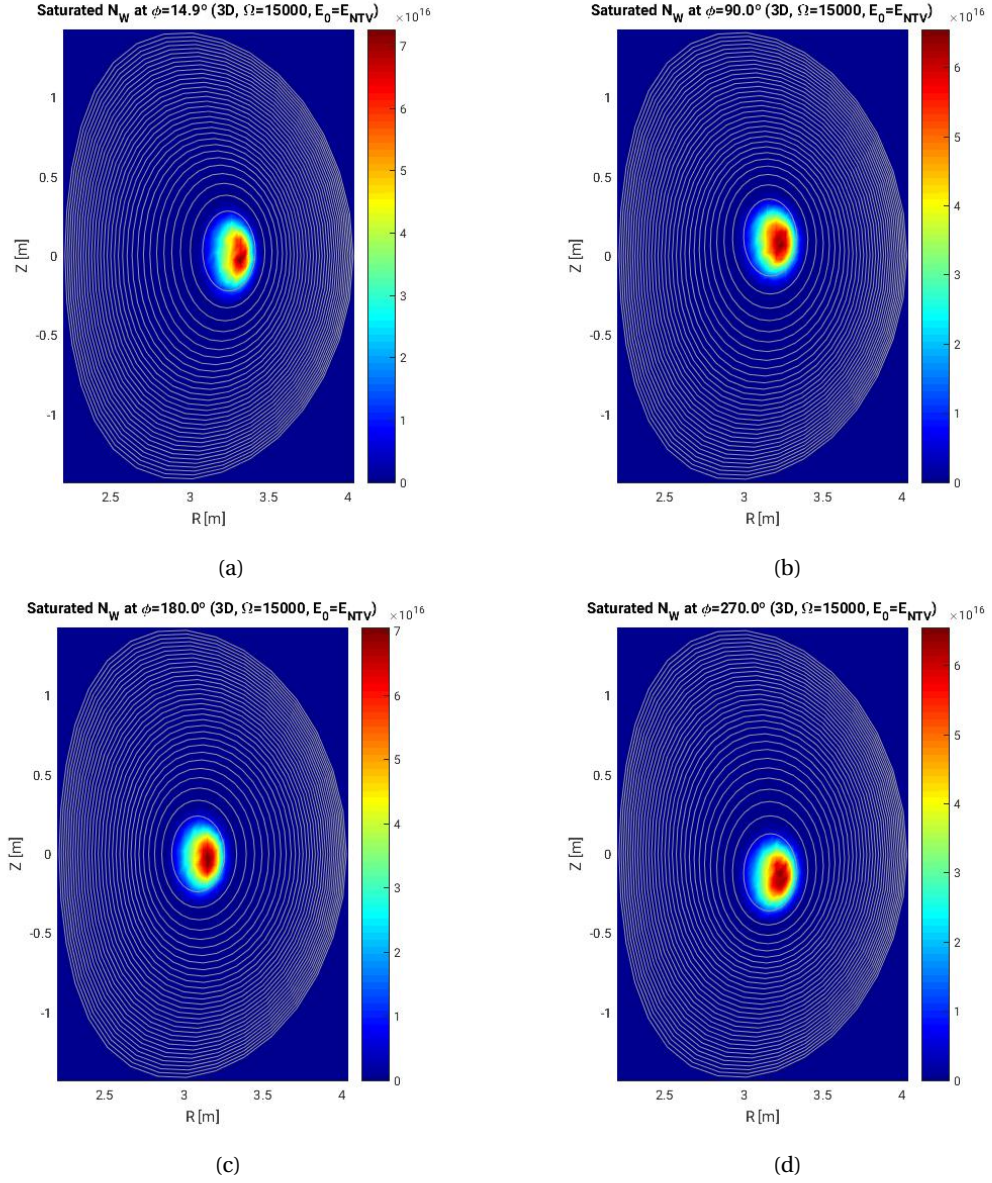


Figure 4.8 – Poloidal contour plot of the saturated heavy impurity density obtained with VENUS-LEVIS for the self-consistent 1/1 internal kink case with rotation and NTV. (a) At  $\theta_V = 11.4^\circ$ . (b) At  $\theta_V = 90.0^\circ$ . (c) At  $\theta_V = 180.0^\circ$ . (d) At  $\theta_V = 270.0^\circ$ .

by

$$q_e \langle \Gamma_{e_\psi} \rangle \approx 0, \quad (4.2)$$

which has a positive ambipolar electric field as a solution  $E_r > 0$  (72), usually called electron root. This is so because the fast radial movement of the hot electrons will generate a loss of electrons, which itself generates a charge separation. This charge separation is counteracted by the generation of a positive electric field. This electric field solution can be calculated via a neoclassical calculation. We currently do not have access to such a calculation (though there are some estimates in (72)). Nevertheless, by simply swapping the sign of the NTV electric field used in the last subsection, while maintaining the same amplitude, we hope to gain some insight into the possibility that the physics processes investigated in this thesis may explain the impurity behaviour observed in these ASDEX-U scenarios, in particular the effects of 3D, flows and ambipolar electric field. This is relevant when comparing to the work in (72), because in that work the focus was mainly on obtaining a estimate for the ambipolar electric field, while the impurity behaviour with such an estimate of the ambipolar electric field is not investigated in detail. The poloidal contour plots of the saturated tungsten density at different toroidal angles  $\phi_V$  can be seen in figure 4.9. We see that setting  $E_{ECRH} = -E_{NTV}$  is indeed capable of generating a screening of the impurities from the core, qualitatively consistent with the impurity density 'hole' observed in such ASDEX-U scenarios (53). In fact, in the kinked core region in which the effect of the ambipolar electric field is felt, the magnitude of the ad-hoc electric field  $E_{ECRH} = -E_{NTV}$  is smaller than the estimate found in (72). This indicates that even a small electric field will generate an impurity density 'hole'. The electron root effect is not considered in the remainder of this chapter because in the JET experiments we are primarily interested in modelling, ECRH is not available. However, the ECRH simulation is still shown here because the results could be relevant for future studies regarding ASDEX-U experiments and ITER scenarios in which ECRH will be available.

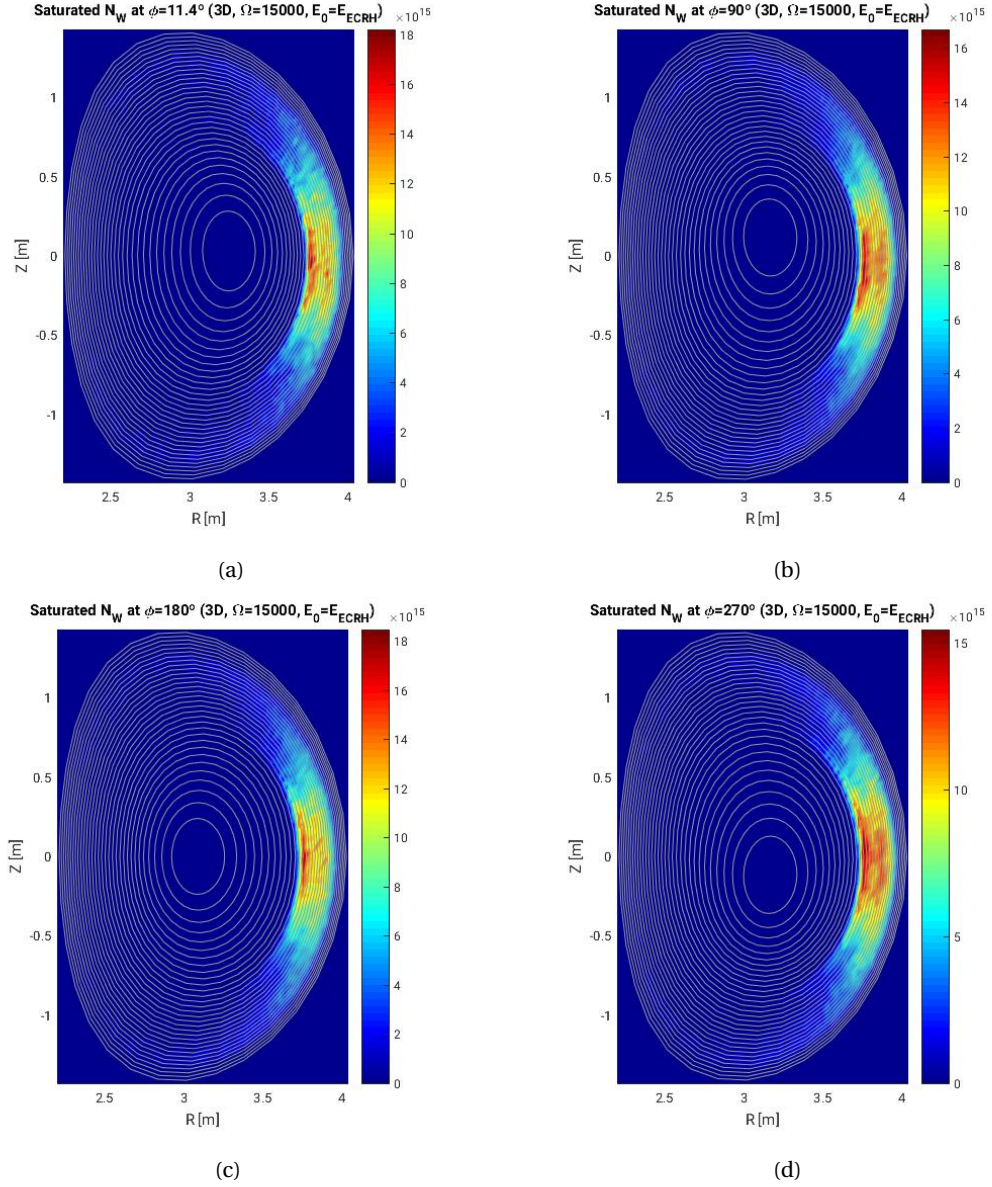


Figure 4.9 – Poloidal contour plot at of the saturated heavy impurity density for the 1/1 internal kink equilibrium of figure 3.7, the rotation profile of figure 4.3c, and an ambipolar electric field  $E_{ECRH} = -E_{NTV}$ . (a)  $\phi_V = 0^\circ$ . (b)  $\phi_V = 90^\circ$ . (c)  $\phi_V = 180^\circ$ . (d)  $\phi_V = 270^\circ$ .

## 4.6 Heavy impurity diffusion coefficients

The saturated heavy impurity density profiles are the most important results produced in our study into the effect of a 1/1 internal kink mode on heavy impurity transport. This is because they provide knowledge about the possible accumulation of heavy impurities on axis for different physics mechanisms. However, studying what happens in the transient phase between the initial impurity density configuration and the final saturated state is still of



interest as it may provide us with information about how fast the impurities accumulate in the presence of the different physics effects.

We may start by analysing the differences between parallel (relative to the magnetic field) and cross field impurity transport. In figure 4.10, we observe the poloidal contour plots showing the evolution of the heavy impurity density for the axisymmetric case with a rotation of  $f_{mode} = 15kHz$ . As stated in section 3.2.1, we have chosen to initialize the impurities at  $s = 0.9$ , localized around  $\theta = -\pi/2$  in order to model impurities that are being detached from a JET-like divertor configuration. This initial configuration can be seen in figure 4.10a. The impurities are transported rapidly along the field lines, and are trapped in the outboard region of the flux surface due to centrifugal effects. This configuration can be seen in 4.10b which represents the impurity density  $t = 0.04s$ . As expected we verify that parallel transport of impurities is faster than cross-field transport. Impurities are trapped poloidally before any cross-field transport is observed. In fact, we may observe that parallel transport due to the poloidal centrifugal force occurs at a time scale of around  $\tau_{\parallel} \sim 0.01 - 0.1s$ . In figure 4.10c we see the impurity density at  $t = 0.8s$ , at which time the impurities were already transported across the flux surfaces and have started to accumulate off-axis. From 4.10c we see that cross-field transport for axisymmetry occurs over a time scale of  $\tau_{\perp} \sim 0.1 - 1.0s$  for this axisymmetric rotating case.

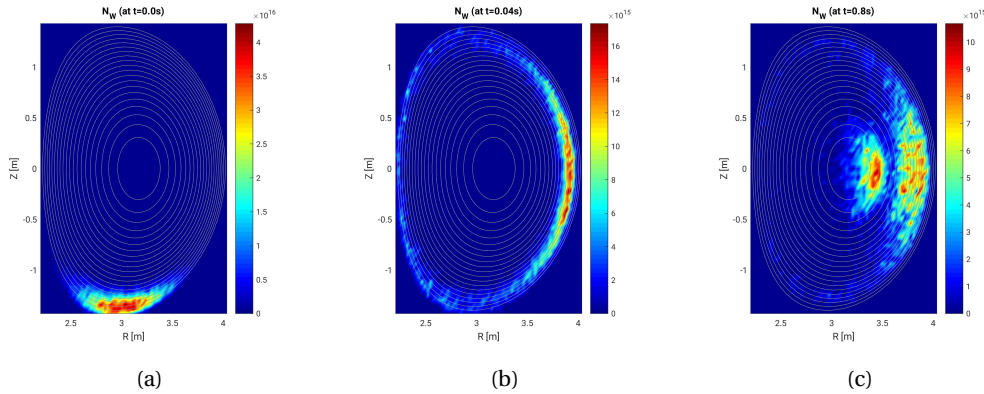


Figure 4.10 – Poloidal contour plot at  $\phi = 0$  of the heavy impurity density obtained with VENUS-LEVIS at different times for the axisymmetric case with a rotation  $\Omega_{max} = 15kHz$ . (a) At  $t = 0.0s$  (initial configuration). (b) At  $t = 0.04s$ . (c) At  $t = 0.8s$ .

A further analysis can now be undertaken to obtain the approximate time needed for the impurity density to saturate. This provides a numerical estimate of the cross-field diffusion coefficients in the presence of different physics mechanisms. To perform this study, we show in figure 4.11 the normalized flux averaged impurity density at different times for different mechanisms. The normalization factor  $\langle N_W \rangle_0$  is the maximum of the flux averaged impurity density profile for the initial configuration at  $t = 0.0s$  which also corresponds to the black line in figures 4.11a, 4.11b and 4.11c. In figure 4.11a we analyse the axisymmetric case without

rotation. From 2.151 and considering the plasma parameters of #92181 we obtain that the diffusion coefficient associated with the density gradients is  $D_{N_i}^{Neo} \sim 0.01 m^2/s$ . As we see from figure 4.11a the impurity density takes around 12s to reach the final state in which it accumulates on axis. Since it takes around 6s for the impurities to move across half the minor radius we obtain a numerical diffusion coefficient of  $D_{num}^{Neo} \approx 0.0726 m^2/s$  which is of the same order of magnitude as the analytical estimation. In the axisymmetric case with rotation of  $f_{max} = 15 kHz$ , which is presented in figure 4.11b, we see that in order to reach the final off-axis peak from a density peaking at  $(r/a)^2 = 0.9$  a time interval of around 1.8 – 2.0s is necessary. This implies that the diffusion coefficient for this case is  $D_{num}^{Neo} \approx 0.4737 m^2/s$ . This value is one order of magnitude larger than the axisymmetric case without rotation, which is expected because the rotation enhances heavy impurity cross-field transport.

The last case in figure 4.11c shows the 1/1 internal kink case with a rotation of  $f_{mode} = 15 kHz$ , and taking into account the self consistent effect of the NTV electric field. We observe that it takes around 1.2 – 1.4s for the impurities to saturate on axis from an initial density peaking at  $s = 0.9$ . Using this time interval an estimate for the diffusion coefficient including 3D effects would be  $D_{num}^{Neo} \approx 0.69 m^2/s$ . However, this time interval should not be used to obtain an estimate of the 3D modified transport diffusion coefficient, as in 4.11c all the impurities were initialised in the axisymmetric region. Thus, the transport is mainly unaffected by 3D effects until some of the particles start to reach the 3D core region around  $s = 0.4$ . In fact, in figure 4.11c we see that as the first impurities reach this area around  $t = 0.2s$ , they quickly start to strongly accumulate on axis (orange curve), whilst in the axisymmetric case (see orange curve of figure 4.11b) the impurities that reach this area are still not accumulating off-axis. A better estimate of the 3D modified diffusion coefficient can be obtained from figure 4.12). In this case the impurities are initialised around  $(r/a)^2 = 0.5$  (black curve). Thus, roughly half of the impurities are initialised inside the 3D region. The blue curve shows the impurity density at  $t = 0.1s$  for the axisymmetric case with rotation and the red curve the 3D case with rotation and NTV electric field. We see that 0.1s is enough for the particles to strongly accumulate on axis and obtain the same accumulation shown in the saturated state of figure 4.11b, while for the axisymmetric case (blue curve of figure 4.11c) the off-axis accumulation level is not the same as that observed in the saturated state of figure 4.11b. Considering the time interval of 0.1s and  $(r/a)^2 = 0.5$  we conclude that the transport due to the synergy of 3D effects, rotation and NTV is fast. The diffusion coefficient for this case is  $D_{num}^{Neo} \approx 5.0 m^2/s$  i.e. two orders of magnitude larger than the axisymmetric case without rotation, and one order of magnitude larger than the rotating axisymmetric case. In addition, the final state of the 3D rotating case is much more peaked than the other two cases.

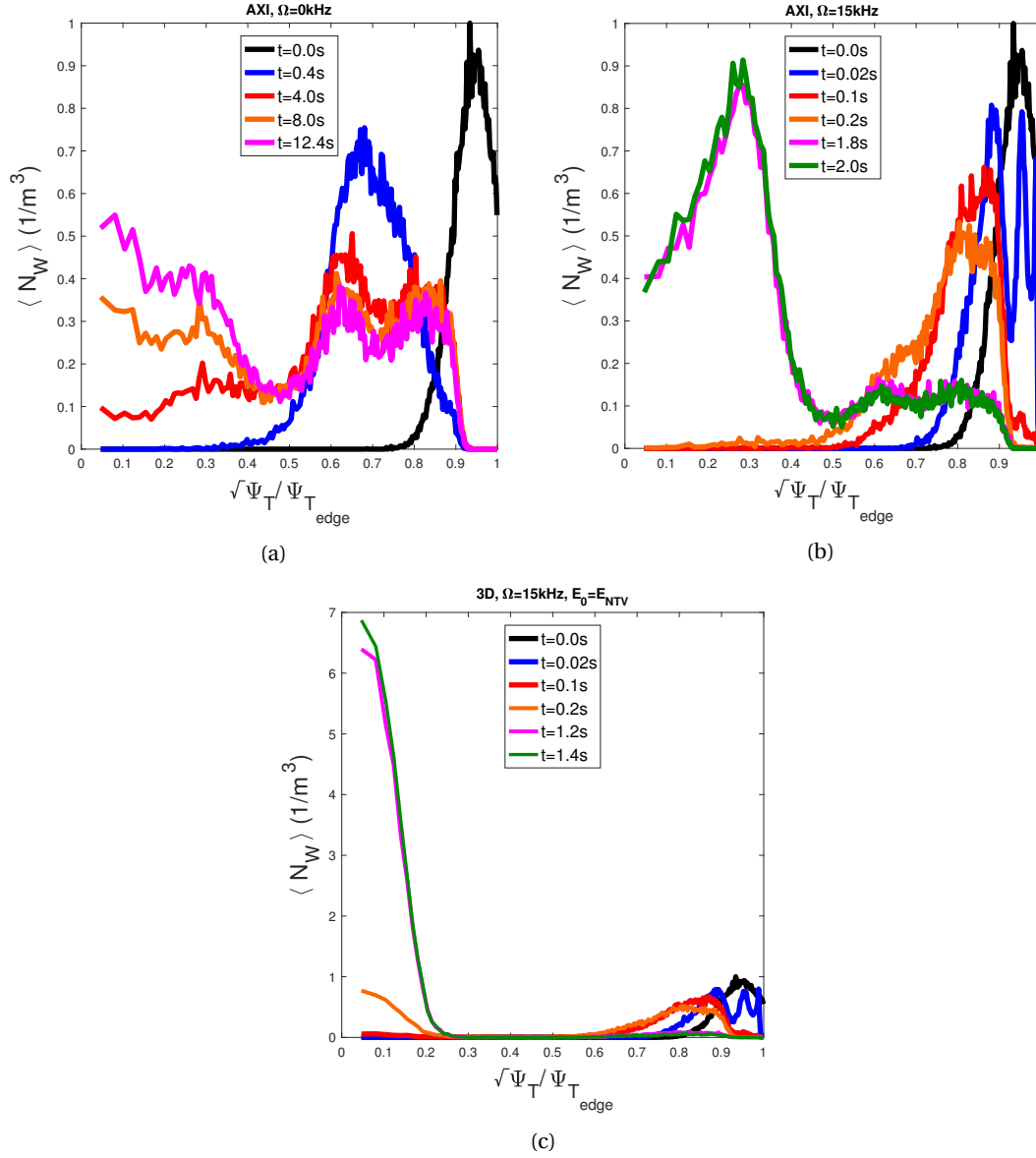


Figure 4.11 – Flux averaged radial profiles of heavy impurity density obtained with VENUS-LEVIS at different times normalized against the maximum  $\langle N_W \rangle_0$  of the flux averaged density profile for the initial configuration ( $t=0.0s$ ). This allows an investigation into the radial speed of impurities in the presence of the different physics effects. (a) Axisymmetry without rotation. (b) Axisymmetry with rotation  $f_{mode} = 15kHz$ . (c) 1/1 internal kink with  $f_{mode} = 15kHz$  and NTV electric field. The initial flux averaged density profile is approximately the same (black data points) in (a), (b) and (c).



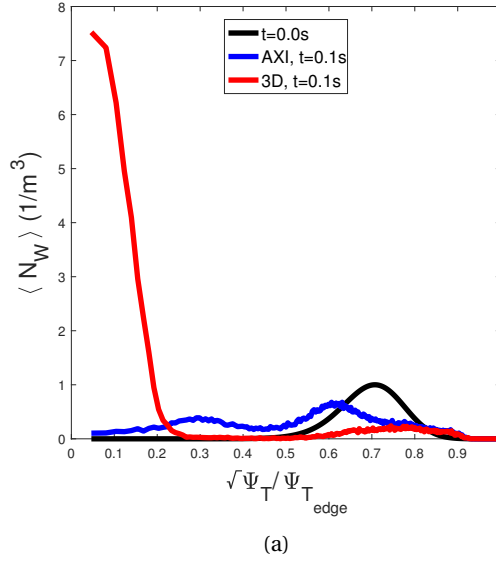


Figure 4.12 – Flux averaged radial profiles of heavy impurity density obtained with VENUS-LEVIS at different times normalized against the maximum. The particles are initialised around  $(r/a)^2 = 0.5$ .

#### 4.7 Impact of the 1/1 internal kink amplitude on heavy impurity transport

Simulations were performed with various kink perturbation amplitudes in order to see if the kink amplitude is the main player in setting the very fast transport described above. The amplitude of the  $m = 1, n = 1$  radial displacement  $\xi$  (and associated perturbed poloidal magnetic field  $\delta B_{(1,1)}$ ) used for the equilibrium in figure 4.11c was reduced to 74.91%, 53.53%, 29.60%, 16.22% and 12.15% while maintaining other conditions (see figure 4.13). The values of  $\xi$  were taken at the position of the minimum of the safety factor profile. In figure 4.13a we can see the heavy impurity density normalized against  $\langle N_W \rangle_0$  at  $t = 0.2s$  for the different levels of reduced kink amplitude. The results indicate that the levels of transport are reduced as the kink amplitude is decreased. The peaking of the saturated heavy density profile also decreases with a decrease of the kink amplitude as expected. This can be seen in figure 4.13b in which the saturated heavy impurity density normalized against  $\langle N_W \rangle_0$  is shown for different values of the kink amplitude. At kink amplitudes of 16.22% and 12.15% (relative to the amplitude of the kink shown in figure 4.11c) the transport is as slow as the axisymmetric transport with rotation (see figure 4.13a). However, the kink amplitudes of 16.22% and 12.15% seem to still have a non-negligible impact in the peaking of the saturated density. The saturated states for these two cases, respectively curves red and blue of figure 4.13b are slightly deviated from the axisymmetric case (black curve). It is also interesting to note that in figure 4.13b the behaviour of the saturated density in the region  $0.6 < r < 1$  for the 3D cases with largest perturbation amplitudes is different from the axisymmetric case. It is important to point out that although

the amplitude of the  $1/1$  mode is much larger in the core region, there is still a residual nonzero amplitude of this mode in the outer region. Moreover, residual amplitudes of other modes with  $n \neq (0, 1)$  exist throughout the plasma for the 3D simulation (see figure 3.8). However, no distinct behaviour was seen when artificially setting these residual 3D modes in the outer region. The same transport characteristics were still observed for the region  $0.6 < r < 1$ . This means that this behaviour is due to the transport caused by the  $n = 1$  mode extending into the outer region. The overall saturated density profile is affected by the extra transport due to the NTV electric field.

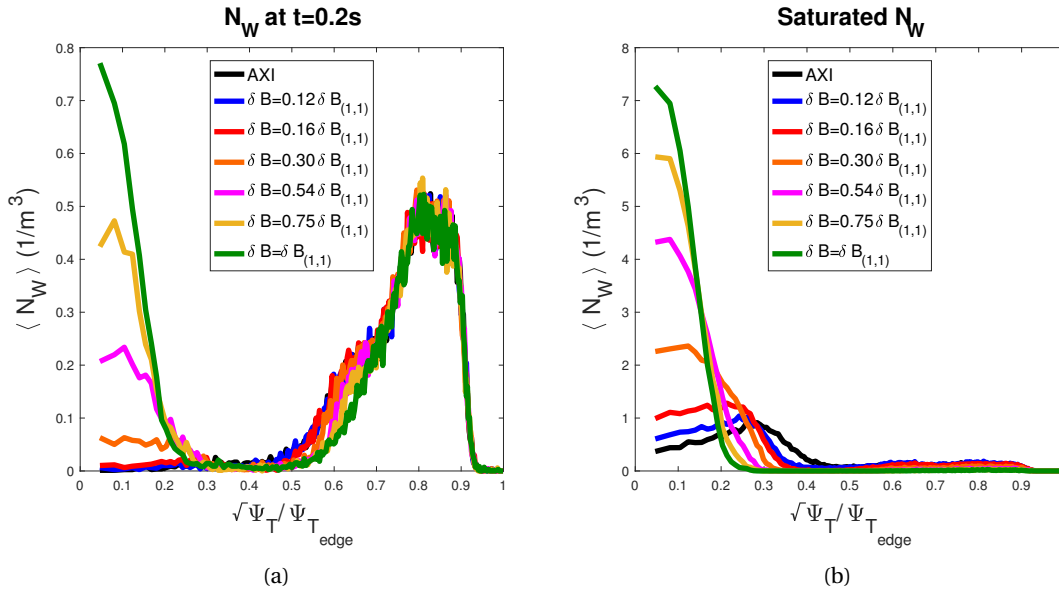


Figure 4.13 – Effect of reducing the amplitude of the kink displacement of figure 3.7 ( $\delta B = \delta B_{(1,1)}$ ). (a) Normalized impurity density at  $t = 0.2s$ . (b) Saturated normalized impurity density.

Instead of a 3D effect, one might think that the experimentally observed fast transport is due to an increase of the main ion density gradient, or due to a hollow main ion temperature profile in the kink region caused by the effect of the 3D field on profiles. The case of a hollow temperature profile is of particular interest as the on-axis plasma temperature decreases slightly between the times  $t = 45.9s$  and  $t = 46.63s$  for the JET pulse #92181, which can be seen in figures 3.2 and 3.3. Axisymmetric simulations were thus performed with increased normalized main ion density gradient in the kink region. A normalized main ion density gradient of one order of magnitude larger than the one used in figure 4.11b was considered. Impurity accumulation on axis was observed after  $0.5s$  for particles initialised around  $s = 0.9$ , which leads to a diffusion coefficient of  $D_{num}^{Neo} \approx 1.8m^2/s$  which is still slower than the diffusion coefficient  $D_{num}^{Neo} \approx 5.0m^2/s$  observed for the 3D case with  $\delta B = \delta B_{(1,1)}$ . A similar result was obtained when considering a hollow main ion temperature profile in the core region with a normalized temperature gradient of one order magnitude larger than the gradient used in

figure 4.11b. This is expected since both diffusion coefficients 2.151 and 2.152 associated with main ion density and temperature gradients have the same magnitude.

It is worth noting that the increased impurity accumulation on axis could also lead to a large impurity density gradient. This gradient, if large enough, could be a source of a secondary stage of fast transport. This effect is not taken into account in VENUS-LEVIS. For the trace limit which we consider in VENUS-LEVIS this drive of impurity transport should be smaller by a factor of  $1/Z_W$  than the other drives. Dropping the trace limit could in principle enhance or decrease the diffusion coefficient associated with the impurity density gradient as well as any of the other diffusion coefficients. However, such a study is out of the scope of the work of this thesis. From the simulations performed, we conclude that the fast transport observed in figures 3.2 and 3.3 (JET) is best explained by 3D effects when the trace limit is a good approximation. And when it is not a good approximation, the 3D effects considered here establish rapidly peaked conditions from which self collision effects may then take over later.

## 4.8 Conclusion

This chapter focused in applying the numerical tools developed and presented in chapter 3 to gain a better understanding of how a saturated 1/1 internal kink mode can impact heavy impurity transport.

We first recover the well known physics of axisymmetric heavy impurity transport in the absence of strong rotation. The friction force, in an axisymmetric equilibria, pushes the impurities radially inward while the thermal force provides a screening effect of impurities (44). When including strong toroidal rotation, similar to that observed experimentally for the JET pulse of interest (see figures 3.2, 3.3 and 4.2), the usual poloidal centrifugal trapping of the impurities is observed (see 4.4b) which enhances the heavy impurity transport driven by the friction and thermal forces (see figure 4.11) (46), (47), (48). However, for the experimental case of interest the rotation is strong enough for the radial centrifugal force to be important in driving radially outward transport of impurities (as studied in (46)), which makes them accumulate off-axis (see figure 4.4a), contrary to what would happen if no rotation was present (see figure 4.4a).

We then analysed the effect of the 1/1 internal kink on the heavy impurity behaviour. We first studied the interesting case (though not completely consistent) of no ambipolar electric field. In this situation the background ion mean parallel diamagnetic flow and heat flux is seen to play an important role on heavy impurity transport if impurity density asymmetries due to centrifugal effects are present. The flow inverts its sign in the region of the kinked core, when compared with its axisymmetric value. As a result, the friction force in the kinked region will act to screen impurities from the core while the thermal force will act to push them to the axis if strong rotation is present (see figure 4.5). The fully consistent 3D case with the effect of the 1/1 internal kink, strong rotation and ambipolar electric field is then considered. It is seen that the electric field due to NTV is enough to drive strong accumulation of the

impurities, contrary to what is seen in the consistent axisymmetric case (see figure 4.7). The impurity accumulation is generated by the synergy between the effects of the  $1/1$  internal kink, strong rotation, and ambipolar electric field, thus explaining the observed accumulation of impurities in the strong 3D phase of the JET pulse #92181 (compare figures 3.3 and 4.7). The transport due to the consistent treatment of 3D effects is seen to be enhanced when compared to the case of axisymmetry with rotation (see figure 4.11). We also conclude that decreasing the size of the  $1/1$  internal kink perturbation decreases this enhancement of the impurity transport, but even small  $1/1$  internal kink amplitudes can have an effect on the final saturated heavy impurity state. Finally, we also try to postulate the physical mechanism behind the tungsten density 'hole' observed in ASDEX-U (53). We use an ad-hoc model for an ambipolar electric field associated with an electron root that could appear in ECRH heated operational scenarios, which is similar to previously suggested models (72) but with a smaller magnitude. However, in (72) the heavy impurity physics was not described in detail, whilst in this thesis we can make use of the tools developed to model and understand the impurity behaviour in the presence of such an ambipolar electric field, flows and 3D effects. A hollow tungsten density is observed as a result. While better modelling of the electric field in such cases is necessary in the future, the calculations presented here give some insight into the behaviour of heavy impurity transport in the presence of an electron root solution for the ambipolarity electric field, strong rotation and a  $1/1$  internal kink mode. Such a situation is useful for understanding ASDEX-U experiments and future ITER scenarios in which such scenarios can be present.

To summarize, the results obtained in this chapter provide a better understanding of the impact of long living  $1/1$  internal kink modes on heavy impurity transport. This understanding should help provide ways of designing operational scenarios to prevent heavy impurity accumulation, either by avoiding such modes or making use of them to help screen impurities. Indeed, we see that reducing the  $1/1$  internal kink amplitude to small values can reduce accumulation drastically (see figure 4.13b). Furthermore, the interesting effect of the ion parallel mean flow as well as the screening effect of an electron root solution of the ambipolar electric field could in principle be manipulated to design operational scenarios in the presence of a long living  $1/1$  internal kink mode to screen impurities from the core.

## 5 Conclusions and Outlook

This thesis pursued modelling of heavy impurity transport in the presence of long living saturated 3D MHD perturbations. Such features are important in tokamaks with tungsten divertors. Although, mostly axisymmetric, the plasma in these devices can often present long living 3D saturated perturbations, like for example the 1/1 internal kink. However, the effect of such 3D structures is often not considered when modelling the behaviour of heavy impurity transport. Historically, this has been presumably in order to focus on other important physics properties such as strong toroidal rotation, ICRH heating and the evolution of the background ion density and temperature profiles. Another reason for this could be simply that 3D transport with rotation has been considered too complex. However, we know from stellarator devices that 3D geometry strongly impacts impurity transport. It is thus not obvious why the same should not happen in tokamak plasmas with 3D MHD perturbations. Nevertheless, it is not possible to just assume that the same impurity behaviour observed in stellarators will be observed in tokamaks with 3D perturbations, because stellarators lack strong plasma rotation. It is known that rotation has an important impact on heavy impurity transport even in axisymmetric tokamak plasmas. Crucially, we have shown in this thesis that the synergetic effect of strong toroidal rotation and 3D MHD perturbations are crucial for fully describing heavy impurity transport in tokamaks with long living 3D perturbations.

The analytical descriptions and models of interest to study heavy impurity transport in such scenarios are presented in chapter 2. These results are needed to further develop the code packages composed of VMEC, VENUS-LEVIS and auxiliary codes, as addressed and presented in chapter 3. Finally, in chapter 4, we used the numerical tools described in chapter 3 to model heavy impurity transport in the presence of a 1/1 internal kink mode. The main objective of this study was to model the weakly and strongly 3D phase of JET pulse #92181 in which a long living 1/1 mode was present. Due to the existence of such an experimental scenario, such studies provide a ‘benchmark’ of the code against experiment, as well as to better understand the different physics involved in such scenarios. As such, we start by modelling the weakly 3D phase with an axisymmetric equilibrium. The usual inward radial transport due to the friction force is observed, despite the screening provided by the thermal force. However,

the strong rotation force observed in such experiments provides both poloidal asymmetries as well as screening due to the strong radial centrifugal force. The screening provided by the radial centrifugal force is enough to accumulate the impurities off-axis, which agrees with the experimental observations in the weak 3D phase of JET pulse #92181. Contrary to the axisymmetric case, the consistent model of a 1/1 internal kink mode shows on-axis accumulation of heavy impurities due to the synergetic effect of the 3D geometry, rotation and NTV ambipolar electric field. Such strong accumulation agrees with the experimental observations of the strongly 3D phase of JET pulse #92181. Furthermore, the synergy between 3D, rotation and NTV ambipolar electric field is observed to enhance the heavy impurity diffusion coefficient by an order of magnitude when compared with the axisymmetric case with the same rotation. These results are thus a step forward in understanding the importance of the effect of the 1/1 internal kink mode on heavy impurity transport through modelling. In particular, these results help in the understanding of heavy impurity behaviour during JET hybrid scenarios in which the 1/1 internal kink is present. Previous modelling had been undertaken in (55) and (56), but important effects such as the thermal force and the ambipolar electric field were not taken into account in a consistent way.

Since the results are systematically studied by investigating the effect of every physics mechanism involved on heavy impurity transport one might hope to isolate the physics mechanisms observed in ASDEX-U experiments as well as possible ITER and DEMO scenarios with 1/1 kink modes. However, these tokamaks have (or will have) the possibility of heating the plasma through ECRH. Such a heating system, not present in JET experiments, may add extra important physics when considering the behaviour of heavy impurity transport (53). In order to gain some physical insight a simple model for an ECRH ambipolar electric field was considered. The model consisted of simply choosing the ambipolarity electric field as  $E_{ECRH} = -E_{NTV}$ . This was done to model the electron root solution (positive electric field) often associated with such scenarios due to the loss of hot electrons. While the choice of such an electric field seems a rather crude approximation, it is not much more crude than previous proposed analytical solutions (72). In the latter paper (72), the ambipolar electric field solution is found to be approximately constant in the core region and positive, but the heavy impurity physics is not modelled in detail. The electric field  $E_{ECRH}$  chosen for our simulation is almost constant, albeit of smaller magnitude than in (72), and with that electric field, the simulations in this thesis provide an extra insight into how the heavy impurities actually behave in the presence of the ambipolar electric field. The results are in agreement with the observations seen in an ASDEX-U scenario in which a 1/1 internal kink mode and ECRH heating are simultaneously present (53). This is an interesting result in itself as it shows that screening of the impurities from the kinked region should occur for a positive ambipolar electric field. Nevertheless, to better compare against the ASDEX-U experiments more precise modelling of the ambipolar electric field is necessary. Such an extension of this work could indeed be important as it also has implications for better understanding of future ITER scenarios in which ECRH may be applied during hybrid operation with a 1/1 internal kink mode. The extension of this work may be achieved by using a better electric field estimate of ASDEX-U experiments, in particular via

dedicated simulations.

Whilst the results presented in this thesis are focused on understanding the effect of the 1/1 internal kink mode on heavy impurity transport, both the theoretical and numerical frameworks in chapters 2 and 3 can be used to consider long lived 3D ideal MHD saturated perturbations beyond that of the 1/1 internal kink. For example, edge harmonic oscillations are quite important in the present panorama of tokamak physics. These 3D MHD perturbations are present in QH-mode operation scenarios. Such scenarios are being considered for the European DEMO design because they avoid edge localised modes which are intolerable for a machine the size of DEMO (and most likely ITER). The presence of such modes, though beneficial in this way, could indirectly lead to strong transport of heavy impurity from the edge region to the core region. Indeed, there may be indications that EHOs in ASDEX-U can cause inward transport of impurities. The numerical tools presented in this thesis could be used to study such a problem and help understanding the effect of such modes on heavy impurity transport. Such modelling has already been started, but the results are still inconclusive as the heavy impurity transport in such cases depends greatly on the choice of the background ion density and temperatures. Furthermore, the importance of self-induced impurity density asymmetries due to collisions seem to be quite important due to the strong gradients present in such experiments. For some cases a radially inward transport of impurities has been seen, but for other cases the opposite occurs. More modelling on this subject is thus necessary.

We have seen that the results of this thesis demonstrate the importance of considering 3D MHD perturbations in tokamak plasmas when studying heavy impurity transport. The theoretical understanding obtained from this work may help provide insight into how to mitigate heavy impurity accumulation during other saturated modes like EHOs in the future. However, the study of the effect of nonlinear island perturbations on heavy impurity transport is also very important because high performance pulses often have neoclassical tearing modes and we have seen devastating inward impurity transport in JET (54). Treating these types of structures with the formalism in this thesis is a more difficult subject, but it should be possible provided a way of calculating the background ion flow and heat flux exists. The drift kinetic equation for the main ions has to be solved in the presence of such structures to obtain the necessary geometrical factors. While some existing analytical calculations (35) provide approximated formulas for the geometrical factors for such cases, a general formula does not exist. Nevertheless, an alternative method to obtain the required flow and heat flux may exist. Indeed, it should be possible to obtain the ion and electron flows as well as the ion heat flux by successively following bulk ions and electrons numerically, and to sample the flow and heat flux of the ions from the velocity distribution obtained. This would have to be undertaken in a magnetic configuration which includes the effects of a magnetic island. Once this has been accomplished it should be easy to then undertake the remaining modelling for the heavy impurity transport. Such an approach may be beneficial not only for the studying of nonlinear MHD tearing modes, but also to obtain more exact numerical solutions for the ion and electron flow in the presence of 1/1 non-resonant internal kink modes or EHOs. This fully consistent methodology would also make possible to obtain a more accurate solution of the

ambipolar electric field for all applications.

We conclude by saying that the work of this thesis has successfully explained the accumulation of impurities during 1/1 experiments JET and ASDEX-U, but also lays down the foundations for exciting and important applications in the future.



# A Considerations on flux coordinates

We present here some details on how to transform between general flux coordinate system to Boozer and Hamada coordinates. This derivation is based on the one presented in (63). It is presented here to help understand the numerical auxiliary code developed to transform between VMEC coordinates and Boozer or Hamada coordinates. Part of this discussion was done in section 2.4.

## A.1 Flux coordinates

As stated in section 2.3 the equilibrium magnetic field in the MHD description of a plasma obeys to the following equations in the absence of strong flows

$$\mathbf{J} \times \mathbf{B} = \nabla P, \quad (\text{A.1})$$

$$\mu_0 \mathbf{J} = \nabla \times \mathbf{B}, \quad (\text{A.2})$$

$$\nabla \cdot \mathbf{B} = 0. \quad (\text{A.3})$$

Such equations imply that the equilibrium magnetic field configuration established in the plasma has a special relation with the density current and the pressure in the plasma. This special relation allows the plasma to be more easily described in a set of spatial coordinates called flux coordinates (63), (64), (65), (66). These special set of coordinates are important as they often simplify calculations. Equation A.2 leads to the constraint

$$\nabla \cdot \mathbf{J} = 0. \quad (\text{A.4})$$

Moreover, 2.36 implies the following constraints

$$\mathbf{J} \cdot \nabla P = 0 \quad (\text{A.5})$$

## Appendix A. Considerations on flux coordinates

---

and

$$\mathbf{B} \cdot \nabla P = 0. \quad (\text{A.6})$$

These constraints mean that in a magnetic field configuration obeying to the MHD force balance equation, the current density and magnetic field vectors lie in surfaces of constant pressure. This implies that each of these surfaces have an associated magnetic flux and total current associated with them. This is so because the magnetic field and density current vector fields have zero divergence, and thus the same magnetic and current lines will stay in the same surface along the entirety of the torus. We then call these surfaces, flux surfaces. Another equivalent meaning of these constraints is to state that if we describe the magnetic field and current density in a set of flux coordinates  $(s, \theta, \phi)$ , where  $s$  is a radial coordinate that labels the flux surface, then the magnetic field and current density vanish across flux surfaces which can be mathematically written as  $B^s = 0$  and  $J^s = 0$ . These constraints greatly simplify the description of problems in the MHD description. If we assume that the toroidal magnetic equilibrium described by such equations can be represented by these flux surfaces in a way that they are nested surfaces with a single magnetic axis, then we can describe the pressure as being function of the single radial variable:

$$P = P(s) \quad (\text{A.7})$$

Equations A.3, A.6 and A.7 implies that a potential function  $v^*$  exists such that the contravariant magnetic field is of the form

$$\mathbf{B} = \nabla s \times \nabla v^*. \quad (\text{A.8})$$

Equations A.4, A.5 and A.7 implies that a potential function  $w^*$  exists such that the contravariant current density is of the form

$$\mathbf{J} = \nabla w^* \times \nabla s. \quad (\text{A.9})$$

This form of the current density vector in conjunction with Faraday's law A.2 implies that a potential function  $u^*$  exists such that the covariant magnetic field is of the form

$$\mathbf{B} = \nabla u^* + w^* \nabla s. \quad (\text{A.10})$$

The definitions of poloidal and toroidal magnetic flux inside a poloidal and toroidal flux surface labeled by  $s$  are given by

$$2\pi\Psi_P(s) = \int \int B^\theta ds d\phi \quad (\text{A.11})$$

and

$$2\pi\Psi_T(s) = \int \int B^\phi ds d\theta. \quad (\text{A.12})$$

As such the form of potential function  $\nu^*$  has to be

$$\nu^*(s, \theta, \phi) = \frac{d\Psi_T}{ds}\theta - \frac{d\Psi_P}{ds}\phi + \tilde{\nu}(s, \theta, \phi), \quad (\text{A.13})$$

in which  $\tilde{\nu}(s, \theta, \phi)$  is an arbitrary periodic function in  $\theta$  and  $\phi$ .

The definitions of poloidal and toroidal current (multiplied by  $\mu_0$ ) passing through a poloidal and toroidal flux surface labeled by  $s$  are given by

$$2\pi I_P(s) = \int \int \mu_0 J^\theta ds d\phi \quad (\text{A.14})$$

and

$$2\pi I_T(s) = \int \int \mu_0 J^\phi ds d\theta \quad (\text{A.15})$$

and lead in a similar fashion to the following form for the potential function  $w^*$

$$w^*(s, \theta, \phi) = -\frac{dI_T}{ds}\theta - \frac{dI_P}{ds}\phi + \tilde{w}(s, \theta, \phi), \quad (\text{A.16})$$

in which  $\tilde{w}(s, \theta, \phi)$  is again an arbitrary periodic function in  $\theta$  and  $\phi$ . Faraday's law A.2 then implies that the potential function  $u^*$  is

$$u^*(s, \theta, \phi) = I_T\theta + I_P\phi + \tilde{u}(s, \theta, \phi), \quad (\text{A.17})$$

with  $\tilde{u}(s, \theta, \phi)$  an arbitrary periodic function in  $\theta$  and  $\phi$ . These potential functions define an arbitrary set of flux coordinates. Choosing specific forms of the functions  $\tilde{\nu}(s, \theta, \phi)$ ,  $\tilde{w}(s, \theta, \phi)$  and  $\tilde{u}(s, \theta, \phi)$  will lead to different choice of  $\theta$  and  $\phi$  coordinates. Each set of flux coordinates  $(s, \theta, \phi)$  is a valid set of coordinates to describe a equilibrium magnetic field which is a solution of the MHD force balance equation A.1. Substituting A.13, A.16 on A.8 and A.10 and using these formulas on the MHD equilibrium equation A.1 one obtains the follow equations

$$\mathbf{B} \cdot \nabla \tilde{w}(s, \theta, \phi) = \frac{dP}{ds} + \frac{dI_T}{ds}B^\theta + \frac{dI_P}{ds}B^\phi, \quad (\text{A.18})$$

$$\mathbf{B} \cdot \nabla \tilde{\nu}(s, \theta, \phi) = \frac{dP}{ds} - \frac{d\Psi_T}{ds}J^\theta + \frac{d\Psi_P}{ds}J^\phi, \quad (\text{A.19})$$

$$\mathbf{B} \cdot \nabla \tilde{u}(s, \theta, \phi) = B^2 - I_TB^\theta - I_PB^\phi, \quad (\text{A.20})$$

which can be used to obtain the function  $\tilde{w}$  and hold in any flux coordinate system. These equations are magnetic differential equations due to the presence of the magnetic differential operator  $\mathbf{B} \cdot \nabla$ . Such type of equations can be written generally as

## Appendix A. Considerations on flux coordinates

---

$$\mathbf{B} \cdot \nabla \mathcal{F}(s, \theta, \phi) = \mathcal{S}, \quad (\text{A.21})$$

with  $\mathcal{S}$  a single-valued periodic function. Such type of equations have the two following solvability conditions (63)

$$\langle \mathcal{S} \rangle = 0, \quad (\text{A.22})$$

$$\int \frac{dl}{B} \mathcal{S} = 0 \quad (\text{A.23})$$

in which the flux average for a function  $X(s, \theta, \phi)$  is defined as

$$\langle X(s, \theta, \phi) \rangle(s) = \frac{\int_0^{2\pi} \int_0^{2\pi} X(s, \theta, \phi) \sqrt{g} d\theta d\phi}{\int_0^{2\pi} \int_0^{2\pi} \sqrt{g} d\theta d\phi} = \frac{\int_0^{2\pi} \int_0^{2\pi} X(s, \theta, \phi) \sqrt{g} d\theta d\phi}{V'}. \quad (\text{A.24})$$

Here,  $\sqrt{g}(s, \theta, \phi) = (\nabla s \cdot \nabla \theta \times \nabla \phi)^{-1}$  is the jacobian in the set of flux coordinates  $(s, \theta, \phi)$  and  $V(s)$  is the volume enclosed by the flux surface labeled by  $s$  such that the differential volume element is  $dV = \sqrt{g} ds d\theta d\phi$ .  $dl$  is the line element along a closed magnetic field line. Applying these two solvability constraints to either equation A.18 or A.19 yields the two following equations

$$\frac{dP}{dV} = -4\pi^2 \left( \frac{dI_T}{dV} \frac{d\Psi_P}{dV} + \frac{dI_P}{dV} \frac{d\Psi_T}{dV} \right), \quad (\text{A.25})$$

$$\int \frac{dl}{B} = \frac{N_T}{2\pi} \frac{d\Psi_T}{dV}, \quad (\text{A.26})$$

in which  $N_T$  is the number of toroidal rotations that a closed magnetic field line undergoes. Equation A.25 states the flux averaged MHD balance equation. Applying the same solvability constraints to A.20 holds the following equations

$$\langle B^2 \rangle = 4\pi^2 \frac{d\Psi_T}{dV} (I_P + \iota I_T), \quad (\text{A.27})$$

$$\int B dl = 2\pi N_T (I_P + \iota I_T), \quad (\text{A.28})$$

in which  $\iota(s) = \frac{d\Phi_P}{d\Phi_T} = \frac{1}{q(s)}$  the rotational transform,  $q(s)$  the safety factor. The constraints A.25, A.26, A.27 and A.28 have to hold in a system of flux coordinates  $(s, \theta, \phi)$  in order for such coordinate system to exist. It is of often the case in which is interesting to work with flux coordinates with distinct properties. Such case is when we want to solve magnetic differential equations like the ones just presented which have a magnetic differential operator  $\mathbf{B} \cdot \nabla$ . General flux coordinates already simplify this operator by ensuring  $B^s = 0$ . Nevertheless, it is clear that this operator is treated in a simpler way if the poloidal and toroidal contravariant components of

the magnetic field are flux functions such that  $\langle B^\theta(s, \theta, \phi) \rangle = B^\theta(s)$  and  $\langle B^\phi(s, \theta, \phi) \rangle = B^\phi(s)$ . In which we define for an arbitrary function flux function  $X(s)$  the following notation  $X'(s) = \frac{dX}{ds}$ . The sets of flux coordinates in which the contravariant components of  $B$  are flux functions are called straight field line coordinates as the representation of the field lines in the  $(\theta, \phi)$  plane are straight lines. Since from A.8 the magnetic field lines are defined by the intersection of a flux surface  $s$  and a surface in which  $v^*$  is constant it is clear to see that straight field line coordinates are obtained when imposing  $\tilde{v} = 0$ . The simplest set of coordinates that can be obtained without considering the trivial case (with  $v^* = u^* = w^* = 0$ ) are obtained by imposing  $v^* = u^* = 0$  or  $v^* = w^* = 0$ . The first set of coordinates are called Boozer coordinates (64), (65) and the second Hamada coordinates (66).

## A.2 Boozer coordinates

Boozer coordinates  $(s, \theta_B, \phi_B)$  are straight field line coordinates with a simpler representation of the covariant magnetic field and jacobian. Imposing  $v^* = u^* = 0$  leads to the following forms of the potential functions  $v^*(s, \theta_B, \phi_B)$ ,  $u^*(s, \theta_B, \phi_B)$  and  $w^*(s, \theta_B, \phi_B)$  in Boozer coordinates

$$v^*(s, \theta_B, \phi_B) = \frac{d\Psi_T}{ds} \theta_B - \frac{d\Psi_P}{ds} \phi_B, \quad (\text{A.29})$$

$$u^*(s, \theta_B, \phi_B) = I_T \theta_B + I_P \phi_B. \quad (\text{A.30})$$

$$w^*(s, \theta_B, \phi_B) = -\frac{dI_T}{ds} \theta_B + \frac{dI_P}{ds} \phi_B + \tilde{w}_B(s, \theta_B, \phi_B). \quad (\text{A.31})$$

with  $\tilde{w}_B(s, \theta_B, \phi_B)$  the  $\tilde{w}$  function of Boozer coordinates. Since the potential functions  $v^*$ ,  $u^*$  and  $w^*$  are scalars they have to be identical they are identical even when described in different system of coordinates. We can thus match equations A.29 to A.13 and A.30 to A.17 to obtain the general angle transformation between a general set of flux coordinates  $(s, \theta, \phi)$  and Boozer coordinates  $(s, \theta_B, \phi_B)$ .

$$\theta_B = \theta + \frac{d\Psi_T}{ds}^{-1} \tilde{v}(s, \theta, \phi) + \frac{d\Psi_P}{ds} G_B(s, \theta, \phi), \quad (\text{A.32})$$

$$\phi_B = \phi + \frac{d\Psi_T}{ds} G_B(s, \theta, \phi), \quad (\text{A.33})$$

with the Boozer coordinates generator function given by

$$G_B(s, \theta, \phi) = -\frac{I_T \frac{d\Psi_T}{ds}^{-1} \tilde{v}(s, \theta, \phi) - \tilde{u}(s, \theta, \phi)}{\frac{d\Psi_T}{ds} (I_P + I_T)}. \quad (\text{A.34})$$

Matching A.48 to A.16 and using definitions A.32, A.33 and A.34 one obtains

## Appendix A. Considerations on flux coordinates

---

$$\tilde{w}_B(s, \theta, \phi) = \tilde{w}(s, \theta, \phi) + \frac{\frac{dI_T}{ds}}{\frac{d\Psi_T}{ds}} \tilde{v}(s, \theta, \phi) + \frac{d\Psi_T}{ds} \left( \frac{dI_P}{ds} + \iota \frac{dI_T}{ds} \right) G_B(s, \theta, \phi). \quad (\text{A.35})$$

Inserting A.13, A.16 and A.17 in A.8, A.9 and A.10 we obtain

$$\mathbf{B} = \frac{d\Psi_T}{ds} \nabla s \times \nabla \theta_B - \frac{d\Psi_P}{ds} \nabla s \times \nabla \phi_B = \nabla \Psi_T \times \nabla \theta_B - \iota \nabla \Psi_T \times \nabla \phi_B, \quad (\text{A.36})$$

$$\mathbf{J} = \frac{dI_T}{ds} \nabla s \times \nabla \theta_B + \frac{dI_P}{ds} \nabla s \times \nabla \phi_B + \nabla \tilde{w}_B \times \nabla \phi_B, \quad (\text{A.37})$$

$$\mathbf{B} = \tilde{w}_B \nabla s + I_T \nabla \theta_B + I_P \nabla \phi_B. \quad (\text{A.38})$$

It is clear that the contravariant and covariant forms of the magnetic field are simpler in Boozer coordinates. Since  $\tilde{u}_B = 0$  in Boozer coordinates, equation A.20 delivers a form for the jacobian in these coordinates

$$\sqrt{g_B} = \frac{d\Psi_T}{ds} \frac{I_P + \iota I_T}{B^2}, \quad (\text{A.39})$$

and equation A.18 in Boozer coordinates holds a magnetic differential equation for  $\tilde{w}_B(s, \theta, \phi)$

$$\mathbf{B} \cdot \nabla \tilde{w}_B(s, \theta, \phi) = \frac{dP}{ds} \left( 1 - \frac{B^2}{\langle B^2 \rangle} \right). \quad (\text{A.40})$$

Using the transformation equations A.32 and A.33 one obtains a relation between the jacobians in the general system of coordinates  $(s, \theta, \phi)$  and the Boozer coordinate system  $(s, \theta_B, \phi_B)$  which can be written as

$$\mathbf{B} \cdot \nabla G_B(s, \theta, \phi) = \frac{1}{\sqrt{g_B}} - \frac{1}{\sqrt{g}} \left( 1 + \frac{d\Psi_T}{ds}^{-1} \frac{\partial \tilde{v}(s, \theta, \phi)}{\partial \theta} \right). \quad (\text{A.41})$$

If  $\tilde{v}(s, \theta, \phi)$ ,  $\sqrt{g}(s, \theta, \phi)$  and  $B^2(s, \theta, \phi)$  are known in  $(s, \theta, \phi)$ , equations A.40 and A.41 can be used to construct the Boozer coordinate system.

### A.3 Hamada coordinates

Hamada coordinates  $(s, \theta_H, \phi_H)$  have the particularity of being straight field line coordinates in which the current lines are also straight and the jacobian  $\sqrt{g_H}(s, \theta_H, \phi_H)$  is a flux function. Imposing  $v^* = w^* = 0$  leads to the following forms of the potential fuctions  $v^*(s, \theta_H, \phi_H)$ ,  $u^*(s, \theta_H, \phi_H)$  and  $w^*(s, \theta_H, \phi_H)$  in Hamada coordinates

$$v^*(s, \theta_H, \phi_H) = \frac{d\Psi_T}{ds} \theta_H - \frac{d\Psi_P}{ds} \phi_H, \quad (\text{A.42})$$

$$u^*(s, \theta_H, \phi_H) = I_T \theta_H + I_P \phi_H + \tilde{u}_B(s, \theta_H, \phi_H), \quad (\text{A.43})$$

$$w^*(s, \theta_H, \phi_H) = -\frac{dI_T}{ds} \theta_H - \frac{dI_P}{ds} \phi_H. \quad (\text{A.44})$$

with  $\tilde{u}_B(s, \theta_B, \phi_B)$  the  $\tilde{u}$  function of Boozer coordinates. We can thus match equations A.42 to A.13 and A.44 to A.16 to obtain the general angle transformation between a general set of flux coordinates  $(s, \theta, \phi)$  and Hamada coordinates  $(s, \theta_H, \phi_H)$ .

$$\theta_H = \theta + \frac{d\Psi_T}{ds}^{-1} \tilde{v}(s, \theta, \phi) + \frac{d\Psi_P}{ds} G_H(s, \theta, \phi), \quad (\text{A.45})$$

$$\phi_H = \phi + \frac{d\Psi_T}{ds} G_H(s, \theta, \phi), \quad (\text{A.46})$$

with the Hamada coordinates generator function given by

$$G_H(s, \theta, \phi) = -\frac{I_T \frac{d\Psi_T}{ds}^{-1} \tilde{v}(s, \theta, \phi) + \tilde{w}(s, \theta, \phi)}{\frac{d\Psi_T}{ds} (I_P + \iota I_T)}. \quad (\text{A.47})$$

Matching A.43 to A.17 and using definitions A.55, A.56 and A.47 one obtains

$$\tilde{u}_H(s, \theta, \phi) = \tilde{u}(s, \theta, \phi) - \frac{I_T}{\frac{d\Psi_T}{ds}} \tilde{v}(s, \theta, \phi) - \frac{d\Psi_T}{ds} (I_P + \iota I_T) G_H(s, \theta, \phi). \quad (\text{A.48})$$

Inserting A.13, A.16 and A.17 in A.8, A.9 and A.10 we obtain

$$\mathbf{B} = \nabla \Psi_T \times \nabla \theta_H - \iota \nabla \Psi_T \times \nabla \phi_H, \quad (\text{A.49})$$

$$\mathbf{J} = \frac{dI_T}{ds} \nabla s \times \nabla \theta_H + \frac{dI_P}{ds} \nabla s \times \nabla \phi_H, \quad (\text{A.50})$$

$$\mathbf{B} = \frac{\partial \tilde{u}_H}{\partial s} \nabla s + \left( I_T + \frac{\partial \tilde{u}_H}{\partial \theta_H} \right) \nabla \theta_H + \left( I_P + \frac{\partial \tilde{u}_H}{\partial \phi_H} \right) \nabla \phi_H, \quad (\text{A.51})$$

which implies that the contravariant magnetic field and current density are straight lines. Since  $\tilde{w}_H = 0$  in Hamada coordinates, equation A.18 and A.25 implies the following form for the jacobian in these coordinates

$$\sqrt{g_H}(s) = \frac{V'}{(2\pi)^2} = \langle \sqrt{g}(s, \theta, \phi) \rangle. \quad (\text{A.52})$$

Equation A.20 in Hamada coordinates holds a magnetic differential equation for  $\tilde{u}_H(s, \theta, \phi)$

## Appendix A. Considerations on flux coordinates

---

$$\mathbf{B} \cdot \nabla \tilde{u}_H(s, \theta, \phi) = B^2 - \langle B^2 \rangle. \quad (\text{A.53})$$

Using the transformation equations A.55 and A.56 one obtains a relation between the jacobians in the general system of coordinates  $(s, \theta, \phi)$  and the Hamada coordinate system  $(s, \theta_H, \phi_H)$  which can be written as

$$\mathbf{B} \cdot \nabla G_H(s, \theta, \phi) = \frac{1}{\sqrt{g_H}} - \frac{1}{\sqrt{g}} \left( 1 + \frac{d\Psi_T}{ds}^{-1} \frac{\partial \tilde{v}(s, \theta, \phi)}{\partial \theta} \right). \quad (\text{A.54})$$

As in the Boozer case, if  $\tilde{v}(s, \theta, \phi)$ ,  $\sqrt{g}(s, \theta, \phi)$  and  $B^2(s, \theta, \phi)$  are known in  $(s, \theta, \phi)$ , equations A.53 and A.54 provide a way to construct the Hamada coordinate system.

### A.4 Transformation between straight field line coordinates

Let's suppose we want to transform from a general known system of flux coordinates  $(s, \theta, \phi)$  to Boozer or Hamada coordinates  $(s, \theta_N, \phi_N)$  as in the last two sections. But now we know that the original system is also a straight field line coordinate system. Then all the relations presented in the previous sections hold, but now we impose  $\tilde{v}(s, \theta, \phi) = 0$ . So that we have

$$\theta_N = \theta + \frac{d\Psi_P}{ds} G_N(s, \theta, \phi), \quad (\text{A.55})$$

$$\phi_H = \phi + \frac{d\Psi_T}{ds} G_N(s, \theta, \phi), \quad (\text{A.56})$$

with  $G_N(s, \theta, \phi)$  given by the Boozer or Hamada generator function (see equations A.34 and A.47) with  $\tilde{v} = 0$ . The equation for the generator is then given in general by

$$\mathbf{B} \cdot \nabla G_N(s, \theta, \phi) = \frac{1}{\sqrt{g_N}} - \frac{1}{\sqrt{g}}. \quad (\text{A.57})$$

### A.5 Axisymmetry

In the case of axisymmetry the derivatives of all quantities in order to the toroidal angle are null ( $\frac{\partial}{\partial \phi} \rightarrow 0$ ), which means that in general the contravariant and covariant forms of the magnetic field can be given by

$$\mathbf{B} = \left( q(s) + \frac{\partial \tilde{v}}{\partial \theta} \right) \nabla \Psi_P \times \nabla \theta + \nabla \phi \times \nabla \Psi_P, \quad (\text{A.58})$$

$$\mathbf{B} = \frac{\partial \tilde{u}}{\partial \Phi_P} \nabla \Phi_P + \left( I_T + \frac{\partial \tilde{u}}{\partial \theta} \right) \nabla \theta + I_P \nabla \phi. \quad (\text{A.59})$$



In the cylindrical system of coordinates  $(R, \phi_{geo}, Z)$  the toroidal angle is chosen to be the geometrical angle  $\phi_{geo}$ . Since the potential functions in axisymmetry are independent of the toroidal angle, we may substitute the general coordinate  $\phi$  by  $\phi_{geo}$  in 2.60 and 2.61. This implies then that  $B_{\phi_{geo}} = I_P(\Phi_P)$  and that the poloidal magnetic field component is then given from A.58  $\mathbf{B}_P = \nabla\phi \times \nabla\Phi_P$ , since the first term is in the toroidal direction. The magnetic field in cylindrical coordinates is written as

$$\mathbf{B} = |B_R|\hat{R} + |B_Z|\hat{Z} + |B_{\phi_{geo}}|\hat{\phi}_{geo} = \mathbf{B}_P + B_{\phi_{geo}}\nabla\phi_{geo}, \quad (\text{A.60})$$

which make sthe axisymmetric magnetic field in flux coordinates

$$\mathbf{B} = \nabla\phi \times \nabla\Psi_P + I_P\nabla\phi, \quad (\text{A.61})$$

which is the typical form of the axisymmetric magnetic field (9). It can be noted that the by changing  $\phi$  for  $\phi_{geo}$  will still change the  $\theta$  angle as well as the functions  $\tilde{v}$  and  $\tilde{u}$  but these changes have no effect on this way of writing the axisymmetric magnetic field.



## B Derivation of the drift kinetic equation

We present here a derivation of the drift kinetic equation (10), (9). Part of this topic is discussed in sections 2.1 and 2.7. We have seen in section 2.1 that the plasma can be described by following the trajectories of every particle in the system through a distribution function  $f_s(\mathbf{x}, \mathbf{v}_s, t)$ . Such distribution obeys in general to the Boltzmann equation given by

$$\frac{df_s}{dt} = C(f_s) \Leftrightarrow \frac{\partial f_s}{\partial t} + \mathbf{v}_s \cdot \nabla_{\mathbf{x}_s} f_s + \frac{\mathbf{E} + \mathbf{v}_s \times \mathbf{B}}{m_s} \cdot \nabla_{\mathbf{v}_s} f_s = C(f_s), \quad (\text{B.1})$$

A solution to such distribution would allow us to know both the movement of the guiding centers of the helical trajectories of the particles in the plasma as well as the Larmor radius gyration. However, it is impossible to solve for such a general solution. In order to solve for the distribution function it is often necessary to divide this distribution function in a part that describes the movement of the guiding centers  $\tilde{f}_s$  and a part that describes the Larmor gyration of the particles  $\tilde{f}_s$ . To better understand what this means let us write the velocity of a particle following a helical trajectory around a magnetic field line as follows

$$\mathbf{v} = v_{\parallel} \hat{\mathbf{b}} + \mathbf{v}_{\perp} = v_{\parallel} \hat{\mathbf{b}} + |\mathbf{v}_{\perp}| (\cos \varphi \hat{\mathbf{e}}_1 + \sin \varphi \hat{\mathbf{e}}_2) \quad (\text{B.2})$$

with  $(v, \varphi, v_{\parallel})$  a set of cylindrical velocity-space coordinates with the  $z$  direction along the magnetic field direction or along  $\hat{\mathbf{b}}$ . Here  $v_{\perp}$  and  $v_{\parallel}$  are respectively the magnitudes of the perpendicular and parallel components of the velocity with respect to the direction of the magnetic field line and  $\varphi$  is the gyrophase associated with the Larmor gyration.  $\hat{\mathbf{e}}_1$  and  $\hat{\mathbf{e}}_2$  are orthogonal unit vectors to  $\hat{\mathbf{b}}$ , which are dependent of the position of the particle. Thus, the distribution function would in general be written as  $f_s(\mathbf{x}, v_{\perp}, \varphi, v_{\parallel}, t)$ . If we are only interested in following the guiding centers of the particles we can take an average along the gyro movement of the particles which means taking an average in the gyrophase coordinate. The gyroaverage for a quantity  $X$  is thus defined as

## Appendix B. Derivation of the drift kinetic equation

---

$$\bar{X}(v_{\perp}, \varphi, v_{\parallel}) = \frac{1}{2\pi} \int_0^{2\pi} X(v_{\perp}, \varphi, v_{\parallel}) d\varphi. \quad (\text{B.3})$$

We call  $\bar{f}_s(\mathbf{x}, v, v_{\parallel}, t)$  the gyroaveraged distribution function.  $\tilde{f}_s(\mathbf{x}, v_{\perp}, \varphi, v_{\parallel}, t) = f_s - \bar{f}_s$  is the remainder part of the distribution function. The position of the particles can also be divided in the guiding center position  $\mathbf{X}_g$  and the Larmor radius position vector  $\boldsymbol{\rho}_L$  as

$$\mathbf{x} = \mathbf{X}_g + \boldsymbol{\rho}_L = \mathbf{X}_g + \frac{\hat{\mathbf{b}} \times \mathbf{v}_{\perp}}{\Omega_{C_s}} \quad (\text{B.4})$$

with  $\Omega_{C_s} = \frac{q_s B}{m_s c}$  the cyclotronic frequency for a particle of species  $s$ . We can notice that since  $\bar{\mathbf{v}}_{\perp} = 0$ , then  $\bar{\boldsymbol{\rho}}_L = 0$  and thus  $\bar{\mathbf{x}} = \mathbf{X}_g$ . This means that gyroaveraged distribution function depends only on the position of the guiding centers such that  $\bar{f}_s(\mathbf{X}_g, v_{\perp}, \varphi, v_{\parallel}, t)$ . Neoclassical transport (which is studied by the drift kinetic equation) is caused mostly by the movement of the guiding centers so the distribution function is also expanded in order to the smallness of the Larmor radius such that the expansion parameter is

$$\delta = \frac{\rho_{\theta l}}{L_{\perp}} \ll 1, \quad (\text{B.5})$$

so that

$$f = f_0 + f_1 + \dots \quad (\text{B.6})$$

The temporal derivatives are considered to be second order in  $\delta$ . At zeroth order the electric field is electrostatic so that  $\mathbf{E} = -\nabla\Phi_0 + \mathbf{E}^*$  with the electromagnetic part  $\mathbf{E}^* \sim \delta\mathbf{E}$ . The constants of motion of the particles trajectories are not the velocities but the magnetic moment and energy defined (when divided by the mass  $m_s$  of the particle) as

$$\mu = \frac{v_{\perp}^2}{2B} \quad (\text{B.7})$$

and

$$\epsilon = \frac{v_{\parallel}^2}{2} + \frac{v_{\perp}^2}{2} + \frac{q_s}{m_s} \Phi_0(\mathbf{x}). \quad (\text{B.8})$$

The Boltzmann equation can in these coordinates be written as

$$\frac{\partial f_s}{\partial t} + \mathbf{v}_s \cdot \nabla_{\mathbf{x}_s} f_s + \frac{d\mu}{dt} \frac{f_s}{\partial\mu} + \frac{d\epsilon}{dt} \frac{f_s}{\partial\epsilon} + \frac{d\varphi}{dt} \frac{f_s}{\partial\varphi} = C(f_s), \quad (\text{B.9})$$

where the derivatives of  $f_s$  are done holding  $\mu$ ,  $\epsilon$  and  $\varphi$  fixed. By noting that we can choose the unit vectors  $\hat{\mathbf{e}}_1$  and  $\hat{\mathbf{e}}_2$  to be in the radial direction of  $\mathbf{v}_{\perp}$  (in the velocity space) and in the

diamagnetic direction defined by  $\hat{b} \times \mathbf{v}$  we can write

$$\nabla_{\mathbf{v}_s} f = \frac{\partial f}{\partial v_{\parallel}} \hat{b} + \frac{\partial f}{\partial v_{\perp}} \frac{\mathbf{v}_{\perp}}{v_{\perp}} + \frac{\partial f}{\partial v_{\varphi}} \frac{\hat{b} \times \mathbf{v}_{\perp}}{v_{\perp}}. \quad (\text{B.10})$$

Using this result we may write

$$\frac{d\mu}{dt} = -\frac{\mu}{B} \mathbf{v} \cdot \nabla B - \frac{v_{\parallel}}{B} \mathbf{v} \mathbf{v} : (\nabla \hat{b}) + \frac{q_s}{m_s} \mathbf{v} \cdot \mathbf{E}, \quad (\text{B.11})$$

$$\frac{d\epsilon}{dt} = \frac{q_s}{m_s} \mathbf{v} \cdot \mathbf{E}^*, \quad (\text{B.12})$$

$$\frac{d\varphi}{dt} = \Omega_C + \mathcal{O}(\rho_L \Omega_C). \quad (\text{B.13})$$

Where  $:$  indicates a tensor product and  $\mathbf{v} \mathbf{v}$  is a tensor. Dividing the distribution function into  $\bar{f}$  and  $\tilde{f}$  we obtain

$$\frac{\partial \bar{f}}{\partial t} + \mathbf{v} \cdot \nabla_{\mathbf{x}} \bar{f} + \frac{d\mu}{dt} \frac{\partial \bar{f}}{\partial \mu} + \frac{d\epsilon}{dt} \frac{\partial \bar{f}}{\partial \epsilon} + \frac{d\varphi}{dt} \frac{\partial \bar{f}}{\partial \varphi} + \frac{d\tilde{f}}{dt} = C(\bar{f} + \tilde{f}). \quad (\text{B.14})$$

We then can apply a gyroaverage to get

$$\frac{\partial \bar{f}}{\partial t} + \mathbf{v}_{\parallel} \cdot \nabla_{\mathbf{x}} \bar{f} + \frac{q}{m} E_{\parallel}^* v_{\parallel} \frac{\partial \bar{f}}{\partial \epsilon} + \frac{d\varphi}{dt} \frac{\partial \bar{f}}{\partial \varphi} + \overline{\frac{d\tilde{f}}{dt}} = \overline{C(\bar{f} + \tilde{f})}, \quad (\text{B.15})$$

where we have used

$$\overline{\frac{d\mu}{dt}} = 0, \quad (\text{B.16})$$

since  $\overline{v_{\perp}} = 0$ ,  $\mathbf{B} \cdot \nabla B = 0$ , and

$$\overline{\mathbf{v} \mathbf{v}} = v_{\parallel}^2 \hat{b} \hat{b} + \frac{v_{\perp}^2}{2} (\mathcal{I} - \hat{b} \hat{b}), \quad (\text{B.17})$$

with  $\hat{b} \hat{b} : \nabla \hat{b} = 0$ , and where we have used

$$\overline{\frac{d\epsilon}{dt}} = \frac{q}{m} E_{\parallel}^* v_{\parallel}. \quad (\text{B.18})$$

Subtracting equation B.15 from B.9 we obtain

$$\mathbf{v}_{\perp} \cdot \nabla_{\mathbf{x}} \tilde{f} + \frac{q}{m} \mathbf{E}_{\perp}^* \cdot \mathbf{v}_{\perp} \frac{\partial \tilde{f}}{\partial \epsilon} + \frac{d\mu}{dt} \frac{\partial \tilde{f}}{\partial \mu} + \frac{d\tilde{f}}{dt} - \overline{\frac{d\tilde{f}}{dt}} = C(\tilde{f} + \bar{f}) - \overline{C(\tilde{f} + \bar{f})}, \quad (\text{B.19})$$

The leading term in equation B.9 implies

## Appendix B. Derivation of the drift kinetic equation

---

$$-\Omega_C \frac{\partial f_0}{\partial \varphi} = 0 \quad (\text{B.20})$$

which states that  $\tilde{f}_0 = 0$  and thus  $f_0 = \tilde{f}_0$  and  $\tilde{f} \sim \delta \tilde{f}$ . The leading terms in B.15 are of order  $\mathcal{O}(\rho_L \Omega_C f)$  which gives the equation

$$\mathbf{v}_\parallel \cdot \nabla_{\mathbf{x}} f_0 = \overline{C(f_0)}, \quad (\text{B.21})$$

Since we may always linearize the collision operator we may write  $\overline{C(f_0)} = C(\overline{f_0}) = C(f_0)$ . The solvability equation for the magnetic differential equation B.15, can be shown to hold only if  $C(f_0) = 0$ , which happens only if  $f_0$  is a Maxwellian (H-theorem) such that

$$f_0 = f_M(\mathbf{x}, \varepsilon) = n_s(\mathbf{x}) \left( \frac{m_s}{2\pi} \right)^{\frac{3}{2}} T_s(\mathbf{x})^{-\frac{3}{2}} e^{-\frac{m_s \varepsilon}{T_s(\mathbf{x})}}, \quad (\text{B.22})$$

and

$$\mathbf{v}_\parallel \cdot \nabla_{\mathbf{x}} f_0 = 0. \quad (\text{B.23})$$

The  $\mathcal{O}(\rho_L \Omega_C f)$  order terms in B.19 hold the equation

$$\mathbf{v}_\perp \cdot \nabla_{\mathbf{x}} f_0 - \Omega_C \frac{\partial \tilde{f}_1}{\partial \varphi} = 0 \quad (\text{B.24})$$

which can be integrated to obtain

$$\tilde{f}_1 = -\boldsymbol{\rho}_L \cdot \nabla_{\mathbf{x}} f_0 \quad (\text{B.25})$$

since

$$\mathbf{v}_\perp = \frac{\partial}{\partial \varphi} (\mathbf{v} \times \hat{\mathbf{b}}) = \frac{\partial}{\partial \varphi} \left( -\frac{\boldsymbol{\rho}_L}{\Omega_C} \right). \quad (\text{B.26})$$

The drift kinetic equation is the equation which is given by the terms of order  $\mathcal{O}(\rho_L^2 \Omega_C f)$  in the gyroaveraged boltzmann equation B.15 and is written as

$$\frac{\partial \tilde{f}}{\partial t} + \mathbf{v}_\parallel \cdot \nabla_{\mathbf{x}} \tilde{f}_1 + \frac{q}{m} E_\parallel^* v_\parallel \frac{\partial f_0}{\partial \varepsilon} + \overline{\frac{d \tilde{f}_1}{dt}} = C(\tilde{f}_1). \quad (\text{B.27})$$

The term  $\overline{\frac{d\tilde{f}_1}{dt}}$  can be simplified by using B.25 which implies

$$\overline{\frac{d\tilde{f}_1}{dt}} = -\overline{\frac{d}{dt}(\boldsymbol{\rho}_L \cdot \nabla_x f_0)} = -\overline{\frac{d\boldsymbol{\rho}_L}{dt} \cdot \nabla_x f_0} - \overline{\boldsymbol{\rho}_L \cdot \frac{d}{dt}(\nabla_x f_0)} \quad (\text{B.28})$$

The second term B.28 is proportional to

$$\frac{d}{dt}(\nabla_x f_0) = \left( \mathbf{v} \cdot \nabla_x + \frac{d\epsilon}{dt} \frac{\partial}{\partial \epsilon} \right) \nabla_x f_0 = \mathbf{v} \cdot \nabla_x \nabla_x f_0 + \frac{q_s^*}{m_s} v_{\parallel} \frac{\partial}{\partial \epsilon} (\nabla_x f_0) \approx \mathbf{v} \cdot \nabla_x \nabla_x f_0 \quad (\text{B.29})$$

as the terms multiplied by  $E^*$  are of higher order than the others in B.28 and can be neglected. The second term of B.28 can thus be written as

$$-\overline{\boldsymbol{\rho}_L \cdot \frac{d}{dt}(\nabla_x f_0)} = -\overline{\boldsymbol{\rho}_L \mathbf{v} \cdot \nabla_x \nabla_x f_0}. \quad (\text{B.30})$$

Since

$$\overline{\boldsymbol{\rho}_L \mathbf{v}} = \frac{v_{\perp}^2}{2\Omega_C} (\hat{e}_2 \hat{e}_1 - \hat{e}_1 \hat{e}_2) \quad (\text{B.31})$$

is antisymmetric and  $\nabla_x \nabla_x f_0$  is symmetric then

$$-\overline{\boldsymbol{\rho}_L \cdot \frac{d}{dt}(\nabla_x f_0)} = 0. \quad (\text{B.32})$$

The first term in B.28 is proportional to the gyroaverage of

$$\frac{d}{dt} \boldsymbol{\rho}_L = \mathbf{v} \cdot \nabla_x \left( \frac{\hat{\mathbf{b}} \times \mathbf{v}}{\Omega_C} \right) + \frac{q_s}{m_s} (\mathbf{E} + \mathbf{v}_s \times \mathbf{B}) \cdot \nabla_v \left( \frac{\hat{\mathbf{b}} \times \mathbf{v}}{\Omega_C} \right) = \mathbf{v} \cdot \nabla_x \left( \frac{\hat{\mathbf{b}}}{\Omega_C} \right) \times \mathbf{v} - \frac{c}{B^2} \mathbf{E} \times \mathbf{B}, \quad (\text{B.33})$$

which is written as

$$\overline{\frac{d}{dt} \boldsymbol{\rho}_L} = \left( v_{\parallel}^2 - v_{\perp}^2 \right) \hat{\mathbf{b}} \cdot \nabla_x \left( \frac{\hat{\mathbf{b}}}{\Omega_C} \right) \times \hat{\mathbf{b}} + \frac{v_{\perp}^2}{2} \sum_i^3 \hat{e}_i \cdot \nabla_x \left( \frac{\hat{\mathbf{b}}}{\Omega_C} \right) \times \hat{e}_i - \frac{c}{B^2} \mathbf{E} \times \mathbf{B} = \quad (\text{B.34})$$

$$= \left( v_{\parallel}^2 - v_{\perp}^2 \right) \frac{1}{\Omega_C} \boldsymbol{\kappa} \times \hat{\mathbf{b}} - \frac{v_{\perp}^2}{2\Omega_C} \nabla \times \hat{\mathbf{b}} - \frac{v_{\perp}^2}{2\Omega_C B} \hat{\mathbf{b}} \times \nabla B - \frac{c}{B^2} \mathbf{E} \times \mathbf{B}. \quad (\text{B.35})$$

and thus

$$\overline{\frac{d}{dt} \boldsymbol{\rho}_L} = -\mathbf{v}_d \quad (\text{B.36})$$

is the drift velocity of the particle following the magnetic field. The drift velocity is thus an gyro averaged measure of the deviation of the guiding center of a particle from its original trajectory along the magnetic field line and it is due to the gyro movement of the particle around the magnetic field. The drift kinetic equation can then be written as

## Appendix B. Derivation of the drift kinetic equation

---

$$v_{\parallel} \hat{b} \cdot \nabla_{x_s} \bar{f}_1 + \boldsymbol{v}_d \cdot \nabla_{x_s} f_0 - \frac{q_s E_{\parallel} v_{\parallel}}{T_s} f_0 = C(\bar{f}_1). \quad (\text{B.37})$$

It is an equation for the first order gyroaveraged distribution function. It is this part of the distribution function that can be used to obtain the parallel part of the background ion flows in section 2.8.



# Bibliography

- [1] Eurofusion. Eurofusion. <https://www.euro-fusion.org>, 2021. Accessed: 2021-09-02.
- [2] U. S. Energy Information Administration. *Annual Energy Outlook 2021*. Independent Statistics Analysis, 2021.
- [3] Jeffrey P. Friedberg. *Ideal MHD*. Cambridge University Press, 1st edition, 11th August, 2021.
- [4] Per Helander. Theory of plasma confinement in non-axisymmetric magnetic fields. *Rep. Prog. Phys.*, 77(8):087001, 2014.
- [5] F. Wagner et al. 'Regime of improved confinement and high beta in neutral-beam-heated divertor discharges of the asdex tokamak. *Phys. Rev. Lett.*, 49(1408), 1982.
- [6] F. J. Casson et al. 'Theoretical description of heavy impurity transport and its application to the modelling of tungsten in jet and asdex upgrade. *Plasma Phys. Control. Fusion*, 57(014031), 2015.
- [7] T. Pütterich et al. 'Theoretical description of heavy impurity transport and its application to the modelling of tungsten in jet and asdex upgrade. *Plasma Phys. Control. Fusion*, 55(3124036), 2013.
- [8] ITER. Divertor. <https://www.iter.org/mach/Divertor>, 2021. Accessed: 2021-09-02.
- [9] P. Helander and D. J. Sigmar. Collisional Transport in Magnetized Plasmas. *Cambridge University Press, Cambridge*, 2022.
- [10] R. D. Hazeltine. Recursive derivation of drift-kinetic equation. *Plasma Physics*, 15(77), 1973.
- [11] F. L. Hinton and R. D. Hazeltine. Theory of plasma transport in toroidal confinement systems. *Rev. Mod. Phys.*, 48(239), 1976.
- [12] R. D. Hazeltine and A. A. Ware. The drift kinetic equation for toroidal plasmas with large mass velocities. *Plasma Physics*, 20(673), 1978.
- [13] F. L. Hinton and S. K. Wong. Neoclassical ion transport in rotating axisymmetric plasmas. *The Physics of Fluids*, 26(3082), 1985.

## Bibliography

---

- [14] S. Newton. Neoclassical momentum transport in an impure rotating tokamak plasma. *Physics of Plasmas*, 13(012505), 2006.
- [15] M. N. Rosenbluth and R. D. Hazeltine. Plasma transport in toroidal confinement systems. *Physics of Plasmas*, 15(116), 1972.
- [16] R. D. Hazeltine and F. L. Hinton. Plasma transport in a torus of arbitrary aspect ratio. *The Physics of Fluids*, 16(1645), 1973.
- [17] P. H. Rutherford. Collisional diffusion in an axisymmetric torus. *The Physics of Fluids*, 13(482), 1970.
- [18] M. Taguchi. Ion thermal conductivity and ion distribution function in the banana regime. *Plasma Phys. Control. Fusion*, 30(1987), 1988.
- [19] M. Wakatani. *Stellarator and Heliotron Devices*. Oxford University Press, Oxford, 1998.
- [20] K. C. Shaing et al. Neoclassical plasma viscosity and transport processes in non-axisymmetric tori. *Nuclear Fusion*, 55(125001), 2015.
- [21] K. C. Shaing. Viscosity-driven impurity transport in a stellarator. *The Physics of Fluids*, 26(3164), 1983.
- [22] K. C. Shaing and J. D. Callen. Neoclassical flows and transport in nonaxisymmetric toroidal plasmas. *The Physics of Fluids*, 26(3315), 1983.
- [23] K. C. Shaing and J. D. Callen. Calculation of parallel viscosity in the plateau regime. *The Physics of Fluids*, 26(1526), 1983.
- [24] K. C. Shaing et al. Neoclassical transport fluxes in the plateau regime in nonaxisymmetric toroidal plasmas. *The Physics of Fluids*, 29(521), 1986.
- [25] K. C. Shaing et al. Bootstrap current control in stellarators. *Physics of Fluids B: Plasma Physics*, 1(166), 1989.
- [26] K. C. Shaing et al. Bootstrap current and parallel viscosity in the low collisionality regime in toroidal plasmas. *Physics of Fluids B: Plasma Physics*, 1(146), 1989.
- [27] K. C. Shaing. Poloidal and parallel plasma viscosities in tokamak geometry. *Physics of Fluids B: Plasma Physics*, 2(2847), 1989.
- [28] Y. Ogawa et al. Analysis of neoclassical transport in the banana regime with the dkes code for the large helical device. *Nuclear Fusion*, 32(1), 1992.
- [29] K. C. Shaing. Driftorbidriven flux and plasma viscosity in asymmetric toroidal plasmas. *Physics of Plasmas*, 3(4276), 1996.
- [30] K. C. Shaing. Transport processes close to magnetic axis in quasihelically symmetric stellarators. *Physics of Plasmas*, 4(3341), 1997.

- 
- [31] K. C. Shaing. Squeezed superbananas and improved superbanana transport in stellarators. *Physics of Plasmas*, 9(2865), 2002.
  - [32] N. Nakajima, , and M. Okamoto. Neoclassical flow, current, and rotation in general toroidal systems. *J. Phys. Soc. Jpn.*, 61:833–843, 1992.
  - [33] P. Helander et al. *Stellarator bootstrap current and plasma flow velocity at low collisionality*. *J. Plasma Physics*, 83(905830206), 2017.
  - [34] K. C. Shaing. *Magnetohydrodynamic-activity-induced toroidal momentum dissipation in collisionless regimes in tokamaks*. *Physics of Plasmas*, 10(1443), 2003.
  - [35] K. C. Shaing. *Transport processes in the vicinity of a magnetic island in tokamaks*. *Physics of Plasmas*, 9(849), 2002.
  - [36] K. C. Shaing. *Transport processes in the vicinity of a magnetic island in tokamaks*. *Physics of Plasmas*, 9(849), 2002.
  - [37] K. C. Shaing. *Radial electric field and plasma confinement in the vicinity of a magnetic island*. *Physics of Plasmas*, 9(3470), 2002.
  - [38] K. C. Shaing. *Plasma flow and confinement in the vicinity of a rotating island in tokamaks*. *Physics of Plasmas*, 10(4728), 2003.
  - [39] K. C. Shaing. *Plasma flow and confinement in the vicinity of a rotating island in tokamaks*. *Physics of Plasmas*, 10(4728), 2003.
  - [40] K. C. Shaing et al. *Plasma and momentum transport processes in the vicinity of a magnetic island in a tokamak*. *Nuclear Fusion*, 43(4), 2003.
  - [41] K. C. Shaing. *Magnetic island induced bootstrap current on island dynamics in tokamaks*. *Physics of Plasmas*, 13(022501), 2006.
  - [42] K. C. Shaing. *Island-induced bootstrap current on the saturation of a thin magnetic island in tokamaks*. *Physics of Plasmas*, 14(042507), 2007.
  - [43] P. H. Rutherford. *Impurity transport in the pfirschschl*
  - [44] S.P. Hirshman and D.J. Sigmar. *Neoclassical transport of impurities in tokamak plasmas*. *Nuclear Fusion*, 21(9), 1981.
  - [45] J. A. Wesson. *Poloidal distribution of impurities in a rotating tokamak plasma*. *Nuclear Fusion*, 37(5), 1997.
  - [46] M. Romanelli and M. Ottaviani. *Effects of density asymmetries on heavy impurity transport in a rotating tokamak plasma*. *Plasma Phys. Control. Fusion*, 40(1767), 1998.
  - [47] T. Füllöp and P. Helander. *Nonlinear neoclassical transport in a rotating impure plasma with large gradients*. *Physics of Plasmas*, 6(30662), 1999.

## Bibliography

---

- [48] C. Angioni and P. Helander. *Neoclassical transport of heavy impurities with poloidally asymmetric density distribution in tokamaks*. Plasma Phys. Control. Fusion, 56(12), 2014.
- [49] P. Helander. *Bifurcated neoclassical particle transport*. Physics of Plasmas, 5(3999), 1998.
- [50] P. Helander. *Impurity transport in a mixed-collisionality stellarator plasma*. Phys. Rev. Letters, 118(155002), 2017.
- [51] I. Calvo et al. *Stellarator impurity flux driven by electric fields tangent to magnetic surfaces*. Nucl. Fusion, 5(124005), 2018.
- [52] S. Buller et al. *Collisional transport of impurities with flux-surface varying density in stellarators*. J. Plasma Physics, 84(905840409), 2018.
- [53] M. Sertoli et al. *Modification of impurity transport in the presence of saturated  $(m, n) = (1, 1)$  mhd activity at asdex upgrade*. Nucl. Fusion, 55(113029), 2015.
- [54] T. C. Hender et al. *The role of mhd in causing impurity peaking in jet hybrid plasmas*. Nucl. Fusion, 56(066002), 2016.
- [55] M. Raghunathan et al. *Heavy impurity confinement in hybrid operation scenario plasmas with a rotating 1/1 continuous mode*. Plasma Physics and Controlled Fusion, 59(124002), 2017.
- [56] Madhusudan Raghunathan. *Effects of 3D Ideal MHD Equilibrium Geometry on Neoclassical Properties in Tokamaks: Exploring Bootstrap Current and Impurity Accumulation*. PhD thesis, École Polytechnique et Fédéral de Lausanne, Lausanne, Switzerland, 2018.
- [57] S. P. Hirshman. *Steepestdescent moment method for threedimensional magnetohydrodynamic equilibria*. Phys. Fluids, 26(3553), 1983.
- [58] S. P. Hirshman et al. *Three-dimensional free boundary calculations using a spectral green's function method*. Computer Physics Communications, 143(355343), 1986.
- [59] W.A. Cooper et al. *Free boundary equilibrium in 3d tokamaks with toroidal rotation*. Nucl. Fusion, 55(063032), 2015.
- [60] D. Pfefferlé et al. *Venus-levis and its spline-fourier interpolation of 3d toroidal magnetic field representation for guiding-centre and full-orbit simulations of charged energetic particles*. Computer Physics Communications, 185(12), 2014.
- [61] David Pfefferlé. *Energetic ion dynamics and confinement in 3D saturated MHD configurations*. PhD thesis, École Polytechnique et Fédéral de Lausanne, Lausanne, Switzerland, May 2015.
- [62] P. Donnel et al. *Moment approach of the multi-species non-linear coulomb collision operator adapted to particle-in-cell codes*. Plasma Phys. Control. Fusion, 63(025006), 2021.

- [63] N. Nakajima et al. 'On relation between hamada and boozer magnetic coordinate systems. J-Stage, 68(4):395–403, 1992.
- [64] A. H. Boozer. *Plasma equilibrium with rational magnetic surfaces*. The Physics of Fluids, 24(1999), 1981.
- [65] A. H. Boozer. *Establishment of magnetic coordinates for a given magnetic field*. The Physics of Fluids, 25(520), 1982.
- [66] S. Hamada. *Hydromagnetic equilibria and their proper coordinates*. Nuclear Fusion, 2(23), 1962.
- [67] J. Wesson. Tokamaks. Oxford University Press, Oxford, 2011.
- [68] S. L. Newton et al. 'Collisional bulk ion transport and poloidal rotation driven by neutral beam injection. Physics of Plasmas, 14(062301), 2007.
- [69] A. J. Brizard. *Nonlinear gyrokinetic vlasov equation for toroidally rotating axisymmetric tokamaks*. Phys. Plasmas, 2(459), 1995.
- [70] M. D. Kruskal and R. M. Kuslud. *Stability of ideal and resistive internal kink modes in toroidal geometry*. The Physics of Fluids, 30(1756), 1987.
- [71] R. J. Hastie et al. *Stability of ideal and resistive internal kink modes in toroidal geometry*. The Physics of Fluids, 1(265), 1958.
- [72] V. S. Marchenko. *Impurity holes in tokamaks with electron cyclotron resonance heating of the helical core*. Physics of Plasmas, 27(022516), 2020.



# EDUARDO NETO

Email: [eduardo.lascasneto@gmail.com](mailto:eduardo.lascasneto@gmail.com)

Address: EPFL SB SPC, Station 13, CH-1015 Lausanne

Phone: (+351)916182968



---

## SUMMARY

PhD student, with a particular interest in the development of models for plasma physics and controlled fusion, based on analytical work and numerical simulations carried out on high performance computers.

---

## EDUCATION

**Swiss Plasma Center (SPC) - EPFL**, Lausanne, Switzerland

*PhD in Plasma Physics*

**July 2017 – December 2021**

**Thesis Title:** Heavy impurity transport in the presence of 3D MHD ideal perturbations, Supervisor: Prof. Jonathan P. Graves

**Instituto Superior Técnico - University of Lisbon**, Lisbon, Portugal

*MSc on Technological Engineering Physics - Grade: 17/20*

**September 2014 – May 2016**

**Main topics:** Nuclear Fusion, Kinetic Theory, Computational Physics, General Relativity, Quantum Mechanics

**Thesis Title:** Turbulence and Sheared Flow in Fusion Plasmas, Supervisor: Prof. Nuno F. Loureiro

**Instituto Superior Técnico - University of Lisbon**, Lisbon, Portugal

*BsC on Technological Engineering Physics - Grade: 17/20*

**September 2011 – May 2014**

---

## TEACHING EXPERIENCE

**Teaching Assistantship**

- Computational physics II, 2nd semester Physics, EPFL 2018-2019, 2019-2020.
- Computational physics I, 1st semester Physics, EPFL 2018-2019, 2019-2020, 2020-2021.
- Physics lab IIb, 2nd semester Physics, EPFL 2017-2018.
- Physics lab IIIa, 1st semester Physics, EPFL 2017-2018.

---

## AWARDS

**Diploma of Academic Merit**

*Instituto Superior Técnico, University of Lisbon*

**March 2017**

Awarded for finishing the Technological Engineering Physics MSc within the top 15% of graduates.

---

## PEER-REVIEWED PUBLICATIONS 2021

**Heavy impurity transport in tokamaks subject to plasma rotation, NTV and the influence of saturated ideal MHD perturbations**, E. Lascas Neto, J. P. Graves, M. Raghunathan, C. Sommariva, D. Pfefferlé, and JET contributors, Plasma Physics and Controlled Fusion, Volume 64, Number 1, 2021 [doi: [10.1088/1361-6587/ac3964](https://doi.org/10.1088/1361-6587/ac3964)]

**CONFERENCE  
CONTRIBUTIONS  
(AS FIRST  
AUTHOR)**

**2021**

**Heavy impurity transport in the presence of 3D MHD ideal saturated modes, rotation and ambipolar electric field**, E. Neto, J. P. Graves, M. Raghunathan, G. Bustos Ramirez, D. Pfefferlé, W. A. Cooper and C. Sommariva, presentation (invited) at the 10th SFP Workshop, Wuhan, China, 2021

**2019**

**Heavy Impurity transport in tokamaks with plasma flows and saturated, 3D Perturbations**, E. Neto, J. P. Graves, M. Raghunathan, S. Lanthaler, D. Pfefferlé, W.A.Cooper, C. Sommariva and JET contributors, (poster) Proceedings of the 46th EPS conference in Plasma Physics, Milan, Italy, 2019

**2018**

**Self-consistent numerical calculation of neoclassical effects of 3D MHD geometry on heavy impurity transport in the presence of strong rotation**, E. Neto, J. Graves, M. Raghunathan, S. Lanthaler, D. Pfefferlé and JET contributors, (poster) Theory Of Fusion Plasmas Joint Varenna - Lausanne International Workshop, Varenna, Italy 2018

---

**SKILLS**

**Programming:** C, C++, Fortran, Nvidia CUDA, MPI, ROOT  
**Tools:** MATLAB, Mathematica  
**Scripting:** Bash and utils (grep)  
**Mechanical design:** Autodesk Autocad  
**Others:** L<sup>A</sup>T<sub>E</sub>X, Microsoft Word, Excel and Powerpoint

---

**LANGUAGES**

**Portuguese:** Mother tongue  
**English:** Fluent  
**French:** Elementary  
**German:** Elementary

---

**OTHER  
INTERESTS**

Guitar, piano, singing, tennis